Centro de Investigación Científica y de Educación

Superior de Ensenada, Baja California

Doctorado en Ciencias

en Óptica con orientación en Óptica Física

Femtosecond laser-induced periodic surface structures formation on thin films

Tesis

para cubrir parcialmente los requisitos necesarios para obtener el grado de

Doctor en Ciencias

Presenta:

José Ricardo Santillán Díaz

Ensenada, Baja California, México

2021

Tesis defendida por

José Ricardo Santillán Díaz

y aprobada por el siguiente Comité

Dra. Paulina Segovia Olvera
Codirectora de tesis

Dr. Santiago Camacho López
Codirector de tesis

Dr. Anatoly Zayats

Dr. Eugenio Rafael Méndez Méndez

Dr. Raul Rangel Rojo

Dr. Gregory Wurtz

Dra. Karina Garay-Palmett
Coordinadora del Posgrado en Óptica

Dr. Pedro Negrete Regagnon
Director de Estudios de Posgrado

Resumen de la tesis que presenta José Ricardo Santillán Díaz como requisito parcial para la obtención del grado de Doctor en Ciencias en Óptica con orientación en Óptica Física.

Estructuras periódicas superficiales inducidas por láser de femtosegundos en películas delgadas

Resumen aprobado por:

Dra. Paulina Segovia Olvera	Dr. Santiago Camacho López
Codirectora de tesis	Codirector de tesis

En años recientes, el interés en el estudio de la formación de estructuras periódicas inducidas con láser (LIPSS por sus siglas en inglés) ha ido en aumento. Sin embargo, debido a la complejidad de los diversos procesos involucrados, no ha sido posible establecer una teoría que pueda explicar exitosamente la extensa variedad de estructuras obtenidas experimentalmente. En este trabajo se presenta un estudio teórico y experimental de la formación de LIPSS sobre películas delgadas de bismuto y titanio, la fuente de luz que se empleó para hacer las irradiaciones es un láser pulsado de femtosegundos Yb de fibra (Satsuma HP2, Amplitude Systems) que produce pulsos de 270 fs a una longitud de onda central de 1030 nm y con frecuencia de repetición de 1 kHz y 5 kHz. Para determinar los parámetros de irradiación adecuados, se hizo una caracterización del umbral de ablación de cada película. Se propuso un conocido modelo fenomenológico para determinar los parámetros de irradiación adecuados para la formación de dichas estructuras. Mediante la transformada de Fourier de micrografías ópticas y de SEM se determinó la periodicidad, orientación y distribución angular de las LIPSS. Los resultados indican que los modelos electromagneticos, basados en la interacción de luz linealmente polarizada con una superficie que exhibe una rugosidad microscópica, son efectivos para predecir la aparicion de LIPSS en ambos materiales y su evolución al variar el ángulo de incidencia, sin embargo no son totalmente eficaces para predecir la variacion de la periodicidad con el número de pulsos aplicados. Adicionalmente, se demostro la oxidación inducida por láser de ambos materiales y la formación de LIPSS en dichos óxidos, estas LIPSS poseen características que las distinguen de aquellas que son metálicas. Finalmente, se desarrolló un modelo numérico basado en el método de diferencias finitas en el dominio temporal (FDTD) como un esfuerzo para predecir la formación y evolución de los patrones que los modelos teóricos no pudieron explicar completamente. Dicho modelo se construyó tomando en cuenta las propiedades dieléctricas del sustrato irradiado así como las características del láser con el que se llevó a cabo las irradiaciones. Los resultados se muestran al final de esta tesis.

Palabras clave: Laser pulsado, femtosegundos, nanoestructuras, LIPSS, oxidos, titanio, bismuto, transformada de fourier, plasmones, FDTD.

Abstract of the thesis presented by José Ricardo Santillán Díaz as a partial requirement to obtain the degree in Physical Optics.

Femtosecond laser-induced periodic surface structures formation on thin films

Abstract approved by:

Dra. Paulina Segovia Olvera
Thesis Co-Director

Dr. Santiago Camacho López
Thesis Co-Director

In the present work, we develop a theoretical and experimental study on the formation of Laser Induced Periodic Surface Structures (LIPSS) on the surface of bismuth and titanium thin films. The light source that we used to produce such structures is an Ytterbium fiber laser (Satsuma HP2, Amplitude Systems) producing 270 femto-second pulses at a central wavelength of 1030 nm, frequency repetition rates of 1 kHz and 5 kHz. To determine the required irradiation parameter for producing this LIPSS, we carried out a characterization on the ablation threshold fluence on each film. Furthermore, we proposed to modify a well-known phenomenological model which treats the pulse laser ablation as a cumulative process. Once we have produced the patterns, we use a simple image processing technique based on the Fourier transform of optical and SEM micrographs of the structures. This technique gives us the periodicity, orientation ans dispersion of the LIPSS orientation angle among other significant values. The analysis of the experimental results, shows that the current electromagnetic-based models are adequate to predict the occurrence of LIPSS on both materials as well as their evolution when varying the angle on incidence. Nevertheless, such models are not effective to explain the change on the LIPSS periodicity as the number of pulses is increased. Additionally, we demonstrated the laser-induced oxidation of both materials and the formation of LIPSS on those oxides. Finally, we developed a numerical model based on the Finite Difference Time-Domain method as an attempt to predict the formation and evolution of the patterns that the theoretical models can not. To build the numerical model it is necessary to take into account the actual dielectric properties of the substrate as the characteristics of the pulsed laser. The results are shown at the end of this thesis

Keywords: Pulsed Laser, femto-seconds, nano-structures, LIPSS, oxides, titanium, bismuth, Fourier transform, Plasmons, Surface plasmon-polaritons, FDTD.

Dedicatory

I dedicate this thesis to Gregory Wurtz, Santiago Camacho, Paulina Segovia and my friends Corinne Luna, and Abraham Wong. Thank you for your guidance, support and friendship throughout all these years.

Acknowledgment

To Dr. Raul Rangel, Dr. Eugenio Mendez, Dr. Anatholy Zayatz, and Dr. Gregory Wurtz, thank you for agreeing to be members of my thesis committee, you were more than generous with your knowledge, expertise, and precious time. I thank the Optics Department of the Applied Physics Division at CICESE and the Department of Physics at the University of North Florida, for allowing me to conduct my research as well as providing me any assistance requested. I also thank the "Consejo Nacional de Ciencia y Tecnología" (CONACyT) for providing me the economic support to carry out this thesis. Scholarship holder: 394035.

Tambien quiero agradecer a Alejandro Adame y Elvia Arana quienes fueron como unos padres para mi desde que llegué a Ensenada. A mi amigo Carlos Guerrero por su incondicional amistad todos estos años. A mi amiga Miriam Carrillo y a todos los amigos que hice durante este camino, en especial a Lamborghini Sotelo, Corinne Luna, Abraham Wong, Nayeli Casillas, David Reyes y Cecilia Guerra por incontables buenos momentos y risas, a Marielos, Carlos Ochoa, a Victor Rico, a Yulia Kotolevich, a Gibraham Alejandro una de las personas mas formidables que he conocido, a Alma Gonzalez, a Yahaira, Cindy, Jacob, Lucho, Gabriel Castillo, Rene Rodriguez, Marcos Plata y Hector Sanchez. Finalmente, agradezco a mi madre y a quienes fueron mis profesores asi como el personal administrativo del departamento de Óptica. En especial a Carmen Ochoa, Marla Monjaraz, Fabian Alonso, Isaac Fimbres, Laura Rebeca Pineda, Citlali Romero, Elizabeth Aviles y a todos mis profesores sobre todo a los doctores Victor Ruiz, Eugenio Mendez, Hector Escamilla, Roger Cudney, Israel Rocha, Pedro Negrete y Rufina Hernandez.

Table of contents

Page

Table of contents (continued)

List of figures

List of tables

Chapter 1. Introduction

1.1 Background and research motivation

Ablation is the driving mechanism of several practical laser applications, like high-precision cutting, generation of nanoparticles, and particularly, surface functionalization of materials by micro- and nano-structuring; this latter consists of modifying the material actual surface morphology with laser-induced surface textures. Surface nano-structuring may bestow new properties on materials (Chen *et al.*, 2013). For instance, color, wettability (hydrophobicity or hydrophilicity), tribologic properties, and wear-resistance. On metals, surface structuring may modify their optical properties, excite surface plasmons, enhance X-ray emission and stimulate surface-enhanced Raman scattering (SERS) (Ossi, 2018). The laser-induced periodic surface structures (LIPSS) are a particular type of nano-structure that can be generated by a single linearly polarized laser beam. The most common LIPSS, consist of a relief composed of quasi-periodic lines or ripples like those of figure 1. The period and orientation of LIPSS are correlated with the wavelength and polarization of the radiation.

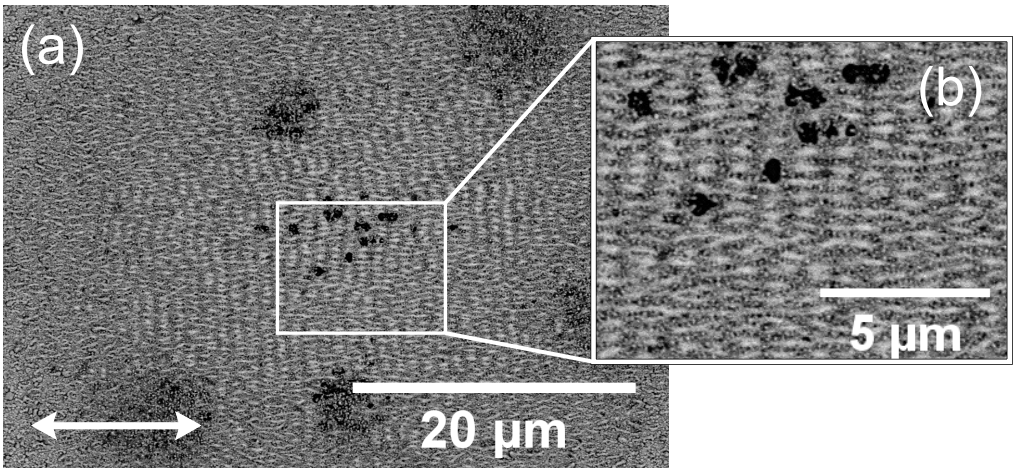

Figure 1. SEM micrographs of LSFL (a) and HSFL (b) present on the surface of a thin bismuth film irradiated with a fs-pulse laser.

In 1965, these structures where discovered by Milton Birnbaum upon irradiating polished germanium with a focused ruby laser beam (Birnbaum, 1965). Ever since, LIPSS have been produced on several metals, semiconductors, dielectrics, and polymers (Bonse *et al.*, 2017) in a wide range of pulse duration, from continuous-wave irradiation down to only a few femtoseconds. One of the most striking features of LIPSS is that they can be generated in a single-step process while exposed to

the environment. The formation and characteristics of LIPSS depend on the irradiation parameters and the material's optical response.

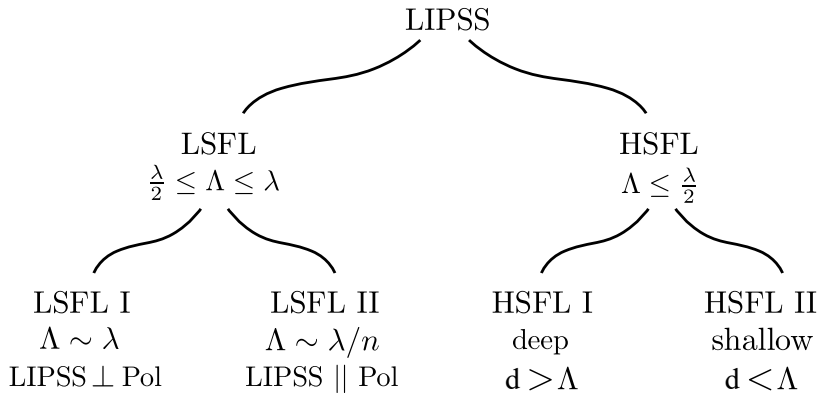

Figure 2. LIPSS classification scheme according to the ripples period respecting to the laser wavelength (Bonse, 2012).

As shown in figure 2, we can classify LIPSS into two groups by the aspect ratio between their periodicity Λ and the incident light wavelength λ. The low spatial frequency LIPSS (LSFL) with periods in the interval $\frac{\lambda}{2} \leq \Lambda \leq \lambda$ and the high spatial frequency LIPSS (HSFL) whose periods are significantly smaller than the irradiation wavelength ($\Lambda \leq \frac{\lambda}{2}$). Their orientation also depends on the type of material; in strong absorbing materials like metals or semiconductors, LSFL orientation is perpendicular to the laser beam polarization. While in dielectrics, LSFL may be either parallel o perpendicular (Bonse *et al.*, 2012). The HSFL, on the other hand, may exhibit both orientations. They are generated predominantly in transparent materials for pulse durations in the range from picosecond down to femtosecond at a fluence very close to the damage threshold.

1.2 Aims and objectives

The driving mechanism of LIPSS formation has been on debate since Birnbaum observed them for the first time. Initially, Birnbaum attributed their origin to a diffraction effect and suggested that the material removal occurring at the electric field maximums intensity may produce surface relief (Birnbaum, 1965). In 1973, Emmony *et al.* suggested that LIPSS might be generated via interference of the incident laser beam with light scattered at surface defects and scratches (Emmony *et al.*, 1973). In 1982, Emmony *et al.*, Keilmann and Bai explored this idea in more detail and proposed that LSFL might arise from the interference between the incident light and surface plasmon polaritons (SPP) excited by the rough surface defects (Keilmann and Bai, 1982). Nowadays, it is

generally accepted that LSFL are generated from the interaction between incident and scattered electromagnetic waves (Bonse *et al.*, 2017). Unlike LSFL, several mechanisms have been proposed to explain the formation of HSFL, such as second harmonic generation (Borowiec and K. Haugen, 2003), the involvement of specific types of plasmon modes (Martsinovskiĭ *et al.*, 2008), or self-organization (Reif *et al.*, 2002; Sakabe *et al.*, 2014; Tsibidis and Stratakis, 2017). Figure 3 shows some of the most studied.

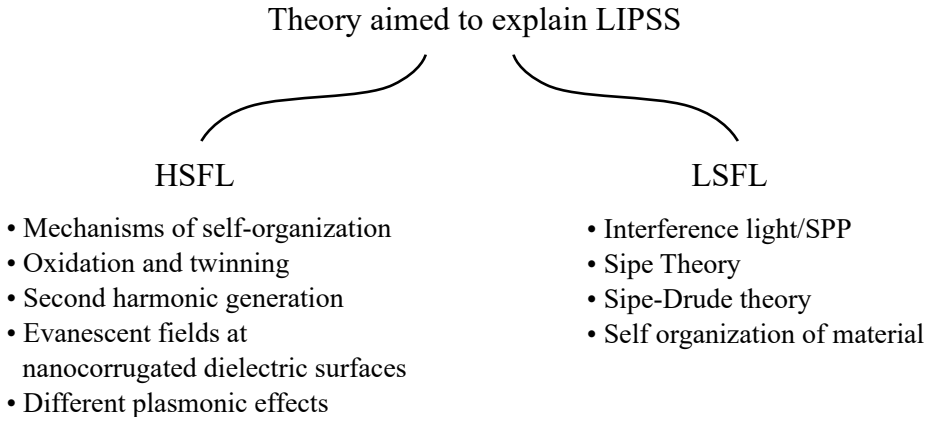

Figure 3. Some of the main models to explain the formation of HSFL and LSFL.

This work aims to study the formation of LIPSS on thin films of bismuth and titanium using a femtosecond pulsed laser far below the ablation threshold fluence. Along with studying the dependence of parameters such as number of pulses, angle of incidence and fluence. In addition, we assess and compare the currently existing models for LIPSS formation that are based on the electromagnetic theory. To overcome the limitations of those models, we develop a numerical approach via the finite-difference time-domain technique to simulate LIPSS formation due to ablation on dispersive materials. Also, LIPSS on bismuth thin films have a great potential to be applied in fields like surface coloring, color coding, polarization sensitive displays, surface texturing, diffraction gratings for miniaturized spectroscopy devices, plasmonics for an spectral range from far IR to UV (Toudert *et al.*, 2017). In this context, the experimental and theoretical study of LIPSS formation on bismuth, with femtosecond laser pulses, is proposed for the first time in this thesis.

On the other hand, titanium is a very relevant metal that has been vastly used in industry due to its high corrosion and temperature resistance, light weight and biocompatibility. Even though, the formation of LIPSS on Ti has been widely studied (Gnilitskyi *et al.*, 2017; Xian-Feng Li, 2014; Dostovalov, 2017), in this thesis we analyze the process of LIPSS formation with fluence values far below to the ablation threshold.

1.3 Thesis outline

In chapter 2, we illustrate the fundamental physical processes occurring during laser-material interaction. We start by analyzing the electron-phonon dynamics upon ultra-fast laser irradiation, then we introduce the concept and main features of laser-induced periodic surface structures (LIPSS). Finally, we use the Maxwell equations in media to develop tools that will allow us to develop models to explain the formation of LIPSS in later sections.

In chapter 3 we make a review of the most accepted theoretical models of LIPSS formation based on the electromagnetic theory. We obtain the requirements to excite surface plasmon polaritons (SPPs) and introduce the concept of the SPP dispersion relation. Then, we present a LIPSS formation model based on interference between incident light and SPPs. Afterwards, we show the efficacy factor theory as an analytic solution of Maxwell equations that allow us to describe the formation of LIPSS.

In chapter 6 we present our experimental methods and results. We start by proposing to use a phenomenological model to treat the ablation threshold as the result of a cumulative process upon multiple pulses. Such model relates the laser fluence with the number of pulses necessary to produce LIPSS, then we analyze the effect of varying those parameters on the LIPSS periodicity and the dispersion of the LIPSS orientation angle (DLOA).

In chapter 5 we analyze the formation of laser-induced oxides and the effect of them on the LIPSS periodicity.

In chapter 6 we develop a numerical model which is based on modified version of the finite-difference time-domain method to incorporate the Drude-Lorentz and the holographic method in order to be able to simulated the formation of ablative LIPSS on metals.

Finally, in chapter 7 we summarize the conclusions obtained throughout the previous chapters of this thesis.

Chapter 2. Theoretical background

In the following chapter, we illustrate the fundamental physical processes occurring during laser-material interaction. We start by analyzing the electron-phonon dynamics upon ultra-fast laser irradiation, then we introduce the concept and main features of laser-induced periodic surface structures (LIPSS). Finally, we use the Maxwell equations in media to develop tools that will allow us to develop models to explain the formation of LIPSS in later sections.

2.1 Ultrafast laser–material interaction

Among the variety of laser-material interactions that may occur in solids, we can mention (Shugaev *et al.*, 2016; Schaaf, 2010): absorption, heating, melting, evaporation, recoil pressure, piston effect, plasma formation, and laser-supported absorption waves, Marangoni convection, and Kelvin-Helmholtz instabilities. Ultrafast (10^{-9} s $-$ 10^{-15} s) pulse-laser irradiation relies on the deposition of light energy into the target via excitation of electrons on a timescale shorter than the lattice heat diffusion time (Schaaf, 2010). For laser wavelengths between the infrared and ultraviolet regions, electrons thermalize first their kinetic energy with the other electrons in the conduction band via collisions. Then, they transfer the thermal energy to the lattice by electron-phonon collisions long after the pulse falling edge (Sakabe *et al.*, 2014; Shugaev *et al.*, 2016). For this reason, the electronic dynamic determines the ultrafast laser processing of materials.

Electronic transitions by light absorption determine the optical properties of the medium; figure 4 depicts the difference between the band structures of metals, semiconductors, and insulators. In metals, photons are directly absorbed by the electrons within the conduction band via intraband transitions. On the other hand, in semiconductors and dielectrics, bounded electrons below the Fermi level need to be promoted across the band-gap energy to the conduction bands via interband transition.

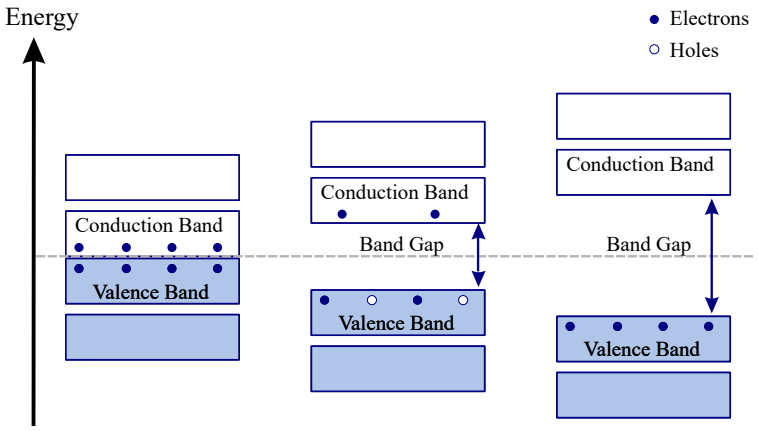

Figure 4. If the free-carrier concentration in a semiconductor is quite high (typically $> 10^{18}$ cm^{-3}), excess free electrons (holes) fill the conduction (valence) band and the semiconductor shows metallic character. In wide bandgap dielectrics, the main mechanisms involved in the generation of free electrons by photons having lower energy than the bandgap are multiphoton and avalanche ionizations, which are highly nonlinear processes.

The laser beam induces an extreme non-equilibrium electronic-distribution state. Excited electrons in the conduction band can produce effective, nonlinear, and multiphoton laser energy absorption(Schaaf, 2010; Shugaev *et al.*, 2016), which may bring the material to a dense electron-hole plasma causing non-thermal phase transformations like Coulomb explosion. Then, the electron gas temperature may reach several thousands of Kelvins inside a room-temperature lattice (Phillips *et al.*, 2015; Schaaf, 2010). Subsequent transfer energy from electrons to lattice vibrations, via electron-electron and electron-phonon interactions, can lead to rapid heating of the medium with rates exceeding 10^{14} K/s (Shugaev *et al.*, 2016), resulting in homogeneous melting or even formation of a supercritical fluid. We can write the electronic-temperature transfer rate between excited electrons and lattice as:

$$\frac{\partial T_e}{\partial t} = \frac{T_L - T_e}{\tau_{ep}}, \tag{1}$$

where T_e and T_L are the electronic and lattice temperatures, and τ_{ep} represents the electron–phonon coupling-time given by (Schaaf, 2010):

$$\tau_{ep} = \frac{2\pi k_B T_e}{3\hbar\lambda_p \omega_D^2}, \tag{2}$$

where λ_p is the characteristic coupling constant, and ω_D the medium Debye frequency. Typical values for metals imply that the electron-phonon coupling-time occurs on the order of hundreds

of femtoseconds, which is approximately two orders of magnitude slower than the electron-electron scattering time (Phillips *et al.*, 2015; Schaaf, 2010). Therefore, since the lattice cannot respond on a time scale as short as the electrons, the electrons and lattice temperature can be described by the following set of coupled heat transport equations, known as the two-temperature model (Anisimov, 1974):

$$C_e \frac{\partial T_e}{\partial t} = \nabla[k_e \nabla T_e] - H(T_L, T_e) + S(t) \tag{3}$$

$$C_L \frac{\partial T_L}{\partial t} = H(T_L, T_e), \tag{4}$$

here, C_e and C_L represent the electronic and lattice specific heat capacities, respectively. $S(t)$ represents the absorbed laser power per unit of volume, $H(T_e, T_L)$ is the rate of energy transfer between electrons and lattice, and $\nabla[k_e \nabla T_e]$ is the diffusive electronic heat transfer. Upon the pulse-laser irradiation, three regimes may take place; non-thermal phase transformation, thermal phase melting, and ablation; this latter consists of laser-induced removal of material from the irradiated target. When the femtosecond laser light fluence exceeds some specific threshold, part of the surface melts, then the superheating of the liquid phase and high nucleation rates of the gas phase eject material from the surface in the form of an ablation plume.

2.2 Optical response of solids

When irradiating an atom with laser light, the atomic nucleus and electron cloud may experience a mutual displacement proportional to the electric field intensity, the atomic nucleus in the electric field direction while the electron cloud in the opposite one. Thus, the shifted atom constitutes an induced electric dipole. On a macroscopic scale, this phenomenon is known as electronic polarization. Nevertheless, other sources of polarization may arise (fujiwara2009, xiaofang2019, dorey2011), like:

- Atomic or ionic; here, the electric field distorts the electrically charged ions that compose an ionic crystal.
- Dipolar; consists of an alignment to the electric field direction of dipoles that can be either inherent (permanent dipoles) or induced by asymmetric distortion of the nuclei.

- Space charge; based on the movement of charge carriers trapped by interfaces in heterogeneous systems.

The electric permittivity or complex dielectric constant (ε) determines the magnitude of the induced polarization. However, for the sake of simplicity, henceforth we will use the relative permittivity ε_r, which is the dimensionless ratio of the electric permittivity to the permittivity in free-space (ε_0). Moreover, the dependence of the dielectric permittivity on the applied electric-field frequency is known as dielectric dispersion. Figure 5 illustrates a typical dielectric dispersion shape of dielectrics, indicating the different polarization sources on top of the corresponding regions.

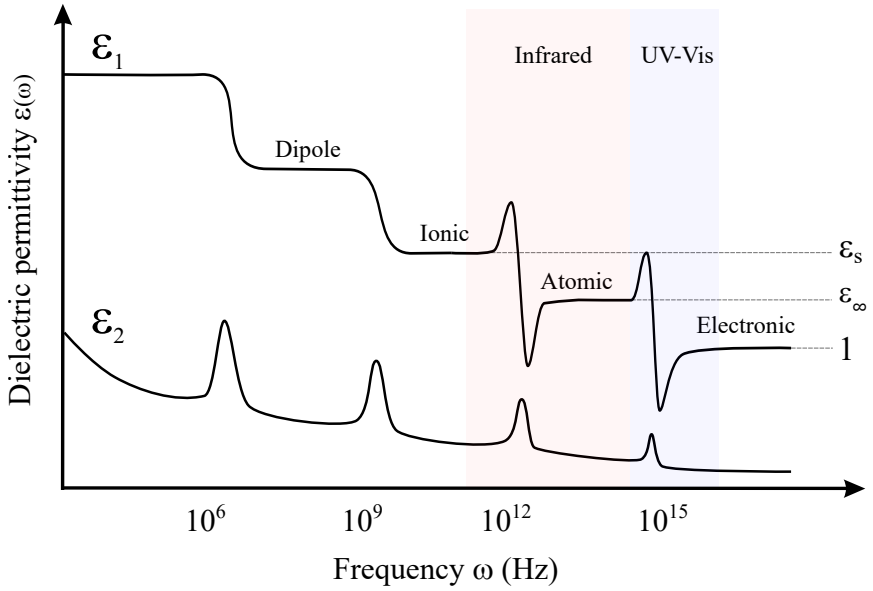

Figure 5. Dielectric dispersion; the different types of polarization are indicated in the regions they correspond. The resonant oscillation for atomic polarization is generally observed in the infrared region, while the resonant oscillation for electric polarization occurs in the UV/visible region.

Since nuclei are too heavy to follow the electric field frequency, electrons determine the electronic polarization. As illustrated in figure 5, the resonant oscillation for atomic polarization generally appears in the infrared region. At higher frequencies, in the UV-Vis region, the atomic polarization oscillations cannot follow the incoming electric field frequency; consequently, only the electronic polarization remains. As the angular frequency goes to infinity, the electric polarization cannot follow the oscillation of light, and the dielectric constant takes the same value as within the vacuum ($\varepsilon_r = 1$). In this case, any material becomes transparent to the electric field.

2.2.1 Maxwell equations in media

Maxwell's equations determine the macroscopic electromagnetic fields in media through the following set of differential equations:

$$\nabla \times \mathbf{H} = \frac{\partial \mathbf{D}}{\partial t} + \mathbf{J} \tag{5a}$$

$$\nabla \times \mathbf{E} = -\frac{\partial \mathbf{B}}{\partial t} - \mathbf{M} \tag{5b}$$

$$\nabla \cdot \mathbf{D} = \rho \tag{5c}$$

$$\nabla \cdot \mathbf{B} = 0. \tag{5d}$$

The vector $\mathbf{E}$ represents the electric field vector in units of volts per meter [V/m], $\mathbf{D}$ the electric displacement vector, $\mathbf{H}$ the magnetic field strength vector, $\mathbf{B}$ the magnetic flux density vector, $\mathbf{J}$ the electric current density vector, $\mathbf{M}$ the magnetic current density vector, and ρ the electric charge density. Furthermore, the electromagnetic fields are linked through the following constitutive relations:

$$\mathbf{D} = \varepsilon_0 \mathbf{E} + \mathbf{P}, \tag{6a}$$

$$\mathbf{B} = \mu_0 (\mathbf{H} + \mathbf{M}). \tag{6b}$$

The macroscopic polarization $\mathbf{P}$ is defined as the dipole moment per unit volume, and the magnetization $\mathbf{M}$ is defined as the magnetic moment per unit volume. The relation between $\mathbf{P}$ and $\mathbf{E}$ for non-magnetic materials ($\mathbf{M} = 0$), assuming local response in space, can be expressed as

$$\mathbf{P}(\mathbf{r}, t) = \varepsilon_0 \int \chi(t - t') \mathbf{E}(\mathbf{r}, t') dt'. \tag{7}$$

The electric susceptibility χ, determines the degree of polarization that the medium exhibits in response to an external electric field. By applying a Fourier transform and the convolution theorem on equation 103, we obtain the following expression for the polarization in the frequency domain,

$$\widetilde{\mathbf{P}}(\mathbf{k},\omega) = \varepsilon_0 \tilde{\chi}(\omega)\widetilde{\mathbf{E}}(\mathbf{k},\omega). \tag{8}$$

If we further assume the material to be non-dispersive, $\tilde{\chi}$ becomes a constant so that equation 102 reduces to

$$\widetilde{\mathbf{P}}(\mathbf{k},\omega) = \varepsilon_0 \tilde{\chi}\widetilde{\mathbf{E}}(\mathbf{k},\omega). \tag{9}$$

Introducing the complex relative permittivity, $\tilde{\varepsilon}_r = 1 + \tilde{\chi}$, we can write the constitutive relation of equation 6a in the frequency domain as

$$\widetilde{\mathbf{D}} = \varepsilon_0 \tilde{\varepsilon}_r \widetilde{\mathbf{E}}(\mathbf{k},\omega). \tag{10}$$

Assuming the absence of external charges or currents, we can use equation 10 to express Faraday's law (eq.5a) in the frequency domain as

$$i\mathbf{k} \times \widetilde{\mathbf{H}} = -i\omega\varepsilon_0 \tilde{\varepsilon}_r \widetilde{\mathbf{E}}. \tag{11}$$

Therefore, the time depended Maxwell's curl equations of non-magnetic, linear, isotropic, non-dispersive materials are

$$\nabla \times \mathbf{H} = \varepsilon_0 \varepsilon_r \frac{\partial \mathbf{E}}{\partial t} \tag{12a}$$

$$\nabla \times \mathbf{E} = -\mu \frac{\partial \mathbf{H}}{\partial t}. \tag{12b}$$

2.2.2 The Lorentz oscillator model for dielectrics

When it comes to electronic polarization, we can treat electrons as tiny harmonic oscillators bound to positively charged nuclei with a resonance frequency ω_o. This classical description of electrons dynamics in response to electromagnetic waves is known as the Lorentz oscillator model. Within

the framework of this model, the electron equation of motion is

$$m_e \frac{d^2\mathbf{r}}{dt^2} = -m_e\Gamma\frac{d\mathbf{r}}{dt} - m_e\omega_o^2\mathbf{r} - e\mathbf{E}_o\exp(i\omega t), \tag{13}$$

after performing a Fourier transform,[1] equation 13 becomes:

$$-m_e\omega^2\mathbf{r}(\omega) = im_e\omega\gamma\mathbf{r}(\omega) - m_e\omega_o^2\mathbf{r}(\omega) - e\mathbf{E}(\omega), \tag{14}$$

and solving for $\mathbf{r}(\omega)$, we obtain

$$\mathbf{r}(\omega) = -\frac{e}{m_e}\frac{1}{\omega_o^2 - i\Gamma\omega - \omega^2}\mathbf{E}(\omega). \tag{15}$$

The displacement of the electron from the equilibrium position produces a time-varying dipole moment $\mathbf{p}(\omega)$. Accordingly, if N represents the number of electrons per unit volume, the macroscopic polarization (dipole moment per unit volume) is given by

$$\mathbf{P}(\omega) = -N_e\mathbf{p}(\omega), \tag{16a}$$

$$= -N_e e\mathbf{r}(\omega), \tag{16b}$$

$$= \left(\frac{N_e e^2}{m_{\text{eff}}}\right)\frac{1}{\omega_o^2 - i\Gamma\omega - \omega^2}\mathbf{E}(\omega). \tag{16c}$$

We can separate the total polarization into two terms, the first one corresponds to the non-resonant background, $\mathbf{P}$, and the second one to the oscillator resonant-response, $\mathbf{P}_{\text{Lorentz}}$ so that the constitutive relation of equation 6a becomes

$$\mathbf{D} = \varepsilon_0\mathbf{E} + \mathbf{P} + \mathbf{P}_{\text{Lorentz}}. \tag{17}$$

When the dielectric is not excited, no electrons contribute to the Lorentz polarization ($N_e = 0$),

[1] According to our sign convention, the Fourier transform of the divergence and curl operators are $\frac{\partial}{\partial t} \to -i\omega$ and $\nabla\times \to ik\times$ respectively

then $\mathbf{P}_{\text{Lorentz}} = 0$. By combining equations 9 and 17 we obtain

$$\mathbf{D} = \varepsilon_0 \mathbf{E}(\omega) + \varepsilon_0 \chi \mathbf{E}(\omega) + \frac{N_e e^2}{m_{\text{eff}}} \frac{1}{\omega_o^2 - i\Gamma\omega - \omega^2} \mathbf{E}(\omega), \tag{18a}$$

$$= \varepsilon_0 \left(1 + \chi + \frac{N_e e^2}{\varepsilon_0 m_{\text{eff}}} \frac{1}{\omega_o^2 - i\Gamma\omega - \omega^2} \right) \mathbf{E}(\omega), \tag{18b}$$

this latter equation represents the constitutive relation associated with a linear, isotropic, dispersive medium. We identify the expression inside the parentheses as the relative permittivity:

$$\varepsilon_r = 1 + \chi + \frac{N_e e^2}{\varepsilon_0 m_{\text{eff}}} \frac{1}{\omega_o^2 - i\Gamma\omega - \omega^2}. \tag{19}$$

Let us now introduce the static dielectric constant ε_s, representing the dielectric constant value at frequencies well below the resonance,

$$\varepsilon_s = \lim_{\omega \ll \omega_o} \varepsilon_r = 1 + \chi + \frac{N_e e^2}{\varepsilon_0 m_{\text{eff}} \omega_o^2}. \tag{20}$$

Thus, we can replace the Lorentz equation with this constant, which includes the contributions of both atomic and electronic polarization, as shown in figure 5. On the other hand, at frequencies above the infrared region, the atomic polarization disappears since the atomic oscillations no longer follow the incoming electric field frequency. Then, the value of the high-frequency dielectric constant, ε_∞, is

$$\varepsilon_\infty = \lim_{\omega \to \infty} \varepsilon_r = 1 + \chi. \tag{21}$$

Therefore, by combining equations 20 and 21, we can write the contribution of the Lorentz oscillator to the relative permittivity as

$$\varepsilon_{\text{Lorentz}} = \frac{(\varepsilon_s - \varepsilon_\infty)\omega_o^2}{\omega_o^2 - i\Gamma\omega - \omega^2}. \tag{22}$$

2.2.3 The free-electron model for metals

In the presence of an external electric field, metals exhibit low polarization. Since their inner-shell electrons weakly interact with the external electric field, the interaction occurs mostly with the valence or free electrons, which may produce electric currents and re-radiate the light energy causing the characteristic metallic high-reflectivity. At a macroscopic scale, the Drude model provides a classical description of the optical response of metals. According to this model, the metal is represented as a gas of free electrons in the conduction band with density N_e, moving against a fixed background of positive ions (Maier, 2007). The free electrons oscillate due to the Lorentz force that the external electromagnetic field generates. Additionally, electrons experience collisions that damp their movement with a characteristic frequency $\Gamma = 1/\langle\tau\rangle$ ($\sim$ 100 THz). Where $\langle\tau\rangle$ is known as the mean scattering time of the free electron, typically on the order of 10^{-14} s at room temperature. Therefore, the motion equation of an electron within such plasma is:

$$m_{\text{eff}}\frac{d^2\mathbf{r}}{dt^2} = -m_{\text{eff}}\Gamma\frac{d\mathbf{r}}{dt} - e\mathbf{E}, \tag{23}$$

once again, $\mathbf{r}$ represents the displacement of the electron from their equilibrium position. The exact mechanisms related to the electron-electron and the electron-ion interactions are not directly considered, so those interactions are taken into account by modifying the mass of the electrons m_e with a multiplying factor, leading to an effective mass $m_{\text{eff}} = m_e m_{opt}$. After applying a Fourier transform, the equation 23 becomes,

$$-m_{\text{eff}}\omega^2\mathbf{r}(\omega) = im_{\text{eff}}\omega\Gamma\mathbf{r}(\omega) - e\mathbf{E}(\omega), \tag{24}$$

and solving for $\mathbf{r}(\omega)$, we obtain

$$\mathbf{r}(\omega) = \frac{e}{m_{\text{eff}}(\omega^2 + i\Gamma\omega)}\mathbf{E}(\omega). \tag{25}$$

Similarly to the Lorentz model, the polarization of the material $\mathbf{P} = \varepsilon_0\chi_e\mathbf{E}(\omega)$ is related to the electron displacement by $\mathbf{P} = -eN_e\mathbf{r}(\omega)$, leading to express the electric susceptibility as

$$\chi = \frac{\omega_p^2}{\omega^2 + i\Gamma\omega}, \tag{26}$$

here we have introduced the well-known plasma frequency, ω_p, given by $\omega_p^2 = N_e e^2/\varepsilon_0 m_{\text{eff}}$. Hence the dielectric function, $\varepsilon_r = 1 - \chi$, is given by

$$\varepsilon_r(\omega) = \varepsilon_\infty - \frac{\omega_p^2}{\omega^2 + i\Gamma\omega}. \tag{27}$$

As with the Lorentz model, we have added the constant ε_∞ for the permittivity at high-frequency. For electric-field frequencies below the plasma frequency, the real part of the dielectric function becomes negative, and the material exhibits its metallic properties.

2.2.4 Drude-Lorentz model

At visible frequencies, the free-electron model description of metals may not be accurate enough due to the presence of inter-band transitions (Maier, 2007). To overcome this limitation, we implement a combined model known as the Drude-Lorentz model, which allows us to consider any number of resonances through a simple summation of classical damped harmonic oscillators representing each discrete vibrational mode, of the form

$$\varepsilon(\omega) = \varepsilon_\infty - \frac{\omega_p^2}{\omega^2 + i\Gamma_0\omega} + \sum_{j=1}^{P} \frac{A_j(\varepsilon_s - \varepsilon_\infty)\omega_j^2}{\omega_j^2 - i\Gamma_j\omega - \omega^2}. \tag{28}$$

The first term in equation 28 represents the electron's response in the conduction-band followed by a summation of P Lorentzian terms representing the electron excitation through inter-band transitions. Each of them possesses its particular resonance frequency (ω_j), oscillator strength (A_j), and damping constant (Γ_j).

2.2.5 Spectroscopic ellipsometry

When irradiating a sample with linearly polarized light, the linear polarization often becomes elliptical upon light reflection, as shown in figure 6. Ellipsometry is an optical measurement technique

that allows us to characterize the dielectric permittivity of substrates by light reflection (or transmission). This technique is based on measuring the ratio ρ of the amplitude reflection coefficients r_p and r_s for parallel and perpendicular polarization, respectively (Fujiwara, 2007); this is

$$\rho \equiv r_p/r_s \equiv \tan(\Psi)\exp(-i\Delta), \tag{29}$$

where Ψ and Δ represent the amplitude ratio and phase difference, respectively. In Spectroscopic Ellipsometry (SE), (Ψ, Δ) spectra are measured by changing the wavelength of light.

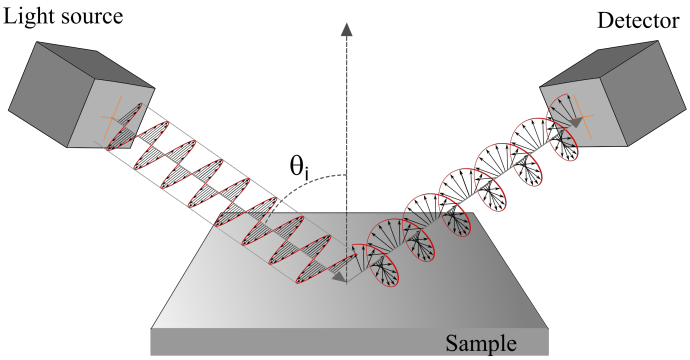

Figure 6. Scheme of spectroscopic ellipsometry characterization of thin films.

When the SE data are acquired on a flat bulk substrate with no oxide on its surface. It is possible to directly determine the optical constants from the ellipsometry data. Equation 29 can be rewritten in terms of Fresnel equations as

$$\rho = r_p/r_s = \frac{\left(\frac{\varepsilon_t}{\varepsilon_i}\right)^2\cos(\theta_i) - \sqrt{\left(\frac{\varepsilon_t}{\varepsilon_i}\right)^2 - \sin^2(\theta_i)}}{\left(\frac{\varepsilon_t}{\varepsilon_i}\right)^2\cos(\theta_i) + \sqrt{\left(\frac{\varepsilon_t}{\varepsilon_i}\right)^2 - \sin^2(\theta_i)}} = \frac{\frac{\sqrt{\varepsilon_i}\varepsilon_t\cos(\theta_i) - \varepsilon_i\sqrt{\varepsilon_t - \varepsilon_i\sin^2(\theta_i)}}{\sqrt{\varepsilon_i}\varepsilon_t\cos(\theta_i) + \varepsilon_i\sqrt{\varepsilon_t - \varepsilon_i\sin^2(\theta_i)}}}{\frac{\sqrt{\varepsilon_i}\cos(\theta_i) - \sqrt{\varepsilon_t - \varepsilon_i\sin^2(\theta_i)}}{\sqrt{\varepsilon_i}\cos(\theta_i) + \sqrt{\varepsilon_t - \varepsilon_i\sin^2(\theta_i)}}}, \tag{30}$$

introducing variables $n_{ii} = \sqrt{\varepsilon_i}\cos(\theta_i)$ and $n_{tt} = \sqrt{\varepsilon_t - \varepsilon_i\sin^2(\theta_i)}$, we get

$$\rho = \frac{\frac{\varepsilon_t n_{ii} - \varepsilon_i n_{tt}}{\varepsilon_t n_{ii} + \varepsilon_i n_{tt}}}{\frac{n_{ii} - n_{tt}}{n_{ii} + n_{tt}}} = \frac{\varepsilon_i \sin^2(\theta_i) - n_{tt} n_{ii}}{\varepsilon_i \sin^2(\theta_i) + n_{tt} n_{ii}} = \frac{\sin^2(\theta_i) - \cos(\theta_i)\sqrt{\frac{\varepsilon_t}{\varepsilon_i} - \sin^2(\theta_i)}}{\sin^2(\theta_i) + \cos(\theta_i)\sqrt{\frac{\varepsilon_t}{\varepsilon_i} - \sin^2(\theta_i)}}, \tag{31}$$

assuming $\varepsilon_i = 1$ and $\varepsilon_t = \langle\varepsilon\rangle$ into equation 31 and solving for $\langle\varepsilon\rangle$ we obtain:

$$\langle\varepsilon\rangle = \sin^2(\theta_i)\left[1 + \tan^2(\theta_i)\left(\frac{1-\rho}{1+\rho}\right)^2\right], \tag{32}$$

which is known as the pseudo-dielectric function.

2.3 Laser induced oxidation

Oxidation of films by classical thermal treatments exhibits several striking differences in comparison to the laser-induced oxidation (Nanai *et al.*, 1997); this latter can be described by the Wagner theory for thick films (thickness $\geq$ 100 nm) or the Cabrera-Mott theory for thin films (thickness $<$ 100 nm). While the Wagner theory assumes there are no electric currents across the film, the Cabrera-Mott theory considers that the oxidation of a metallic substrate is based on the freely diffusion of electrically charged species (Nanai *et al.*, 1997), like the oxide and metal ions, electrons, and holes to the reaction site through the oxide layer. This diffusion is determined by gradients in the chemical potential and the electric fields (Xia *et al.*, 2019). The metal has an oxide surface thickness of few angstroms that is generated due to the exposition of the film to air; upon irradiation, the electrons jump from the metal through the oxide and ionize the adsorbed oxygen molecules by tunneling and thermionic emission effects; as a result, a uniform electric field is created in the oxide layer which drives the oxygen ions migration and causes the oxide layers thickness increasing until the Fermi levels in the metal and absorbed layers are equal and the Mott potential disappears. The oxidation rate decreases sharply because of the rapidly declining electric field as the oxide layer grows (Xia *et al.*, 2019).

Chapter 3. Electromagnetic models on the formation of LIPSS

3.1 Plasmonic model

When a laser beam strikes onto a rough metallic surface, there is a chance that part of the incident light may excite electromagnetic modes at the metal-dielectric interface, known as surface plasmon polaritons (SPPs). As mentioned previously, it is generally accepted that the LSFL driving mechanism is the interaction between incident and scattered electromagnetic waves on the rough surface, particularly SPPs. The incident light and the SPPs may interfere with each other to produce an interference pattern perpendicular to the incident light polarization, whose period would be slightly shorter than the laser wavelength. For this reason, several authors consider the SPPs to play a significant role in the formation of type-I LSFL. In the following sections, we will develop a LIPSS formation model based on the plasmonic theory.

3.1.1 Fundamental properties of SPP

Surface plasmon polaritons (SPPs) are electromagnetic excitations that are strongly confined to a metal-dielectric interface along which they propagate. These excitations result from coupling surface plasmons (collective oscillation of the electron plasma on the conductors) with electromagnetic waves. To deduce the main properties of SPPs, we start by applying Maxwell's equations on a configuration like the one shown in figure 7, which consists of an infinite flat interface between two different mediums of different dielectric constants, ε_1 ($z < 0$) and ε_2 ($z > 0$).

Figure 7. Planar dielectric interface.

Let us assume harmonic time-dependence on the electric and magnetic fields,

$$\begin{aligned} \mathbf{E}(\mathbf{r},t) &= \mathbf{E}(r)\exp(-i\omega t), \\ \mathbf{H}(\mathbf{r},t) &= \mathbf{H}(r)\exp(-i\omega t). \end{aligned} \tag{33}$$

We can find explicit expressions for the electric and magnetic spatial components by substituting 33 into the Maxwell curl equations (12a and 12b) in the absence of external charges or current densities:

$$\begin{aligned} \frac{\partial E_z}{\partial y} - \frac{\partial E_y}{\partial z} &= i\omega\mu_0 H_x, & \frac{\partial E_x}{\partial z} - \frac{\partial E_z}{\partial x} &= i\omega\mu_0 H_y, \\ \frac{\partial E_y}{\partial x} - \frac{\partial E_x}{\partial y} &= i\omega\mu_0 H_z, & \frac{\partial H_z}{\partial y} - \frac{\partial H_y}{\partial z} &= -i\omega\varepsilon_0\varepsilon E_x, \\ \frac{\partial H_x}{\partial z} - \frac{\partial H_z}{\partial x} &= -i\omega\varepsilon_0\varepsilon E_y, & \frac{\partial H_y}{\partial x} - \frac{\partial H_x}{\partial y} &= i\omega\varepsilon_0\varepsilon E_z. \end{aligned} \tag{34}$$

Without loss of generality, we set a coordinate system where the wave propagates along the x-direction ($\frac{\partial}{\partial x} = i\beta$) with no variation in the y-direction ($\frac{\partial}{\partial y} = 0$) so that the dielectric permittivity depends only on the z coordinate, $\varepsilon = \varepsilon(z)$. Hence, we can express the electric and magnetic spatial components as

$$\begin{aligned} \mathbf{E}(\mathbf{r}) &= \mathbf{E}(z)\exp(i\beta x), \\ \mathbf{H}(\mathbf{r}) &= \mathbf{H}(z)\exp(i\beta x), \end{aligned} \tag{35}$$

where $\beta = k_x$ is known as the propagation constant. The equations system 34 becomes:

$$\begin{aligned} \frac{\partial E_y}{\partial z} &= -i\omega\mu_0 H_x, & \frac{\partial E_x}{\partial z} - i\beta E_z &= i\omega\mu_0 H_y, \\ \beta E_y &= \omega\mu_0 H_z, & \frac{\partial H_y}{\partial z} &= i\omega\varepsilon_0\varepsilon E_x, \\ \frac{\partial H_x}{\partial z} - i\beta H_z &= -i\omega\varepsilon_0\varepsilon E_y, & \beta H_y &= \omega\varepsilon_0\varepsilon E_z. \end{aligned} \tag{36}$$

Equation system 36 allows two sets of self-consistent solutions. The first one is called transverse magnetic (TM or p) mode due to the magnetic field points perpendicular to the incident plane; the only nonzero field components are E_x, E_z, and H_y. By contrast, the other solution is called

transverse electric mode (TE or s) since the electric field points perpendicular to the incident plane; the nonzero field components, in this case, are H_x, H_z, and E_y. Considering the TM-mode, system 36 reduces to:

$$\begin{aligned} i\omega\mu_0 H_y &= \frac{\partial E_x}{\partial z} - i\beta E_z, \\ i\omega\varepsilon_0\varepsilon E_x &= \frac{\partial H_y}{\partial z}, \\ \omega\varepsilon_0\varepsilon E_z &= \beta H_y. \end{aligned} \tag{37}$$

The solution of 37 corresponds to a propagating wave in the x-direction with evanescent decay in the perpendicular z-direction (Raether, 2014; Maier, 2007). Above the interface ($z > 0$), the field components are:

$$H_y(z) = A_2 e^{i\beta x} e^{-k_2 z}, \tag{38a}$$

$$E_x(z) = iA_2 \frac{1}{\omega\varepsilon_0\varepsilon_2} k_2 e^{i\beta x} e^{-k_2 z}, \tag{38b}$$

$$E_z(z) = -A_2 \frac{\beta}{\omega\varepsilon_0\varepsilon_2} e^{i\beta x} e^{-k_2 z}; \tag{38c}$$

while below the interface ($z < 0$):

$$H_y(z) = A_1 e^{i\beta x} e^{k_1 z}, \tag{39a}$$

$$E_x(z) = -iA_1 \frac{1}{\omega\varepsilon_0\varepsilon_1} k_2 e^{i\beta x} e^{k_1 z}, \tag{39b}$$

$$E_z(z) = -A_1 \frac{\beta}{\omega\varepsilon_0\varepsilon_1} e^{i\beta x} e^{k_1 z}. \tag{39c}$$

Continuity of H_y, and $\varepsilon_i E_z$ at the interface ($z = 0$) requires that $A_1 = A_2$. Additionally, continuity of E_z leads to the condition

$$\frac{k_1}{\varepsilon_1} + \frac{k_2}{\varepsilon_2} = 0, \tag{40}$$

to fulfill this condition, the product $\Re\{\varepsilon_1\}$ and $\Re\{\varepsilon_2\}$ must have opposite signs, which implies that the surface plasmon polariton can only exist at the interface between a dielectric ($\varepsilon_2 > 0$) and a metal ($\varepsilon_1 < 0$). Additionally, the electric field decays as $\exp(-k_2 z)$ into the dielectric and $\exp(-k_1|z|)$ into the metal so that it is maximum at $z = 0$.

By combining Maxwell curl equations 12a and 12b we obtain the following wave equations,

$$\nabla^2\mathbf{E} - \frac{\varepsilon}{c^2}\frac{\partial^2\mathbf{E}}{\partial t^2} = 0, \tag{41a}$$

$$\nabla^2\mathbf{H} - \frac{\varepsilon}{c^2}\frac{\partial^2\mathbf{H}}{\partial t^2} = 0.4, \tag{41b}$$

where $k_0 = \omega/c$ is the wavenumber in free space. Considering TM-modes, equation 41b becomes into the Helmholtz equation,

$$\frac{\partial^2 H_y}{\partial z^2} + (k_0^2\varepsilon - \beta^2)H_y = 0. \tag{42}$$

Continuity of H_y at the interface implies that expressions 38a and 39a must satisfy equation 42 simultaneously, leading to the following relations

$$\begin{aligned} k_1^2 + k_0^2\varepsilon_1 - \beta^2 &= 0, \\ k_2^2 + k_0^2\varepsilon_2 - \beta^2 &= 0. \end{aligned} \tag{43}$$

By combining equations 40 and 43 we obtain the SPP propagation constant associated with a flat surface interface:

$$\beta = k_0\sqrt{\frac{\varepsilon_1\varepsilon_2}{\varepsilon_1 + \varepsilon_2}}. \tag{44}$$

Equation 44 is also known as the SPP dispersion relation. If we further assume a complex dielectric constant $\varepsilon_1 = \varepsilon_1' + i\varepsilon_1''$ such that $\varepsilon_1'' < |\varepsilon_1'|$, we obtain a complex propagation constant β with

$$\beta' = \frac{\omega}{c}\left(\frac{\varepsilon_1'\varepsilon_2}{\varepsilon_1'+\varepsilon_2}\right)^{1/2}, \tag{45}$$

$$\beta'' = \frac{\omega}{c}\left(\frac{\varepsilon_1'\varepsilon_2}{\varepsilon_1'+\varepsilon_2}\right)^{3/2}\frac{\varepsilon_1''}{2(\varepsilon_1')^2}. \tag{46}$$

3.1.2 Excitation mechanisms of SPP

The dispersion-relation of a propagating wave determines how its frequency and wavenumber are related. To illustrate the dispersion of a TM-mode propagating on a flat metal-dielectric interface, we calculated the scattering produced on a gold-air flat interface by a punctual TM-mode field source (an electric dipole) placed a few nanometers above the interface in the air region. We used the Drude model (equation 27) to simulate the dispersive response of gold. For each frequency value in the range 160 to 1270 THz, we obtained the wavenumber spectrum of the scattered field throughout the interface; each spectrum corresponds to a different row in the dispersion diagram of figure 8. The region of higher intensity (red color) is associated with the SPP resonances.

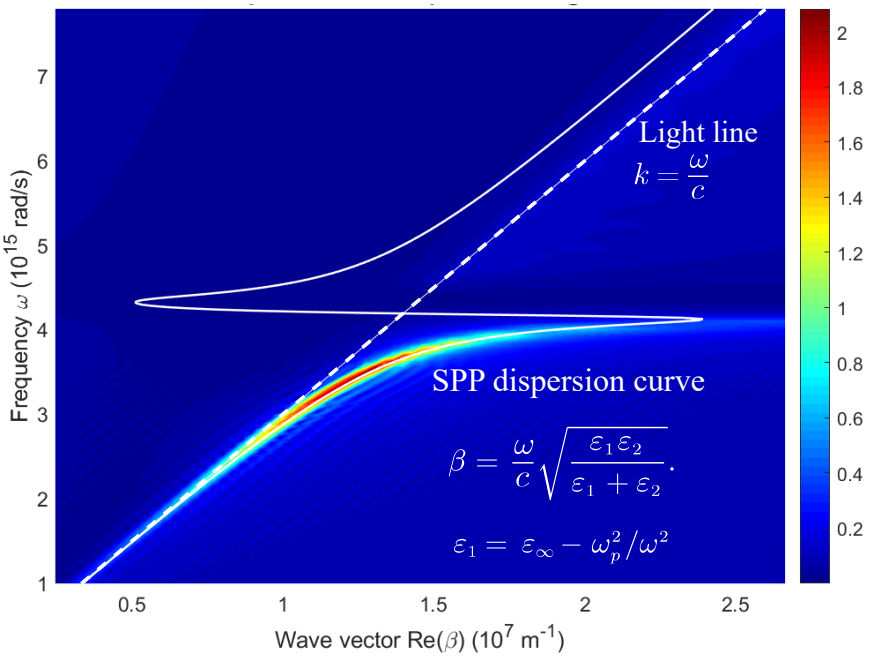

Figure 8. Dispersion diagram corresponding to a gold/air flat interface. The complex dielectric function of gold is calculated with the Drude model using a well known parameters for gold $\varepsilon_\infty = 1$, $\omega_p = 1.3506 \times 10^{16}$, and $\gamma = 1.0769 \times 10^{14}$ Derkachova and Demchenko (2016). The continuous white line corresponds to the dispersion relation of equation 44. The TM field source consists of an electric dipole oriented at 45°. Simulation data were computed using the the commercial software COMSOL multiphysics

Additionally, we displayed the SPP dispersion relation of equation 44 (continuous white line) and the light-line (dashed white line). This latter represents the dispersion-relation of an electromagnetic wave propagating in free-space, $\omega = ck$. Since SPPs are bound modes, the SPP resonance region corresponds to the section of the dispersion curve lying to the right of the light-line. Therefore, for any frequency ω, the SPP wavevector β is always larger than that of the incident photons; this is $\beta > \sqrt{\varepsilon_1}\omega/c$. Nevertheless, it is possible to couple incident light into SPPs using a mechanism that consists of matching the SPP resonance wavenumber with that of the incident-light by adding an amount of momentum Δk to this latter. For this reason, this coupling method is called phase-matching.

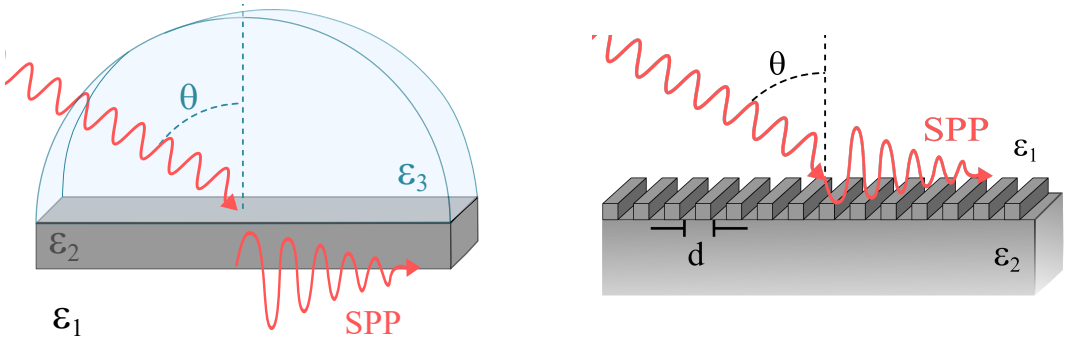

(a) Kretschmann-Raether (b) Grating phase-matching

Figure 9. SPP-coupling configurations.

There are two main methods of phase-matching: attenuated total reflection (ATR) and grating coupling. Otto and Kretschmann-Raether are the two most commonly used ATR configurations; they both consist of a three layers array; two insulators of different dielectric constants $\varepsilon_3 > \varepsilon_1$ (generally glass and air) and a thin metal film of dielectric constant ε_2. In the Kretschmann-Raether configuration, the metal is placed in-between the dielectrics (see figure 9(a)), a light beam of frequency ω strikes the interface between the insulator of higher dielectric constant and the metal ($\varepsilon_3\varepsilon_2$-interface). The angle of incidence θ at the upper interface is such that the in-plane momentum of light $k_x = \sqrt{\varepsilon_3}(\omega/c)\sin\theta$ is sufficient large to excite the SPP at the lower interface ($\varepsilon_2/\varepsilon_1$ interface). Therefore, in a Kretschmann-Raether configuration, we can express the phase-matching condition as

$$\sqrt{\varepsilon_3}\frac{\omega}{c}\sin(\theta) \approx \beta, \tag{47}$$

where β is the SPP wavevector at the lower interface ($\varepsilon_2\varepsilon_1$-interface). We simulated the coupling of plane waves into SPPs, using a three-layer system made of air (ε_1), gold (ε_2), and glass (ε_3) in a Kretschmann-Raether configuration. To identify the SPP resonance, we plot the reflectivity on the glass-gold interface as a function of the incidence angle θ; as shown in figure 10, the SPP resonance takes place at the coupling angle θ_c where the sharp minimum occurs.

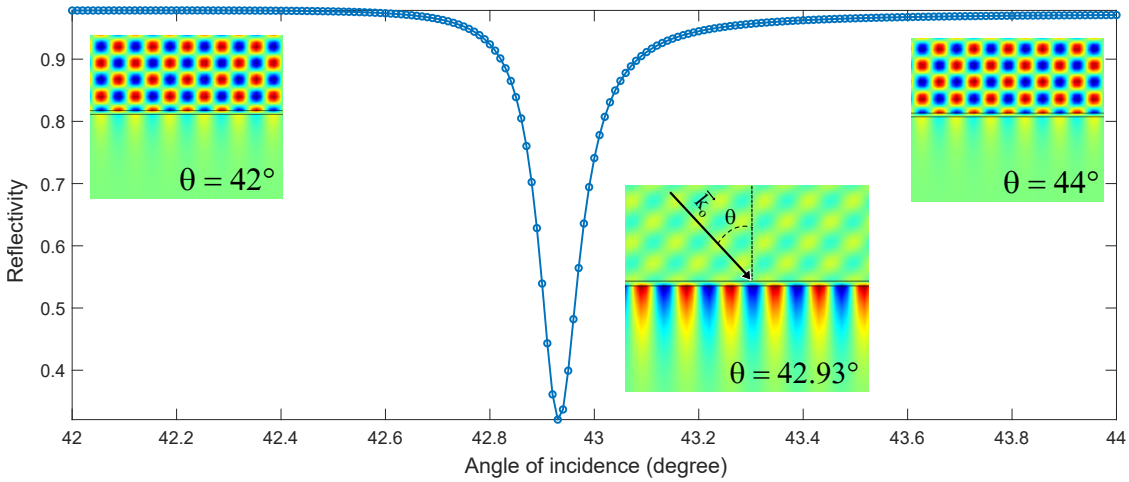

Figure 10. Reflectivity as a function of the angle of incidence in Kreschmann-Raether configuration. The minimum is associated to the SPP-excitation. The insets show the magnetic field magnitude in the Kreschmann-Raether configuration.

For an specific set of frequency values, we computed the reflectivity and determined the coupling angles. Then we calculated the wavenumber of the corresponding electromagnetic field through the air-gold interface. Markers in figure11 display our numerical results; the black squares correspond to the SPP-resonances while the white circles correspond to unbound propagating waves. Additionally we plot the dispersion-curve using equation 44 (black line) and the dispersion relations in air and glass (blue and red straight lines). As expected, the SPPs can only be excited in the dispersion-curve section that is left-limited by the ε_1 light-line and right-limited by the ε_3 light-line.

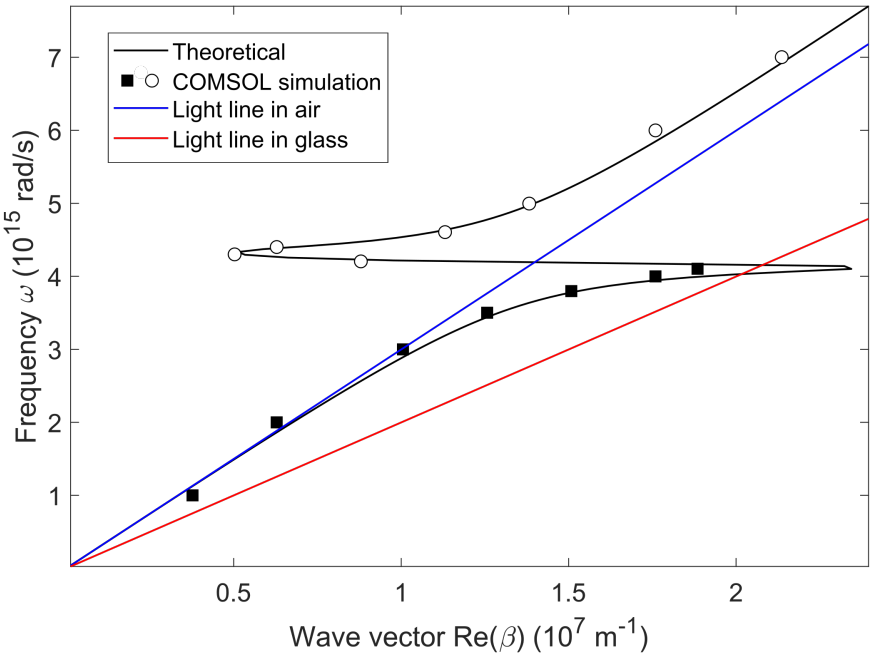

Figure 11. Allowed region for SPP-excitation on an Air-Glass interface. The Drude parameters for Gold are $\varepsilon_\infty = 1$, $\omega_p = 1.3506 \times 10^{16}$, and $\gamma = 1.0769 \times 10^{14}$ Derkachova and Demchenko (2016)

3.1.3 Grating-Assisted SP-Laser Coupling

Phase matching can also be achieved through the assistance of gratings or structured surfaces with a periodic pattern of grooves (see figure 9(b)). For light striking at oblique incidence, the phase-matching between the SPP wavevector β and the in-plane light momentum $k_x = (\omega/c)\sqrt{\varepsilon_1}\sin\theta$ takes place whenever the following condition is fulfilled.

$$\beta = \frac{\omega}{c}\sqrt{\varepsilon_1}\sin\theta_c \pm pg = \pm\frac{\omega}{c}\sqrt{\frac{\varepsilon_1\varepsilon_2}{\varepsilon_1+\varepsilon_2}}, \tag{48}$$

where θ_c is the coupling angle, $g = 2\pi/d$ is the grating wavevector with d the grating period, and p is an integer representing the multiple diffraction orders. As in the case of ATR, the SPP resonance appears as a sharp minimum in the reflectivity plot.

A more general situation occurs when irradiating substrates of random roughness; in that case, the phase-matching can be attained if the scatterers impart to the incident photons the necessary amount of momentum Δk_x. Comparing with a flat interface, the SPP dispersion-diagram of a rough surface exhibits different trends that result from combining the SPP wavevector β with the

multiple diffraction orders of the surface spectrum components. It is possible to represent any surface roughness through its Fourier spectrum as a linear combination of spatial frequency components k_i. For instance, let us consider a surface whose Fourier spectrum consists of only two wavevectors $\{k_1, k_2\}$. Figure 12 shows the first dispersion terms.

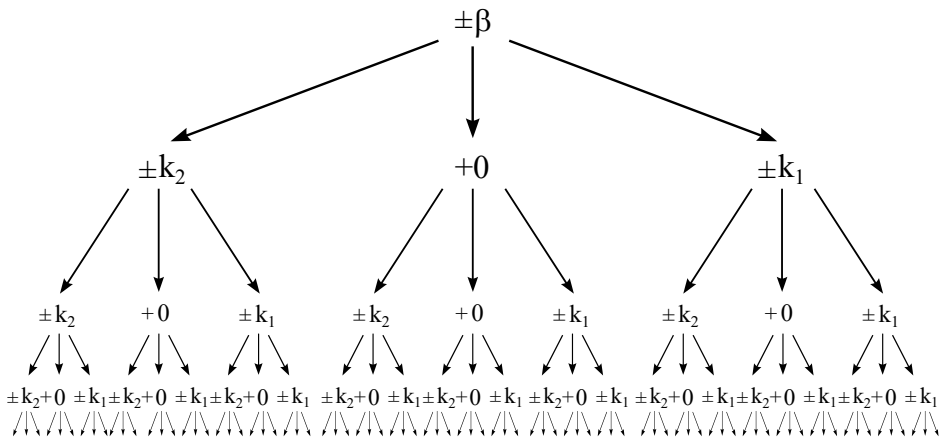

Figure 12. This diagram shows the possible combinations between the SPP wave-vector ($\pm\beta$) and a surface whose Fourier spectrum is spanned into two wave-vectors ($\pm k_1$, $\pm k_2$).

In general, we can obtain all the combinations that result from coupling the SPP wave-vector β with the surface spectrum components, k_i, of an arbitrary surface through the following expression.

$$\pm \beta \pm \sum_i p k_i. \tag{49}$$

Here, the diffraction orders are expressed by the product of k_i with the parameter p, which can take any integer value. To illustrate the influence of the surface shape in the SPP coupling, we compare the dispersion diagram corresponding to the flat surface (figure 8) with those of a sinusoidal grating made of one and three spatial frequencies; figures 13 (a) and (b), respectively.

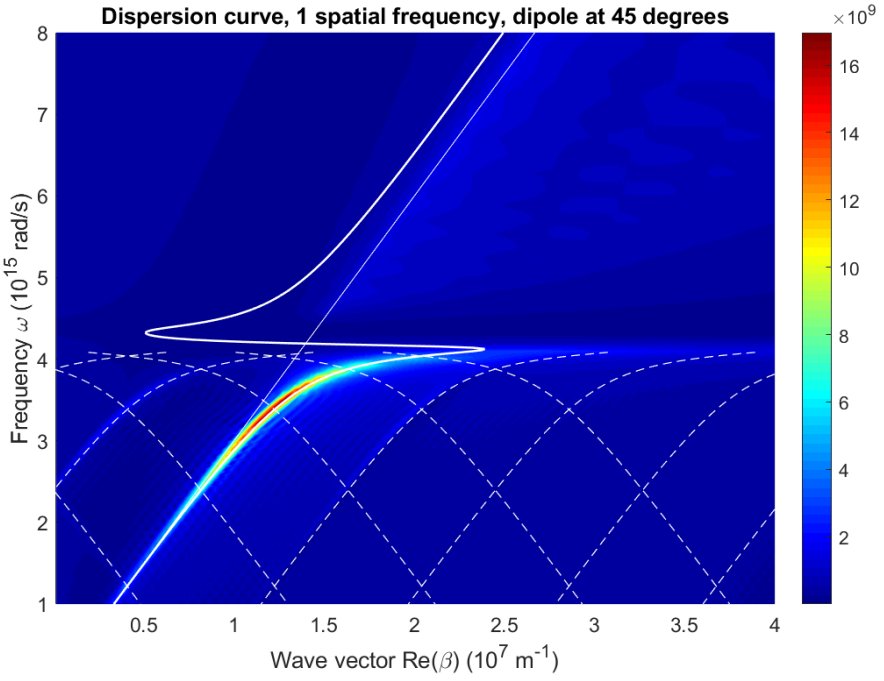

(a)

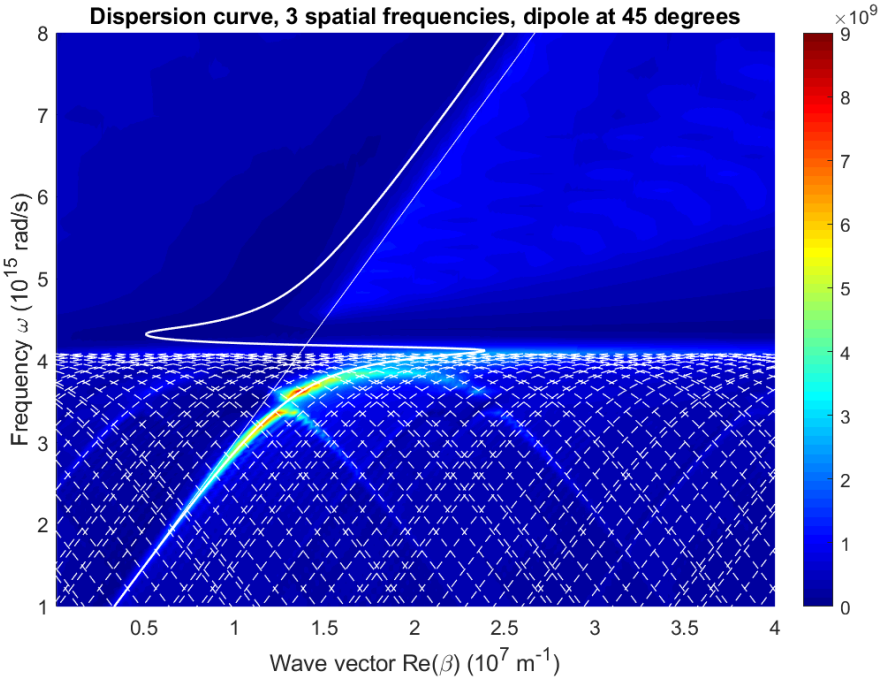

(b)

Figure 13. Dispersion diagram of a periodic surface with one (a) and three (b) spatial frequencies. The coupling between the SPP wave vector β and grating vector $k = 2\pi/\Lambda$ is indicated by the dashed white lines.

We can notice how the dispersion-diagram changes when increasing the number of surface spectrum components; particularly, new resonances appear along both sides of the section associated with the SPP-resonance in the dispersion curve (continuous white curve). Expression 49 determines

the exact distance between those new resonances. Moreover, the SPP-resonance intensity decreases, which suggests that the surface roughness suppresses the SPP-coupling efficacy.

3.1.4 Interference between laser light and SPP

In 1982 Keilmann and Bai introduced a model to explain the formation of LIPSS, which is based on interference between the incident laser light and SPPs (Keilmann and Bai, 1982). To develop this model, let us start by considering two electromagnetic waves of the same frequency, $\mathbf{E}_1$ and $\mathbf{E}_2$, propagating along the wave vectors $\mathbf{k}_1$ and $\mathbf{k}_2$, respectively. If those waves superpose, the time-averaged intensity of the superposition, $I = |\mathbf{E}_1|^2 + |\mathbf{E}_1|^2 - 2\mathbf{E}_1 \cdot \mathbf{E}_2 \cos((\mathbf{k}_1 - \mathbf{k}_2) \cdot \mathbf{r})$, will produce an interference fringe pattern. The wavevector normal to the surfaces of maximum intensity, $\mathbf{G} \equiv \mathbf{k_1} - \mathbf{k_2}$, determines the fringe separation, $d = 2\pi/|\mathbf{G}|$. Similarly, a SPP confined to the interface ($z = 0$) of wavevector $\mathbf{k}_s$ may interfere with the in-plane incident field of wavevector $\mathbf{k}_t$; the superposition of those fields will produce a interference pattern that is imprinted on the irradiated surface as a fringe relief whose grating wavevector is $\mathbf{g} = \mathbf{k}_s - \mathbf{k}_t$. Figure 14(a) depicts the geometrical configuration of the wavevectors involved in this LIPSS formation model.

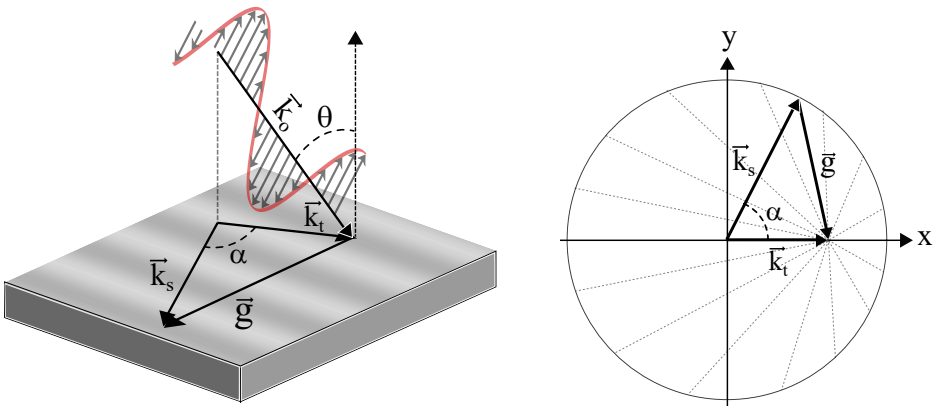

(a)

(b) Possible configurations of incident and SPP wavevectors

Figure 14. Schematic representation of the possible configuration of the wavevectors $\mathbf{k}_s$, $\mathbf{k}_t$, and $\mathbf{g}$.

The circular diagram in figure 14(b) illustrates the mutual orientation of the vectors $\mathbf{k}_s$, $\mathbf{k}_t$, and $\mathbf{g}$. The dashed lines, represent the modulus that the grating-vector $\mathbf{g}$ may take for different configurations of $\mathbf{k}_s$ and $\mathbf{k}_t$, where α represents the angle between them. Hence, the modulus of $\mathbf{g}$ is given by

$$|\mathbf{g}| = (|\mathbf{k}_t|^2 + |\mathbf{k}_s|^2 - 2|\mathbf{k}_t||\mathbf{k}_s|\cos(\alpha))^{1/2}. \tag{50}$$

The simplest and most frequent case (Bonch-Bruevich *et al.*, 1992) occurs when $\mathbf{k}_s$ and $\mathbf{k}_t$ are parallel ($\alpha = 0,\ \pi$), then the SPP travels transverse to the grating, in that case the grating vector modulus of equation 50 reduces to $|\mathbf{g}| = |\mathbf{k}_s| \pm |\mathbf{k}_t| = |\mathbf{k}_s| \pm |\mathbf{k}_o \sin(\theta)|$, the $\pm$ sign implies the possibility of having SPPs traveling in both forward and backward directions. Therefore, the fringe period $\Lambda = 2\pi/|\mathbf{g}|$ can be written as

$$\Lambda = \frac{2\pi}{|\mathbf{k_s}| \pm |\mathbf{k_o}| \sin\theta}, \tag{51}$$

considering, $\lambda = 2\pi|\mathbf{k_o}|^{-1}$, and $\lambda_s = 2\pi|\mathbf{k_s}|^{-1}$, LIPSS periodicity is

$$\Lambda_{\pm} = \frac{\lambda}{\frac{\lambda}{\lambda_s} \pm \sin\theta}. \tag{52}$$

In accordance with equation 52, at normal incidence, LIPSS periodicity reduces to the SPP wavelength ($\Lambda = \lambda_s$). Furthermore, assuming that $|k_s|$ is given by equation 44, and the imaginary part of the electric permittivity is smaller than the absolute value of the real one ($\varepsilon'' < |\varepsilon'|$), the SPP-wavelength is given by

$$\lambda_s = \lambda\sqrt{\frac{\varepsilon' + \varepsilon_d}{\varepsilon'\varepsilon_d}}. \tag{53}$$

Although the SPP dispersion-relation of equation 53 does not contemplate the influence of the roughness on the SPP propagation, we must recall the fundamental role that the surface roughness plays in imparting the momentum mismatch necessary to excite the SPPs. This model has been widely used and can be extended to semiconductors and dielectrics by the hypothesis that during the ultra-short laser irradiation, the optical properties of the non-metallic materials can turn metallic temporally, which would permit the excitation of SPPs.

3.2 The efficacy factor theory

In this section, we discuss another LIPSS formation model known as the efficacy factor theory, which is a first-principle theory developed in 1983 by J. E. Sipe and co-workers, that addresses the interaction between a TM- or TE-polarized wave and a microscopically rough surface (Sipe *et al.*, 1983). According to this model, when a plane wave strikes on the material surface, inhomogeneous energy deposition occurs; then, LIPSS will grow where the absorbed energy is the largest. Consequently, the formation of LIPSS follows the absorbed energy profile.

All calculations within this framework are carried out in the two-dimensional spatial-frequency domain, spanned by the wavevectors $\mathbf{k} = (k_x, k_y)$, parallel to the substrate surface. As pointed out in section 3.1.3, any surface roughness can be represented through its Fourier spectrum; under this premise, $b(\mathbf{k})$ is a spectrum-dependent function that represents the amplitude of the roughness at $\mathbf{k}$. The energy absorbed by the substrate, $A(\mathbf{k})$, is proportional to the product $\eta(\mathbf{k}, \mathbf{k}_i) \times |b(\mathbf{k})|$. Here $\eta(\mathbf{k}, \mathbf{k}_i)$ is a scalar function that represents the efficacy with which the surface roughness leads to inhomogeneous absorption of energy (Sipe *et al.*, 1983); for this reason it is known as the efficacy factor. The dielectric interface properties and the laser parameters determine the value of $\eta(\mathbf{k}, \mathbf{k}_i)$, which exhibits sharp peaks at symmetrical wave-vectors; conversely, $b(\mathbf{k})$ behaves as a slowly varying function of $\mathbf{k}$ if the surface has a homogeneously distributed roughness. Consequently, the function that drives the LIPSS formation is the efficacy factor.

For multipulse irradiation; as LIPSS start to grow, the value of $b(\mathbf{k})$ changes to follow the peaks of $\eta(\mathbf{k}, \mathbf{k}_i)$, which in turn enhance the beam absorption. Then, the LIPSS formation mechanism becomes a feedback process. Nowadays, the Sipe theory is one of the most widely accepted models for explaining LSFL formation (Bonse *et al.*, 2017; Dufft *et al.*, 2009).

3.2.1 Efficacy factor map

For convenience, we based our efficacy factor calculations on a set of simplified equations that Bonse and co-workers summarized in (Bonse *et al.*, 2005) from the original expressions developed by Sipe *et al.* The diagram in figure 15 represents the basic components of the efficacy-factor theory; a linearly polarized electromagnetic wave, propagating through free space, strikes a surface with incidence angle θ. The electric field polarization is assumed to be either parallel (p) or perpendicular

(s). The vector $\mathbf{k}_i = \tilde{\omega}\sin(\theta)\hat{y}$ represents the projection of the incident wavevector on the substrate surface. Just above the plane $z = 0$, there is a layer of thickness l_s containing the surface roughness.

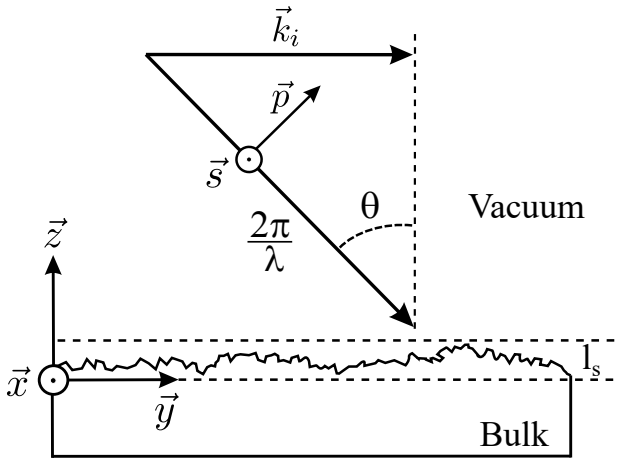

Figure 15. Schematic diagram of a plane wave striking onto a rough surface in the framework of the efficacy factor theory.

The roughness size l_s must satisfy two inequalities; it should be smaller than the wavelength, $\frac{2\pi}{\lambda} l_s \ll 1$, and also it should be smaller than the periodicity of the inhomogeneous energy absorption length, $|\mathbf{k}| l_s \ll 1$. Sipe *et al.* use a statistical model to describe the roughness as a binary function $b(\vec{\rho}) = b(x, y)$ in the space domain (see fig.16), which assigns the values 1 and 0 for the filled and unfilled zones respectively.

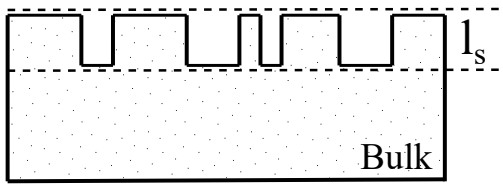

Figure 16. Representation of a binary rough surface.

The function $b(x, y)$ represents the surface roughness via two parameters; the filling factor (F) and shape factor (s). The first one represents the average of $b(\vec{\rho})$, $F \equiv \langle b(\vec{\rho})\rangle$ (Skolski, 2010). Assuming the roughness is uncorrelated at large distances ($|\vec{\rho} - \vec{\rho}\,'| \to \infty$) we note that $\langle b(\vec{\rho}) b(\vec{\rho}\,')\rangle \to F^2$. Whereas for short distances ($|\vec{\rho} - \vec{\rho}\,'| \to 0$), $\langle b(\vec{\rho}) b(\vec{\rho}\,')\rangle \to F$. Hence $\langle b(\vec{\rho}) b(\vec{\rho}\,')\rangle$ can be expressed as

$$\langle b(\vec{\rho}) b(\vec{\rho}\,')\rangle = F^2 + (F - F^2) C(|\vec{\rho} - \vec{\rho}\,'|), \tag{54}$$

where

$$C(\rho) \to \begin{cases} 1 & \text{when} \quad \rho \to 0 \\ 0 & \text{when} \quad \rho \to \infty \end{cases}. \tag{55}$$

Let us introduce the parameter l_t, referred to as the transverse correlation length that characterizes how the filled part of the roughness agglomerates through the expression $\langle b(\vec{\rho})b(\vec{\rho}\,')\rangle$. If $|\vec{\rho}-\vec{\rho}\,'| > l_t$ then $C(|\vec{\rho}-\vec{\rho}\,'|) = 0$ and $\langle b(\vec{\rho})b(\vec{\rho}\,')\rangle = F^2$. While if $|\vec{\rho}-\vec{\rho}\,'| \leq l_t$, then $C(|\vec{\rho}-\vec{\rho}\,'|) = 1$ and $\langle b(\vec{\rho})b(\vec{\rho}\,')\rangle = F$. Therefore, we write $C(\rho) = \Theta(l_t - \rho)$ where Θ is the well-known Heaviside function. Since $F^2 \leq F$ ($F \leq 1$), the filled parts of the roughness tend to agglomerate and form "islands" of radii l_t. Hence, we define the shape factor as the aspect ratio of the filled parts $s \equiv l_t/l_s$.

When the conditions mentioned above are fulfilled, the efficacy factor $\eta(\mathbf{k}, \mathbf{k_i})$ can be calculated as

$$\eta(\mathbf{k}, \mathbf{k_i}) = 2\pi|\nu(\mathbf{k}_+) + \nu^*(\mathbf{k}_-)|, \tag{56}$$

where $\mathbf{k}_\pm = \mathbf{k}_i \pm \mathbf{k}$. The complex function ν is expressed for $s-$polarized light as

$$\nu(\mathbf{k}_\pm, s-\text{pol.}) = [h_{ss}(k_\pm)(\hat{\mathbf{k}}_\pm \cdot \hat{\mathbf{y}})^2 + h_{kk}(k_\pm)(\hat{\mathbf{k}}_\pm \cdot \hat{\mathbf{x}})^2]\gamma_t|t_s(\mathbf{k_i})|^2, \tag{57}$$

while for $p-$polarized light, as

$$\begin{aligned} \nu(\mathbf{k}_\pm, p-\text{pol.}) =& [h_{ss}(k_\pm)(\hat{\mathbf{k}}_\pm \cdot \hat{\mathbf{x}})^2 + h_{kk}(k_\pm)(\hat{\mathbf{k}}_\pm \cdot \hat{\mathbf{y}})^2]\gamma_t|t_x(\mathbf{k_i})|^2 + \\ & h_{kz}(k_\pm)(\hat{\mathbf{k}}_\pm \cdot \hat{\mathbf{y}})\gamma_z\varepsilon t_x^*(\mathbf{k_i})t_z(\mathbf{k_i}) + \\ & h_{zk}(k_\pm)(\hat{\mathbf{k}}_\pm \cdot \hat{\mathbf{y}})\gamma_t t_x(\mathbf{k_i})t_z^*(\mathbf{k_i}) + \\ & h_{zz}(k_\pm)\gamma_z\varepsilon|t_z(\mathbf{k_i})|^2. \end{aligned} \tag{58}$$

For the sake of simplicity, we introduce the normalized wave-vectors $\kappa = \mathbf{k}/\mathbf{k_0}$ so that the

explicit expressions for the inner products of equations 58 and 57 are

$$\hat{\mathbf{k}}_{\pm} \cdot \hat{\mathbf{y}} = \frac{\sin(\theta) \pm \kappa_y}{\kappa_{\pm}}, \tag{59a}$$

$$\hat{\mathbf{k}}_{\pm} \cdot \hat{\mathbf{x}} = \frac{\kappa_x}{\kappa_{\pm}}, \tag{59b}$$

where $\kappa_{\pm} = \sqrt{\kappa_x^2 + (\kappa_y \pm \sin(\theta))^2}$. In (Sipe *et al.*, 1983) the functions h_{ss}, h_{kk}, h_{kz}, h_{zk}, and h_{zz}, were originally expressed in terms of the variables $\tilde{\omega} = k_0$, $\omega_o = \sqrt{k_0^2 - k_{\pm}^2}$, and $\omega = \sqrt{\varepsilon k_0^2 - k_{\pm}^2}$. Using the normalized wave-vectors those functions can be finally written as

$$h_{ss}(k_{\pm}) = \frac{2i\tilde{\omega}}{\omega_o + \omega} = \frac{2i}{\sqrt{1 - \kappa_{\pm}^2} + \sqrt{\varepsilon - \kappa_{\pm}^2}} \tag{60a}$$

$$h_{kk}(k_{\pm}) = \frac{2i\omega\omega_o}{\tilde{\omega}(\omega_o\varepsilon + \omega)} = \frac{2i\sqrt{(\varepsilon - \kappa_{\pm}^2)(1 - \kappa_{\pm}^2)}}{\varepsilon\sqrt{1 - \kappa_{\pm}^2} + \sqrt{\varepsilon - \kappa_{\pm}^2}} \tag{60b}$$

$$h_{zz}(k_{\pm}) = \frac{2ik_{\pm}^2}{\tilde{\omega}(\omega_o\varepsilon + \omega)} = \frac{2i\kappa_{\pm}^2}{\varepsilon\sqrt{1 - \kappa_{\pm}^2} + \sqrt{\varepsilon - \kappa_{\pm}^2}} \tag{60c}$$

$$h_{zk}(k_{\pm}) = \frac{2ik_{\pm}\omega_o}{\tilde{\omega}(\omega_o\varepsilon + \omega)} = \frac{2i\kappa_{\pm}\sqrt{1 - \kappa_{\pm}^2}}{\varepsilon\sqrt{1 - \kappa_{\pm}^2} + \sqrt{\varepsilon - \kappa_{\pm}^2}} \tag{60d}$$

$$h_{kz}(k_{\pm}) = \frac{2i\omega k_{\pm}}{\tilde{\omega}(\omega_o\varepsilon + \omega)} = \frac{2i\kappa_{\pm}\sqrt{\varepsilon - \kappa_{\pm}^2}}{\varepsilon\sqrt{1 - \kappa_{\pm}^2} + \sqrt{\varepsilon - \kappa_{\pm}^2}}, \tag{60e}$$

while the complex functions t_s, t_x, and t_z are given by

$$t_s(\mathbf{k_i}) = \frac{2|\cos\theta|}{|\cos\theta| + \sqrt{\varepsilon - (\sin\theta)^2}}, \tag{61a}$$

$$t_x(\mathbf{k_i}) = \frac{2\sqrt{\varepsilon - (\sin\theta)^2}}{\varepsilon|\cos\theta| + \sqrt{\varepsilon - (\sin\theta)^2}}, \tag{61b}$$

$$t_z(\mathbf{k_i}) = \frac{2\sin\theta}{\varepsilon|\cos\theta| + \sqrt{\varepsilon - (\sin\theta)^2}}. \tag{61c}$$

The functions γ_t and γ_z that involve the roughness parameters s and F, are given by

$$\gamma_z = \frac{\varepsilon - 1}{4\pi\{\varepsilon - (1-F)(\varepsilon-1)[h(s) + Rh_I(s)]\}}, \tag{62a}$$

$$\gamma_t = \frac{\varepsilon - 1}{4\pi\{1 + \frac{1}{2}(1-F)(\varepsilon-1)[h(s) - Rh_I(s)]\}}, \tag{62b}$$

where $R = (\varepsilon - 1)/(\varepsilon + 1)$, and

$$h(s) = \sqrt{s^2 + 1} - s, \tag{63a}$$

$$h_I(s) = \frac{1}{2}[\sqrt{s^2 + 4} + s] - \sqrt{s^2 + 1}. \tag{63b}$$

Figure 17(a) illustrates and example of the efficacy factor map $\eta(\kappa_x, \kappa_y)$ calculated for titanium ($\varepsilon = -79.23 + 10.6i$ (Werner *et al.*, 2009)). Irradiation parameters were set to be $\theta = 0°$ (normal incidence), $\lambda = 1030$ nm, and polarization along the x-axis. Roughness parameters were chosen following the assumption of spherically shaped islands, $s = 0.4$ and $F = 0.1$ (Young *et al.*, 1983).

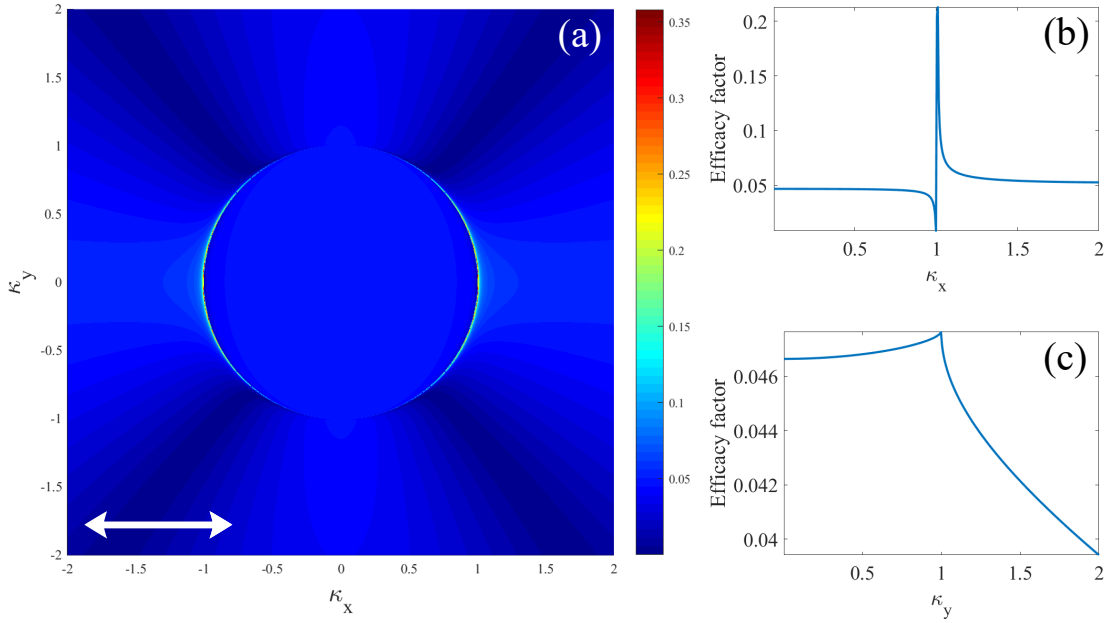

Figure 17. (a) Efficacy factor map of titanium (ε=-79.23 +10.6i at λ = 1030 nm, Werner 2009) irradiated at normal incidence with linearly polarized light (wavelength 1030 nm, polarization indicated by the white arrow). Roughness parameters, s =0.4 and F =0.1. (b) and (c) show the cross section along the normalized κ_x and κ_y axes respectively. Global peak on the κ_x-axis at κ=1.010014 corresponds to LIPSS oriented perpendicular with respect to the polarization and Λ = 1020 nm.

Figures 17 (b) and (c) show the cross-sections along the positive normalized wavevectors $\kappa_x = \lambda/\Lambda_x$ ($\kappa_y = 0$) and $\kappa_y = \lambda/\Lambda_y$ ($\kappa_x = 0$). The feature sharp peak in figure 17(b) exhibits a global maximum at $\lambda/\Lambda_x = 1.010014$. Therefore, according to the efficacy factor theory, the resulting structures correspond to LSFL of 1020 nm, oriented perpendicular to the incident light polarization.

Chapter 4. LIPSS on bismuth and titanium films

4.1 Instrumentation and experimental setup

Figure 18 illustrates the experimental layout we used to produce LIPSS at the Laboratory of Ultrashort Pulse Laser and Processing of Materials at CICESE. The laser source consists of a commercial Ytterbium-doped fiber laser amplifier system (Satsuma Amplitude HP2) that generates linearly polarized pulses of 270 fs at $\lambda = 1030$ nm central wavelength. The repetition rate ranges from one single pulse to 2 MHz. We use a digital delay/pulse generator (SRS DG645) synchronized to the laser to select the exact number of laser pulses. The highest pulse energy is limited to 40 μJ at lower repetition rates and 10 μJ for repetition rates above 500 kHz; the maximum available average power is 20 W. The laser beam waist diameter is approximately $2w_0 = 2.33$ mm (FW1/e^2).

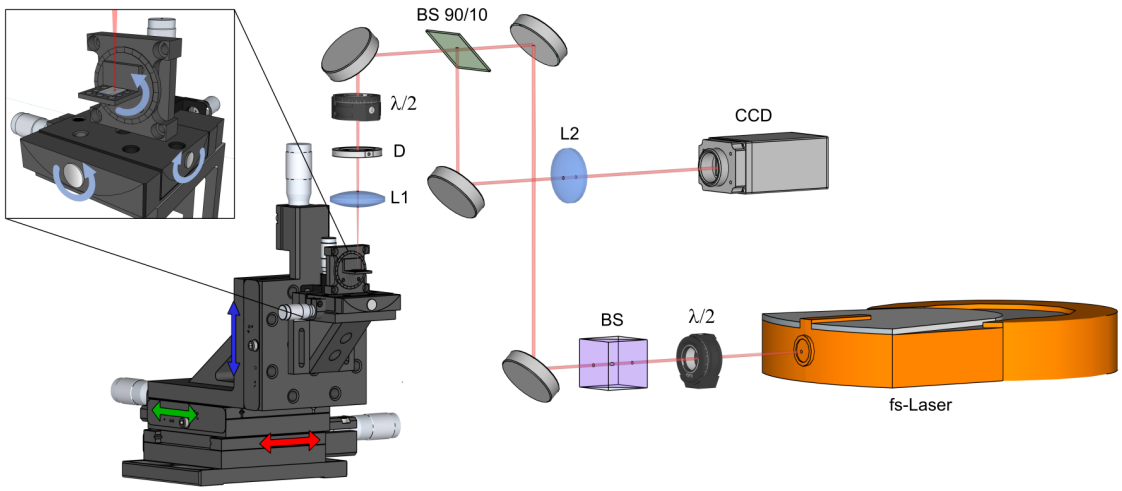

Figure 18. Experimental setup

We used an attenuator consisting of a half-wave plate and a beam-splitter cube to regulate the laser beam intensity. An array of metal-coated mirrors guide the laser beam to a half-wave plate mounted on a rotary stage that controls the beam polarization. A circular-aperture diaphragm may be placed in the light path to trim the laser beam and create a diffraction pattern. A spherical lens, referred to as the processing lens (L1), focuses the beam onto the irradiation plane. A pair of mutually orthogonal goniometers guarantees that the beam hits the sample at normal incidence. The oblique incidence can be achieved by placing the sample on top of a tilting mount (inset in Fig.18). An XYZ-translation stage (Sigma Koki Co. SG-SP20-85) with motorized micrometers allows us to control the laser displacement and sweep velocity.

When the laser hits the sample at normal incidence, the reflected beam travels back along the same optical path until it is divided by a 90/10 beam splitter; a small fraction of light passes through a second lens (L2), which focuses the image of the beam spot on a CCD camera. This setup, known as the equivalent target system, allows us to determine the beam spot shape and size on the irradiation plane.

The electric field of each pulse possesses a Gaussian distribution in space and time, which can be expressed as follows.

$$E = E_0 e^{-i\omega t} e^{-\left(\frac{r}{w}\right)^2} e^{2\ln(2)\left(\frac{t}{\tau}\right)^2}, \tag{64}$$

where r is the radial distance from the center axis of the beam, τ is the pulse duration, and w corresponds to the pulse intensity width at $1/e^2$. By applying the Fresnel diffraction theory, we can obtain the electric field of the pulse propagating through a circular-aperture diaphragm (D) followed by the processing lens (L1),

$$E = E_0 e^{-i\omega t} \frac{i2\pi r_d}{\lambda z} e^{-2\ln(2)\left(\frac{t}{\tau}\right)^2} e^{-\left(\frac{ikr^2}{2z}\right)} \int_0^{r_{dia}} e^{-\left(\frac{\rho}{w}\right)^2} e^{\frac{ik\rho^2}{2f}} e^{-\frac{ik\rho^2}{2z}} J_0\left(\frac{k\rho r}{z}\right) \rho d\rho, \tag{65}$$

here r_d and f represent the diaphragm radius and the lens focal-length. Therefore, we obtain the local fluence $\Phi(r)$ profile by integrating the laser intensity $I = \frac{1}{2}\varepsilon_0 c|E|^2$ over the pulse duration,

$$\Phi(r) = \int_{-\infty}^{\infty} I(r)dt = \sqrt{\frac{\pi}{4\ln(2)}}\tau I(r). \tag{66}$$

4.1.1 Bismuth and titanium films

The samples we used to carry out the experiments consist of bismuth and titanium films with an approximately 400 nm thickness, fabricated at the Institute for Applied Sciences and Technology of UNAM. The fabrication technique consists of DC-magnetron sputtering deposited onto cleaned glass substrates from a target (3-inch diameter, 1/8-inch thick). Commercial argon gas was used as the sputtering environment. The vacuum base and deposition pressures were 10^{-6} mBar and

8.8×10^{-4} mBar, respectively. The target–substrate separation was fixed to be 8 cm. In the case of titanium films, the cathode voltage and power were set to be 300 V and 150 W for 36 seconds, while in the case of the bismuth films, they were 267 V and 10 W for 6 minutes.

As mentioned in section 2.1, when irradiating metals with a pulsed laser between the infrared and ultraviolet regions, the electrons thermalize first their kinetic energy via electron-electron scattering in the order of a few femtoseconds. Then, they transfer their thermal energy to the lattice by electron-phonon coupling, in a timescale that is approximately two orders of magnitude longer. Nonetheless, thermalization with the environment occurs much long after; hence, thermal energy accumulates upon multiple pulses, leading to undesired effects. For this reason, we computed the thermal diffusion time of titanium and bismuth to prevent our samples from those thermal effects according to the list of properties shown in table 1 and the setup details mentioned above. We found that the maximum repetition rates are approximately 14.88 kHz for titanium and 10.54 kHz for bismuth. Therefore we decided to carry out all of our experiments using a repetition rate of 5 kHz for both materials.

Table 1. Optical and thermal properties of bismuth and titanium.

Magnitude	Symbol and units	Ti	Bi	Ref.
Thermal conductivity	κ (W/m·K)	21.9	7.87	(Lide, 2003)
Specific heat capacity	C_p (J/gK)	0.522	0.122	(Lide, 2003)
Density	ρ (10^6 g/m^3)	4.51	9.79	(Lide, 2003)
Thermal diffusivity	$a = \frac{\kappa}{\rho C_p}$ (10^{-5} m^2/s)	0.9302	0.6589	calculated
Refractive index at 1030 nm	n	0.59408	0.34951	(Werner, 2009)
Extinction coefficient	k	8.9209	8.3691	(Werner, 2009)
Absorption coefficient	$\alpha = \frac{4\pi k}{\lambda}$ (10^7 m^{-1})	10.8838	10.2106	calculated
Optical penetration depth	$\delta_p = 1/\alpha$ (nm)	9.1880	9.7937	calculated
Thermal diffusion length	$\chi = \sqrt{2a\tau}$ (nm)	2.2412	1.8863	calculated
Melting point	(K)	1941	544.7	(Lide, 2003)

4.2 Dielectric characterization

We conducted a characterization of the bismuth and titanium dielectric functions by fitting the Drude-Lorentz model to SE-data obtained experimentally (see section 2.2.5). To estimate the Drude-Lorentz parameters corresponding to our bismuth samples, we used an ellipsometer model alpha-SE to acquire SE-data in three different spots within a non-irradiated bismuth film. The ellipsometer beam wavelength ranges from 380 nm to 890 nm. The SE-data was processed using the software CompleteEASE to obtain the pseudo-dielectric function $\langle\varepsilon\rangle$ as a first approximation.

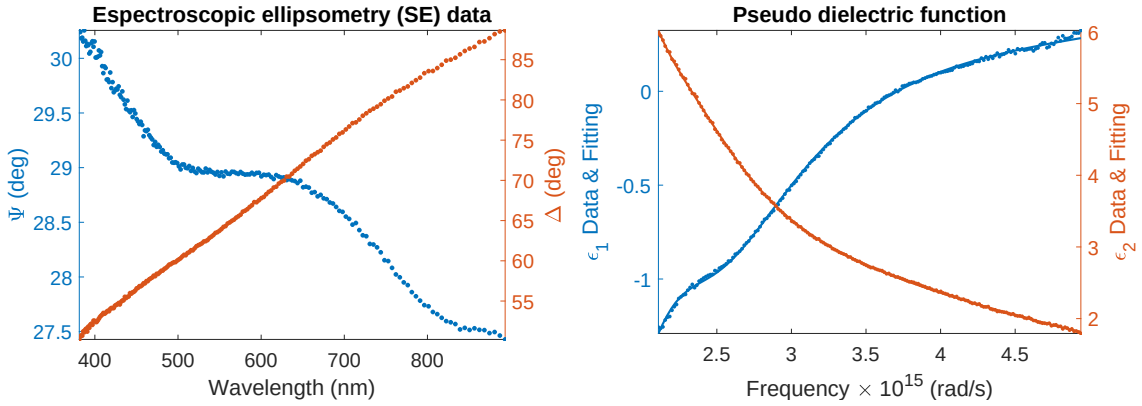

(a) (b)

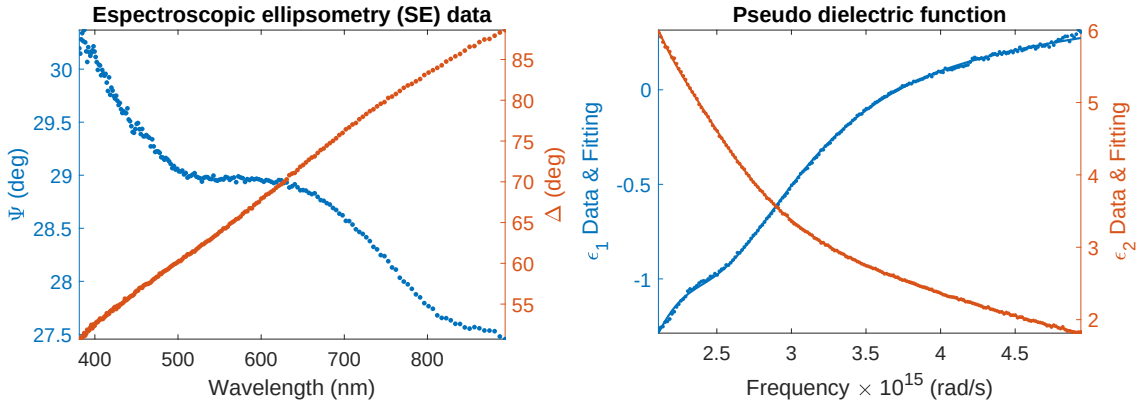

(c) (d)

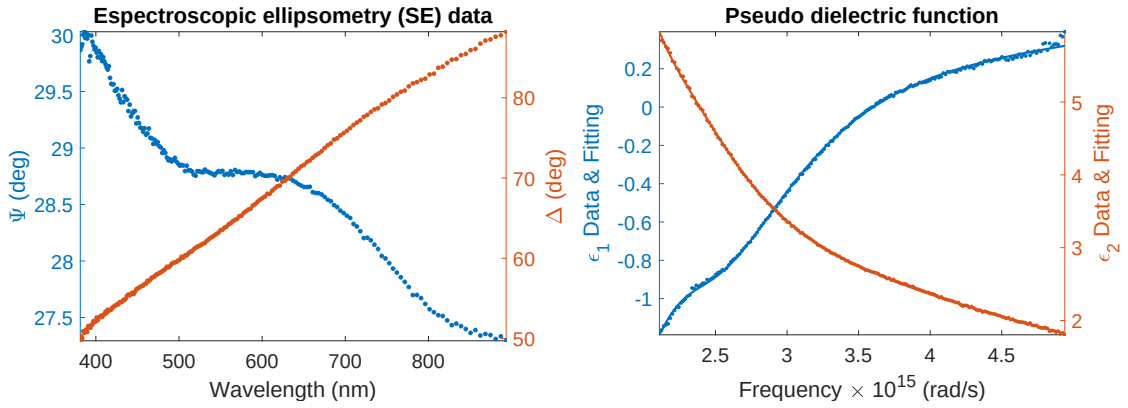

(e) (f)

Figure 19. Spectroscopic ellipsometry measurements in bismuth. Graphs (a), (c), and (e) show the amplitude ratio and phase difference (Ψ and Δ). Graphs (b), (d), and (f) show the real (ε_1) and imaginary (ε_2) parts of the corresponding pseudo-dielectric functions. On top of the experimental points, it is plotted the curve resulting from fitting the Drude-Lorentz model using the parameters of table 2

Table 2. Fitting parameters to model the dielectric constant of bismuth and titanium using the Drude-Lorentz model (one Drude and three Lorentz terms). ε_∞ and f_j are dimensionless while ω_p, Γ_D, $\omega_{o,j}$ and Γ_j are expressed in 10^{15} rad/s.

Spot 1			Spot 2			Spot 3		
ε_∞	ω_j	Γ_D	ε_∞	ω_j	Γ_D	ε_∞	ω_j	Γ_D
1.4976	3.4683	0.0136	1.4953	3.3619	0.014	1.5162	3.4336	0.0103
f_j	$\omega_{o,j}$	Γ_j	f_j	$\omega_{o,j}$	Γ_j	f_j	$\omega_{o,j}$	Γ_j
2.2966	1.6912	0.5545	3.1741	1.6315	0.7028	2.5983	1.6721	0.6389
0.9061	2.3269	1.2308	0.764	2.3513	1.2254	0.8285	2.3459	1.2479
3.72	4.4389	8.6328	3.5561	4.4763	8.4565	3.6284	4.4963	8.6519

Figures 19-(a, c, and e) show the values of SE amplitude ratio (Ψ) and phase difference (Δ) as a function of the wavelength while figures 19-(b, d, and f) show the plots corresponding to the real and imaginary parts of the pseudo-dielectric constant as a function of frequency ω. We used a least-square method to determine parameters that minimize the mean square error (MSE) between the Drude-Lorentz model (eq.28) and our experimental data. Table 2 presents the parameters corresponding to the best-fitting that we found, consisting of one Drude and only three Lorentz terms. It is worth mentioning that the MSE profile could have not a single minimum but many other local minima. For this reason, we should regard the parameters that result from the curve fitting rather as a numerical representation of data than the actual atomic-oscillators parameters. Additionally, it is convenient to choose good starting values to achieve a fit as good as possible.

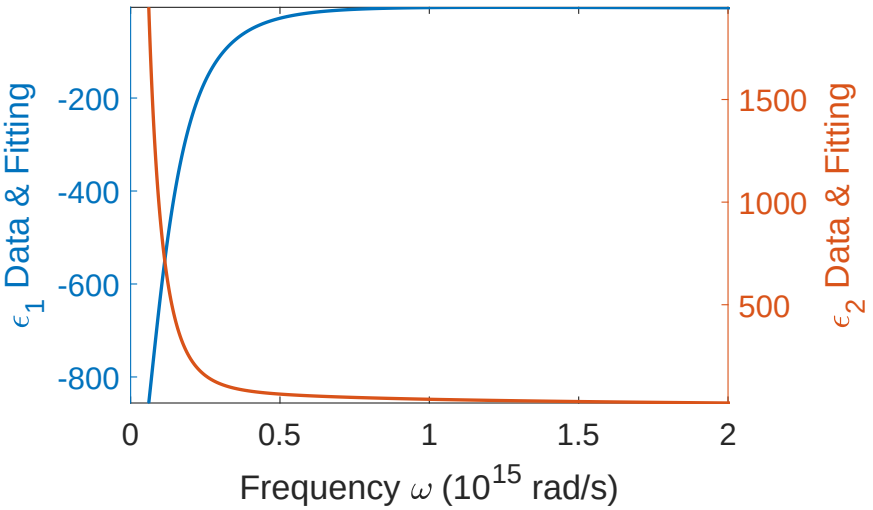

Figure 20. Titanium complex dielectric function ($\tilde{\varepsilon}_{Ti} = \varepsilon_1 + i\varepsilon_2$) respect to the frequency. On top of the experimental points, the resulting fitting curve is plotted using one Drude and three Lorentz terms (RMSE = 0.017). Data available from (Rakic1998)

On the other hand, we used SE-data provided by (Rakić *et al.*, 1998), in the range from 0.2 μm to 31 μm, to fit the Drude-Lorentz parameters for titanium. Figure 20 shows both the fitting and experimental data. Table 3 shows the Drude-Lorentz parameters that we will use to simulate the bismuth and titanium dielectric functions.

Table 3. Fitting parameters of the Drude-Lorentz model (Eq.28) with five Lorentz terms. ε_∞ and f_j are dimensionless whilst ω_p, Γ_D, $\omega_{o,j}$ and Γ_j are expressed in 10^{15} rad/s.

Bismuth			Titanium		
ε_∞	ω_p	Γ_0	ε_∞	ω_j	Γ_j
1.4992	3.4212	0.0126	1.0005	4.2608	0.1246
$A_j(\varepsilon_s - \varepsilon_\infty)$	ω_j	Γ_j	$A_j(\varepsilon_s - \varepsilon_\infty)$	ω_j	Γ_j
2.6897	1.6649	0.6321	79.1573	1.1812	3.4611
0.8329	2.3414	1.2347	1.5828	3.8117	2.5288
3.6348	4.4705	8.5804	8.7225	2.3453	3.8180

4.3 Ablation threshold

In section 2.1 we introduced the basis of pulsed laser ablation; this phenomenon is driven by the laser fluence, defined as the ratio of the delivered pulse energy to the beam cross-section area or, equivalently, as the laser intensity integrated over the pulse duration (Eq.66). Since LIPSS formation

occurs at a fluence value below that of the ablation, we have to determine the minimum laser fluence to start the ablation process, known as the ablation threshold fluence (Φ_{th}).

Yong Jee *et al.* studied the accumulation dependence of damage on a single-crystal metal irradiated with a ns-pulse laser (Jee *et al.*, 1988a) and observed different damage morphologies like slip-line formation, ripple patterns, flat melting, and boiling. They also noticed that the threshold fluence value decreases as the number of laser pulses N increases. That observation led them to develop a phenomenological model that treats the pulse laser ablation as a cumulative process; that model relates the single-pulse ablation threshold $\Phi_{th}(1)$ with the multi-pulse ablation threshold $\Phi_{th}(N)$ via the following power-law equation (Jee *et al.*, 1988a; Krüger *et al.*, 2007)

$$\Phi_{th}(N) = \Phi(1)N^{(\xi-1)}, \tag{67}$$

where ξ is called the incubation factor, a coefficient associated with the storage cycle of thermal stress-strain energy induced by each laser pulse. Usually, the sign of the exponent $(\xi-1)$ is negative, which means that $\Phi_{th}(N)$ is inversely proportional to N; consequently, when the number of pulses tends to infinity, the threshold fluence goes to zero. This fact has led some authors to propose alternative models that add a constant offset representing the threshold fluence for an infinite number of pulses (Neuenschwander *et al.*, 2013). Nevertheless, for metals, there is no better fit than that of the values obtained by equation 67 (Neuenschwander *et al.*, 2012). Regarding the nature of the incubation mechanism, some authors (Neuenschwander *et al.*, 2013; Niso *et al.*, 2014a) have suggested that after multiple pulses, an increase in the surface roughness, due to the accumulation of surface defects, facilitates absorption of the next coming laser pulses, which enhances ablation and material removal. In later sections, we will explore this idea in more detail.

To determine our bismuth sample ablation threshold, we used the system shown in figure 18 to carry out an irradiation matrix, which consists of a series of punctual irradiations varying the energy pulse E_p and the number of pulses N (see figure 21). The processing lens focal-length and the diaphragm radius were set to be 75 mm and 0.75 mm, respectively. The chosen pulse energy values were 2.5μJ, 5μJ, 10μJ, 15μJ, and 16 μJ; while the number of applied pulses were 5000, 10000, 20000, 30000, 40000, and 50000. As shown in figure 21, the ablated craters become broader and deeper whether the energy or number of pulses increases.

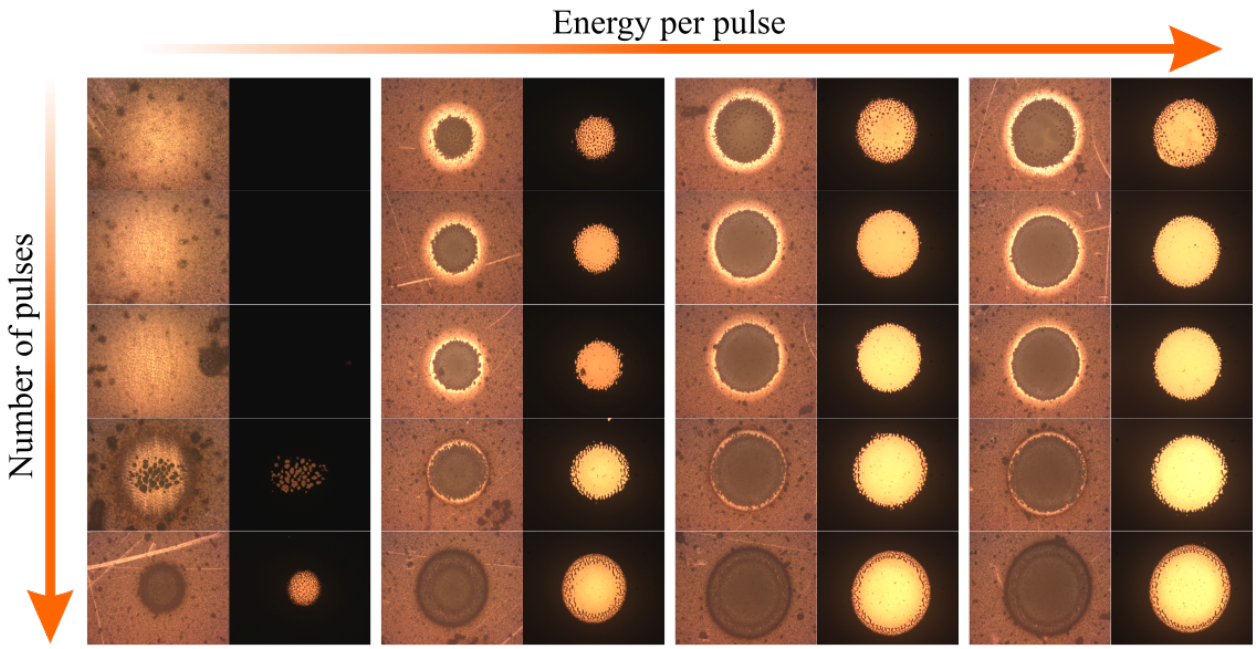

Figure 21. Example of an irradiation matrix on bismuth; each row corresponds to N =10, 50, 100, 500, and 1000. While each column corresponds to E_p = 1 μJ, 2 μJ, 5 μJ, 9 μJ, and 10 μJ. For a given N and E_p values, we show the reflected-light (right-side) and transmitted-light (left-side) micrographs.

As shown in figure 22, if we know E_p and N, we are able to determine the ablation threshold fluence, by measuring the radius of the ablated crater (r_{th}) and directly correlate it with the corresponding fluence value $\Phi(r_{th})$ calculated from equation 66.

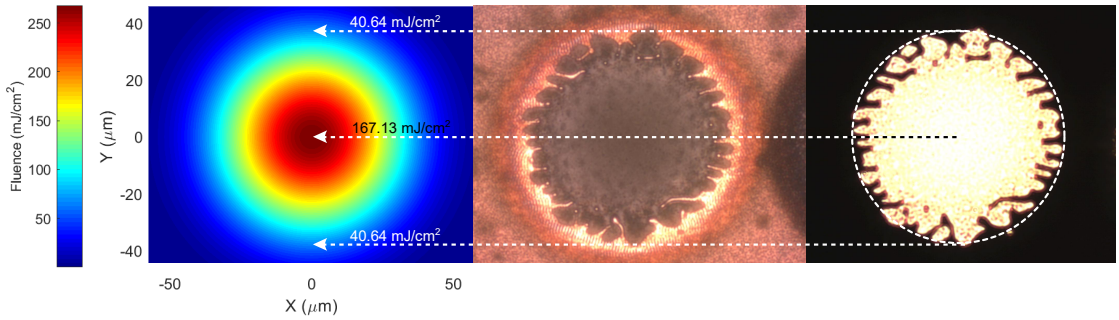

Figure 22. Fluence distribution over an ablation crater.

By numerically solving equations 65 and 66, we calculated the fluence profiles for the different values of the number of pulses N and energy per pulse E_p that we used to produce the irradiation matrix. The graphs in figure 23 show the fluence profiles for the different values of E_p but the same N. The circular markers indicate the laser fluence calculated at the crater radius for a given pulse energy, all material within that radius is ablated hence that calculated fluence corresponds to the ablation-threshold for a given energy. Since all markers have approximately the same value, we

demonstrated that the average ablation threshold (see horizontal lines in figure 23) does not depend on the energy per pulse but the number of pulses.

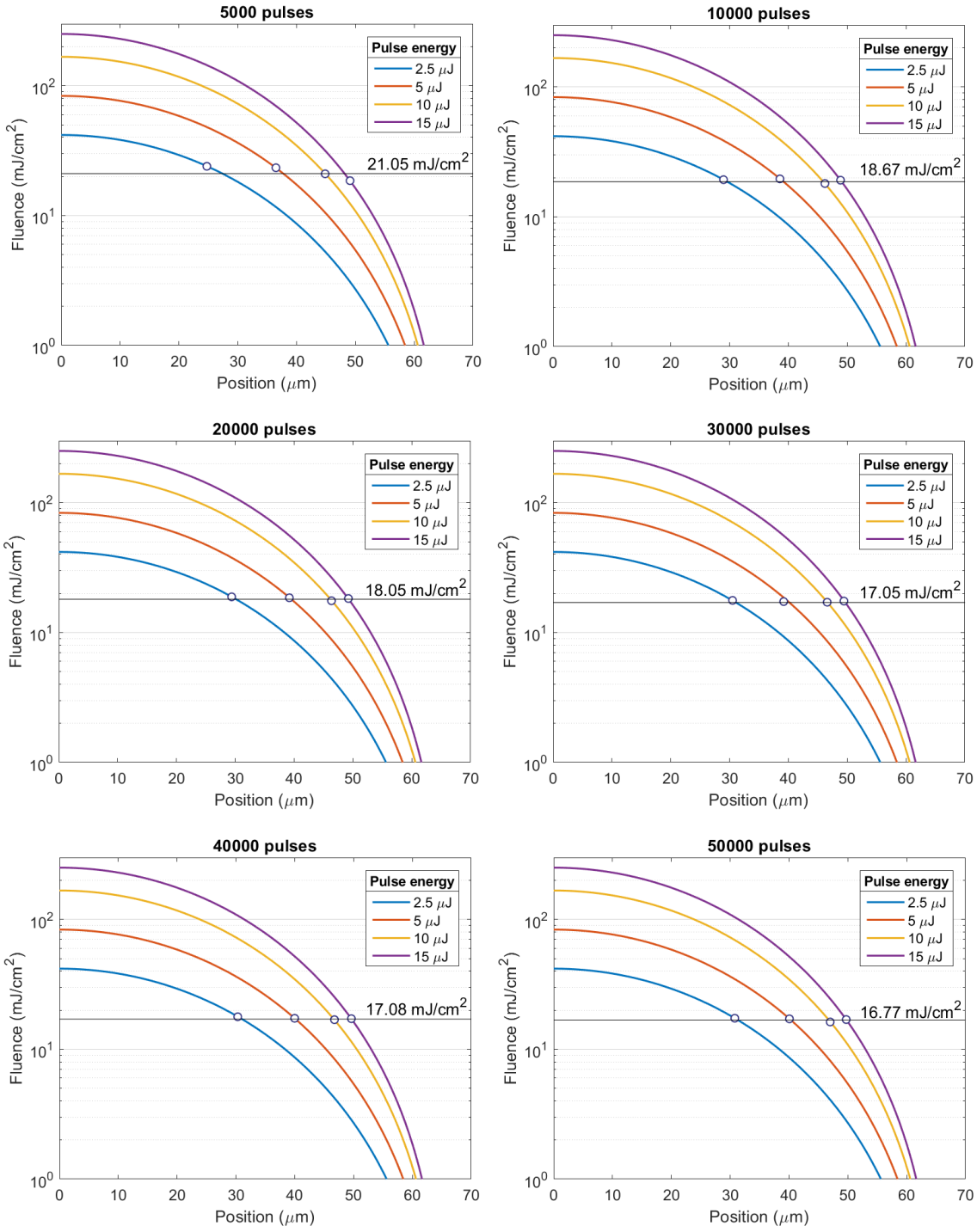

Figure 23. For each incident pulse energy, the measured crater radius in bismuth is represented in the fluence profile as a point on the corresponding curve; the horizontal axis represents the measured radius, while the vertical axis represents the corresponding fluence at a given radius. The average value of the ablation threshold is represented by the horizontal lines.

We determined the ablation threshold dependence on the number of pulses for our titanium and bismuth films using two repetition rates; 1 kHz and 5 kHz. Markers in figure 24 show our experimental results; as expected, the ablation threshold decreases as the number of pulses increases. Table 4 shows the values of the single-pulse ablation threshold $\Phi_{th}(1)$ and the incubation factor ξ that result from fitting the power-law equation 67 to our experimental data. Using these values we plotted the ablation curves in figure 24 in logarithmic scale to visualize them as linear equations $(\log(\Phi(N)) = (\xi - 1)\log(N) + log(\Phi(1)))$. It is worth mentioning that the ablation threshold values depend on both the material's specific features and the irradiation parameters. Hence, it is necessary to carry out this characterization for each sample.

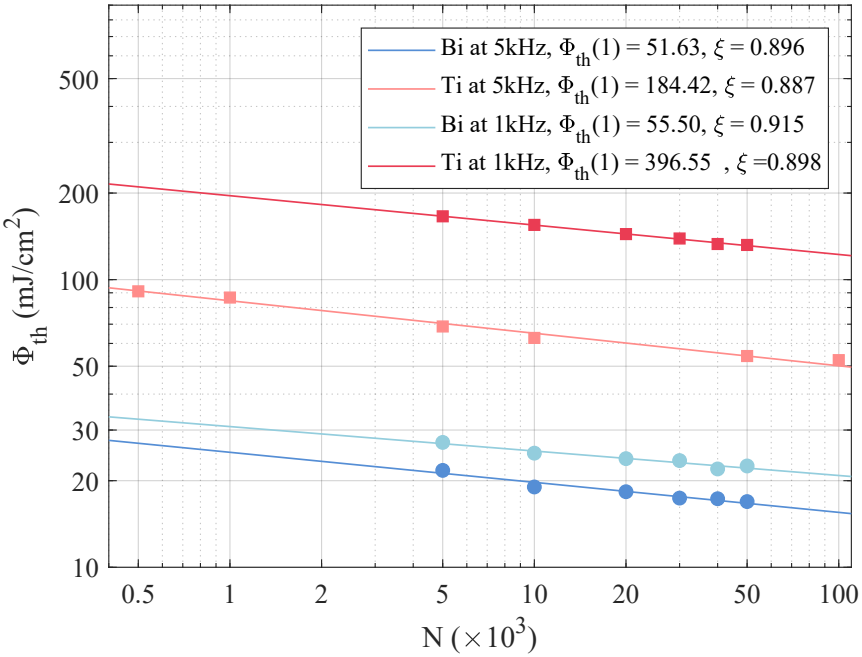

Figure 24. Ablation threshold fluence versus the number of applied pulses together with the best fit values of incubation coefficient and single-pulse ablation threshold.

Table 4. Parameters for the ablation threshold fluence obtained at 1 and 5 kHz.

Material	f_{rep}(kHz)	$\Phi_{th}(1)$(mJ/cm^2)	ξ
Bi	5	51.63	0.896
	1	55.5	0.915
Ti	5	184.42	0.887
	1	396.55	0.898

In both metals, the ablation line corresponding to 5 kHz extends below the one corresponding to 1 kHz. It suggests that the single-pulse ablation threshold $\Phi_{th}(1)$ might depend on the repetition

rate; nevertheless, it has no physical sense. In an attempt to explain this phenomenon, we propose to modify the equation67 by splitting $\Phi_{th}(1)$ into two components; the actual single-pulse ablation threshold $\Phi_{th}(1)$ plus an amount $\Delta(f_{rep})$. We can attribute this latter to heat accumulation when the thermal dissipation time exceeds the period between consecutive pulses. Therefore, the incubation law 67 can be reformulated as $\Phi_{th}(N) = [\Phi(1) + \Delta(f_{rep})]N^{(\xi-1)}$ so that when increasing the repetition rate, the ablation curve will experience a parallel displacement downwards.

It is worth mentioning that in spite of the laser repetition frequency, the ablation threshold of bismuth remains bellow that of the titanium. We can explain this fact by taking into account the fusion temperatures of both materials (see table 1), since the bismuth fusion temperature is quite smaller than that of the titanium, the ablation threshold of bismuth can be also attained at lower values of fluence. Whereas, the high fusion temperature of titanium, requires more energy to be attained.

4.4 The relation between laser fluence a number of pulses in the LIPSS formation process

Several micrographs in figure 21 reveal a ring made of LIPSS on the periphery of the ablated craters, which confirms that LIPSS formation process occurs at fluences close to the damage threshold (Bonse *et al.*, 2017). This characteristic led us to infer that the fluence required to produce LIPSS (Φ_{LIPSS}) is just below that of the ablation threshold (Φ_{th}); furthermore, the whole process could consist of an incubation process. Hence, it is reasonable to assume that the fluence needed to generate LIPSS, Φ_{LIPSS}, can be described by the same equation of the ablation threshold fluence (equation 67) multiplied by a positive constant k whose value must be lower than one to ensure that $\Phi_{LIPSS} < \Phi_{th}$. Therefore, the LIPSS fluence equation is

$$\Phi_{LIPSS}(N) = k \cdot \Phi(1)N^{(\xi-1)}. \tag{68}$$

To assess the validity of this hypothesis, we aimed to produced LIPSS using the equation 68. In the previous section we determined the value of $\Phi(1)$ and ξ for bismuth and titanium (see table 4). We used those parameters to plot the ablation curves (solid black lines in figures 25-a and -b). Additionally, we plotted a set of curves corresponding to different values of k (dashed lines). From those curves, we chose the points represented by the circle markers to irradiate the samples.

Afterward, we inspected the irradiated spots using optical microscopy (OM). In both materials we found the formation of LSFL perpendicular to the laser polarization; figures 51 and 52 in appendix show the resulting micrographs along with the corresponding irradiation parameters. Although all irradiated spots show surface modification only those with $N > 2$ and $k > 0.3$, clearly exhibit formation of ripples. Such spots are represented in figure 25 by the filled-markers, while the rest of spots are represented by the unfilled-markers.

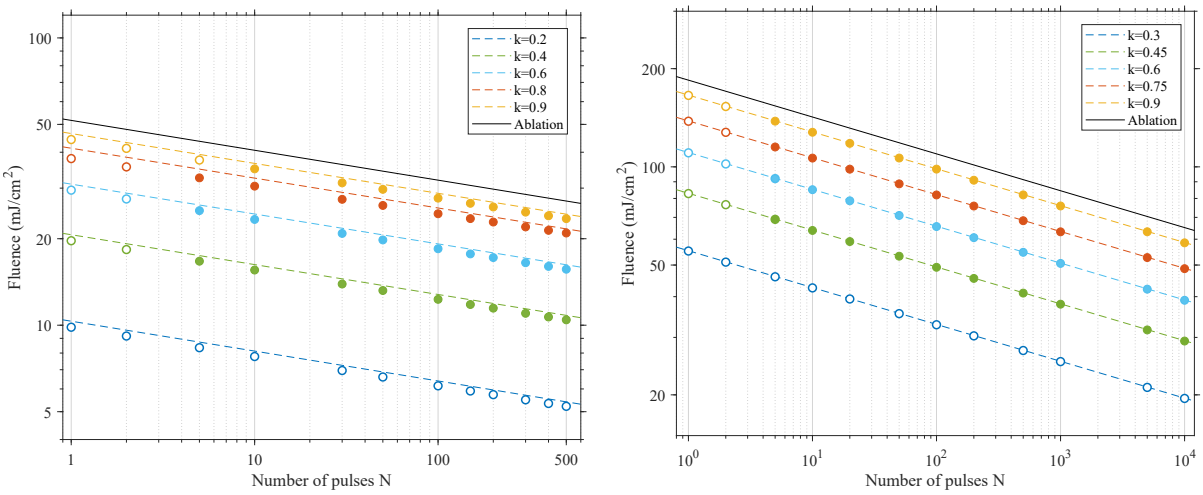

(a) Bismuth fluence curves

(b) Titanium fluence curves

Figure 25. Laser fluence with respect to the number of pulses using a logarithmic scale. The circle markers correspond to the fluence and number of pulses the Bi film was irradiated with. The unfilled-markers represent the irradiation spots where there is no presence of LIPSS. While the filled-markers represent the irradiation spots where it was demonstrated formation of LIPSS.

4.5 LIPSS characterization

We applied three different microscopic techniques to visualize the LIPSS formed on our samples: Optical microscopy (OM, model Olympus BX41), scanning electron microscopy (SEM, model Hitachi SU3500), and atomic force microscopy (AFM, model NanoSurf Flex-Axiom with controller C3000). LIPSS characteristics like periodicity (Λ) and orientation (θ) can be easily determined by means of a basic image processing technique based on the two-dimensional Fourier transform of the OM and SEM micrographs.

4.5.1 Image analysis via two-dimensional Fourier transform

Any micrograph consists of a two-dimensional array divided into $M \times N$ picture elements (pixels) that can be described by a function $f(x, y)$ representing the brightness at the point (x, y). Fourier analysis is based on the premise that any image can be equivalently represented in the spatial domain as in the reciprocal space referred to as frequency domain or k-space (Rzeszotarski and Gilmore, 1983). While x and y are the coordinates in space, k_x and k_y are the coordinates in the k-space. The Fourier Transform approximates the image $f(x, y)$ through sine and cosine wave-functions with different wavenumbers by the equation

$$F(k_x, k_y) = \frac{1}{MN} \sum_{m=0}^{M-1} \sum_{n=0}^{N-1} f(x_n, y_m) e^{-i\left(\frac{k_x}{M} x_n + \frac{k_y}{N} y_m\right)}. \tag{69}$$

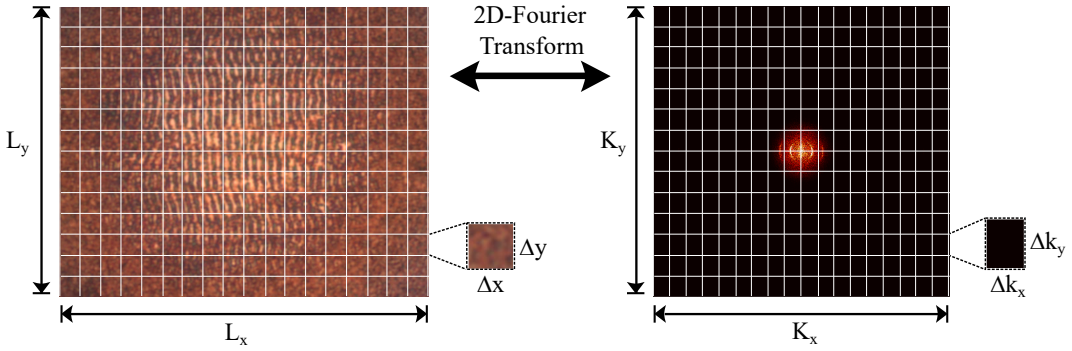

Figure 26. Illustration of the 2D-Fourier transform from an optical micrograph of a bismuth surface with LIPSS. Irradiation parameters: $\lambda = 1030$ nm, $\theta = 0$, $E_p = 2.5$ μJ, $N = 100$ pulses, $f_{rep} = 5$ kHz.

As shown in the following diagrams, the image size and pixel width along each axis determine the number of samples in the k-space. The image size is inversely proportional to the spacing between samples ($\Delta k = 1/L$). Additionally, there is an inverse relationship between the pixel width and the range between the highest positive and negative spatial frequencies in the k-space ($\Delta s = 1/k$).

The Fourier transform of an image made of periodic parallel lines features information about the pattern orientation and periodicity. To illustrate it, let us consider the example shown in figure 27; two perfect periodic patterns of lines $f(x, y)$ and the magnitude of their Fourier transforms $|F(k_x, k_y)|$.

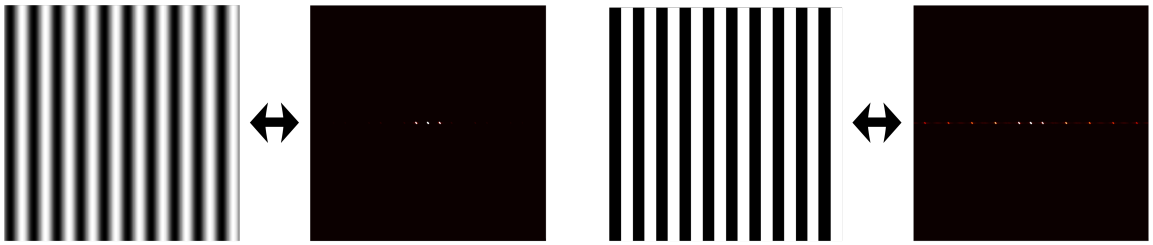

(a) (b)

Figure 27. Comparison of the Fourier transformations of periodic brightness patterns of a perfect sinusoidal profile (a) and a square-wave profile (b).

The periodic pattern made of a perfectly sinusoidal variation in brightness (figure 27-(a)) can be described as well in the positive as in the negative directions. Its representation in the k-space consists of two symmetrical points of equal intensity and magnitude but opposite directions from the origin. Their wavenumber $k = \sqrt{k_x^2 + k_y^2}$ is associated to the pattern periodicity Λ by the inverse relation $k = 2\pi/\Lambda$. Moreover, the orientation of the secant line that passes through those points, $\theta = \tan^{-1}(k_y/k_x)$, is perpendicular to the pattern wavefront. On the other hand, the step-shape pattern in figure 27-(b) requires several frequency components to reproduce the square-wave profile. Consequently, its Fourier transform is composed of multiple bright points aligned perpendicular to the pattern wavefront. In both cases, the bright spot at the center of the Fourier transform corresponds to the mean luminance of the whole image; it comes from substituting the zero frequency ($k_x = k_y = 0$) into equation 70,

$$\frac{1}{MN}\sum_{m=0}^{M-1}\sum_{n=0}^{N-1} f(x_n, y_m) e^{-i\left(\frac{k_x}{M}x_n + \frac{k_y}{N}y_m\right)}\Big|_{k_x=0, k_y=0} = \frac{1}{MN}\sum_{m=0}^{M-1}\sum_{n=0}^{N-1} f(x_n, y_m). \tag{70}$$

Nonetheless, LIPSS consists of a quasi-periodic array of lines, like the ones shown in figure 28-(a), whose spatial characteristics strongly depend on the irradiation parameters of the laser used to produce them, particularly the wavelength and polarization. For this reason, we normalize the scales of the image and its Fourier transform by the laser wavelength (λ) and its wavevector ($k_0 = 2\pi/\lambda$) so that we can directly correlate the LIPSS features in the frequency and space domains to the laser wavelength. Accordingly, any pair of symmetrical points on or within the unitary circle in the normalized k-space corresponds to LIPSS whose periodicity is larger than or equal to the laser wavelength. Likewise, all points outside the unitary disk correspond to patterns with periods smaller than the laser wavelength. In accordance with LIPSS classification (section 1.1), any pair of symmetrical points within the region between the unitary circle and the circle of radius two can be

considered a prospect of LSFL, whereas any pair of symmetrical points outside the circle of radius two, is a candidate of HSFL.

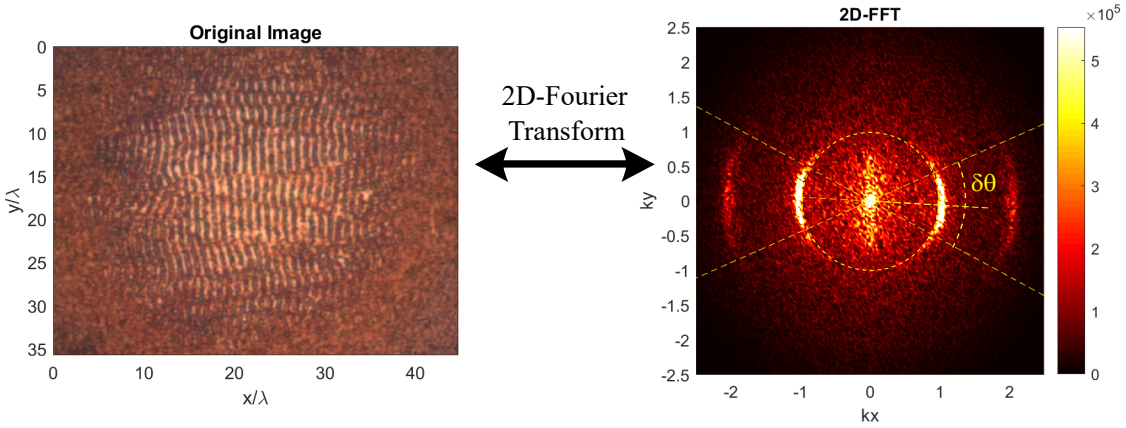

Figure 28. Example of 2D-FT from a SEM image of LIPSS on bismuth 800H irradiated with $\lambda = 1030$ nm, normal incidence and $E_p = 2.5$ μJ, 100 pulses, $f_{rep} = 5$ kHz

As shown in figure 28, the pair of points with the maximum intensity in the Fourier transform of a LIPSS micrograph usually corresponds to the average wavenumber of the dominant pattern. Nevertheless, many other wavenumbers may emerge during the transformation due to the noise present in the image. LIPSS are not composed of perfectly parallel lines but rather quasi-periodic lines with a range of periods and orientations. Hence, instead of having two symmetrical points, we will observe a kind of arcs or crescents around maximum intensity points. The angular opening of those crescents is comparable to the so-called dispersion of the LIPSS orientation angle (DLOA), which is used as a measure of the LIPSS regularity (Gnilitskyi *et al.*, 2017). Figure 29-(a) displays a histogram of the wavenumber distribution corresponding to the points in the crescent around the maximum.

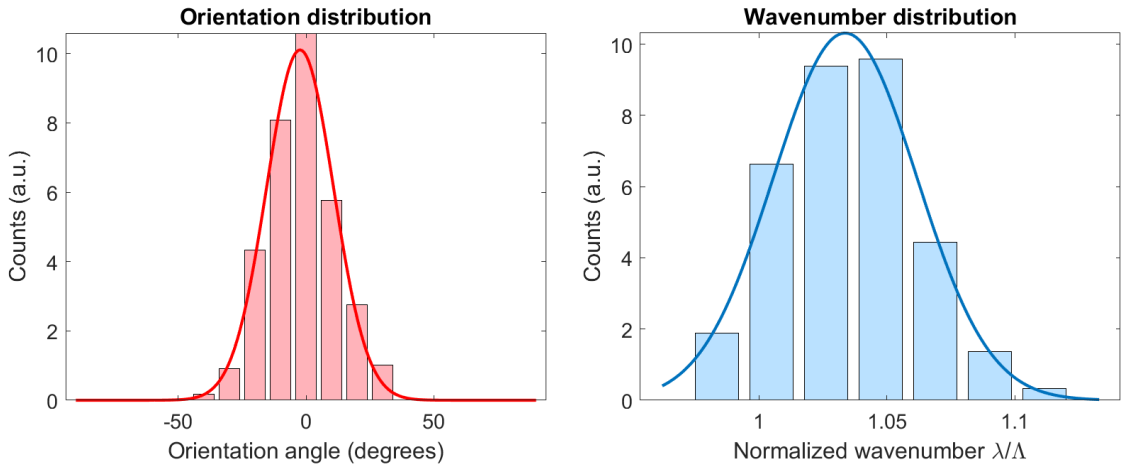

(a) (b)

Figure 29. a) Orientations distribution, interval size 10°. b) Wavenumbers distribution, interval size $\Delta k = 0.02$.

The histogram data were fitted with the Gaussian function $G(k) = A\exp[-(k-\bar{k})/\sigma_k]^2$ (blue line) to obtain the distribution center $\bar{k}$ and the half width at $1/e$, σ_k, of the maximum height; the first one is associated with the LIPSS mean periodicity by the equation $\Lambda = \lambda/\bar{k}$ while the second one measures the spread of the wavenumber values. Similarly, Fig.29-b displays the histogram of the orientation angle distribution for the points in the neighborhood around the maximum. These data were fitted with the Gaussian function $G(\theta) = A\exp[-(\theta-\bar{\theta})/\sigma_\theta]^2$ (blue line) to obtain the orientation angle $\bar{\theta}$ and the dispersion of the LIPSS orientation angle $\delta\theta$, which is equivalent to the half width at $1/e^2$ of the maximum height, $\delta\theta = \sqrt{2}\sigma_\theta$.

4.6 Low spatial frequency LIPSS in bismuth and titanium

We used the Fourier technique described in the previous section to analyze the dependence of LIPSS periodicity and DLOA on the number of pulses N and laser fluence Φ. To achieve reliable data, we require to perform a Fourier transform of high-frequency resolution. To this aim, we must either increase the image size or reduce the pixel width to perform a finer sampling. Therefore, we decided to use images obtained by scanning electron microscopy (SEM), which may feature resolutions even better than 1 nanometer.

From the irradiation matrices performed in section 4.4, we acquired SEM-micrographs of the spots corresponding to N = 1, 10, 50, 200, 400, and 500 pulses in bismuth (see figure 53) and N = 2, 5, 20, 100, 500, 1000, 5000, and 10000 pulses in titanium (see figure 54). Afterward, we conducted

the Fourier analysis on the SEM-micrographs. Graphs in figure 30 show the LIPSS periodicity as a function of N. Let us recall that we produced those LIPSS using the equation 68, which reduces the laser fluence in order to prevent the sample from getting ablated when increasing N. According to this equation, the fluence necessary to produce LIPSS (Φ_{th}) must be lower than that of the ablation threshold, $\Phi_{LIPSS} = k\Phi_{th}$. We have linked the points in figure 30 corresponding to the same value of k. We notice that bismuth LIPSS made with few pulses have periods slightly smaller than the laser wavelength (1030 nm); these decrease when increasing the number of pulses. After 500 pulses, LIPSS periodicity has been reduced by 15 nm approximately. Conversely, LIPSS on titanium for few pulses exhibit periods far below the laser wavelength and decrease up to 100 nm after 1000 pulses.

Regarding the LIPSS regularity, the DLOA graphs in figure 31 show a tendency that does not look like depending on k. In other words, it does not depend on how close to the ablation threshold we are. In the case of bismuth, we cannot identify a global minimum but, in the case of titanium, we notice a minimum around $N = 100$ for all values of k, which means that the most regular LIPSS can be obtained for this number of pulses.

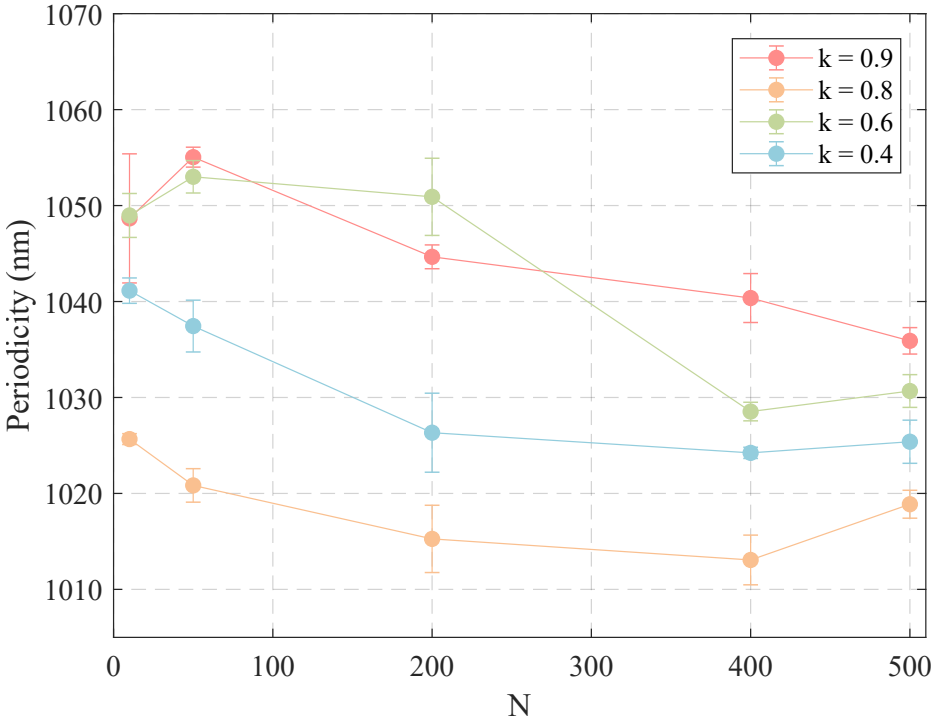

(a)

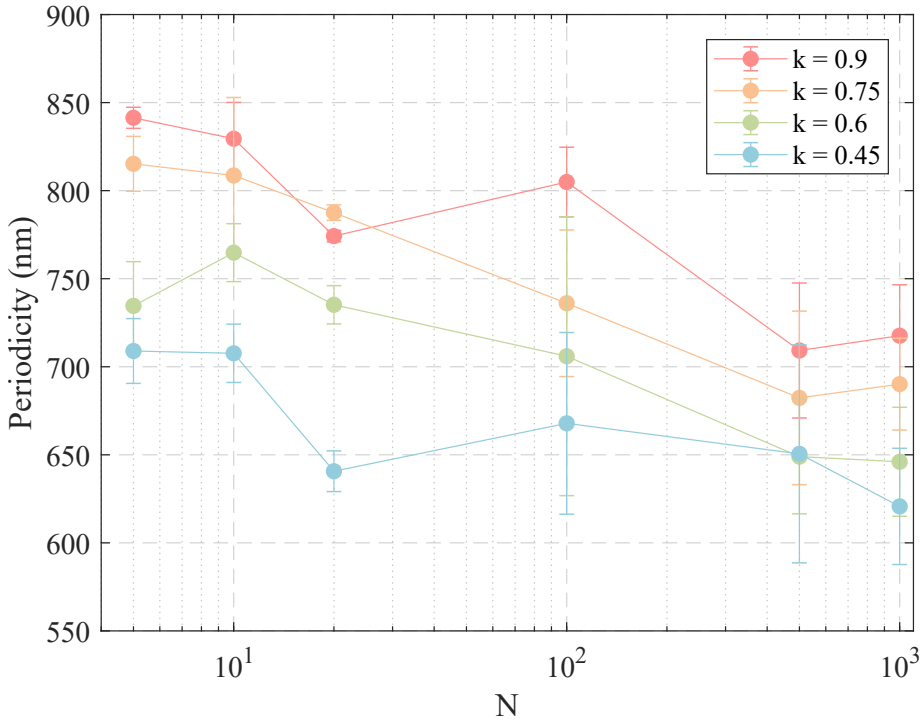

(b)

Figure 30. LIPSS periodicity generated on bismuth (a) and titanium (b) as a function of the number of pulses N, the fluence varies following the power law of Eq.68 using the values for $\Phi_{th}(1)$ and ξ from Tab.4 for different values of k. The data were obtained from a Fourier analysis on the micrographs of figures 53 and 54.

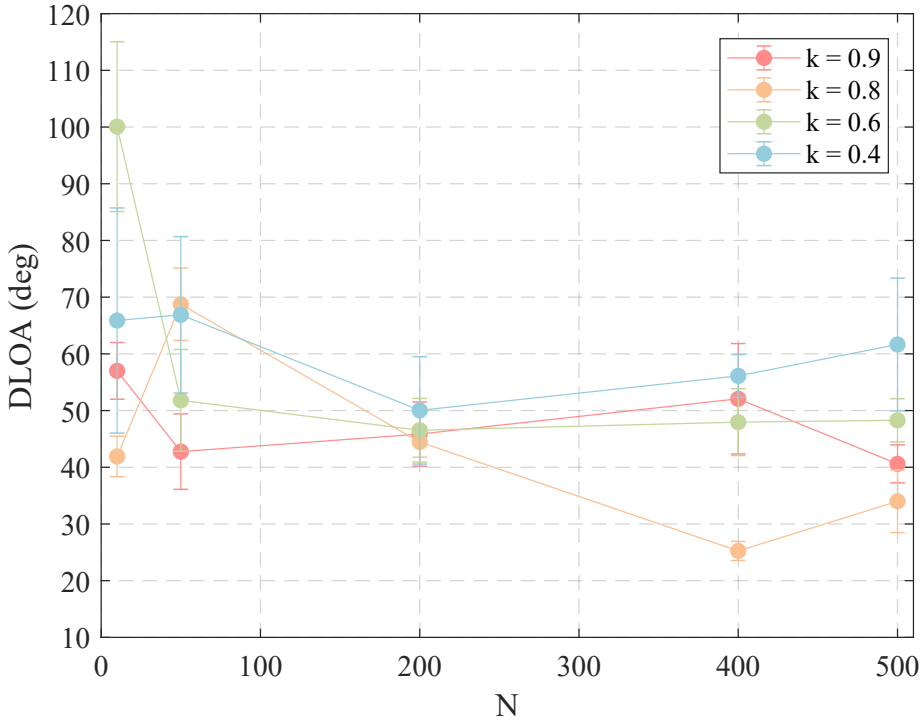

(a)

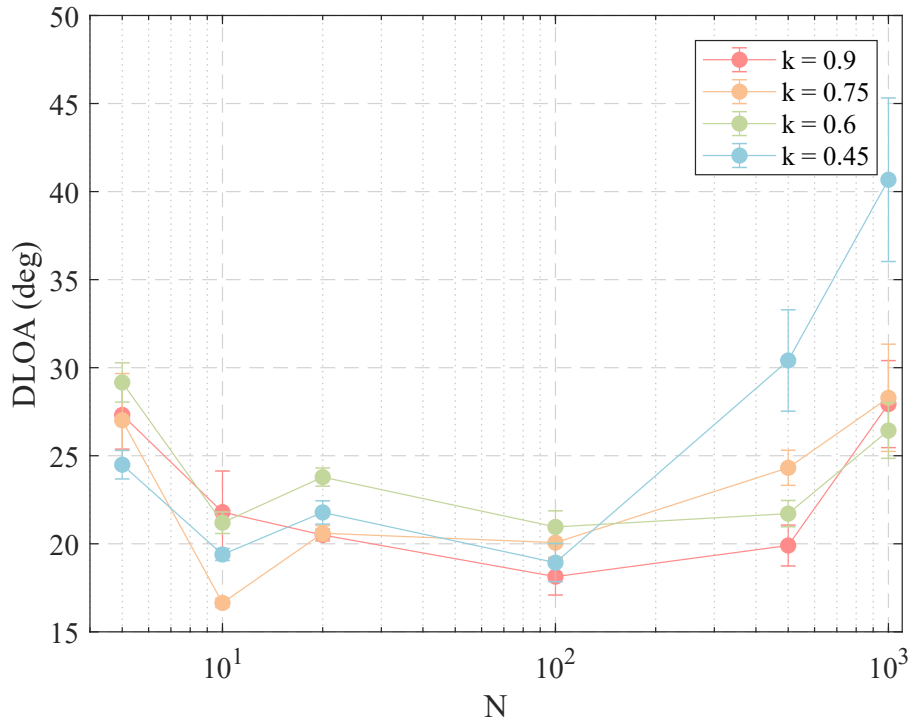

(b)

Figure 31. DLOA of the LIPSS generated on bismuth (a) and titanium (b) as a function of the number of pulses N. The fluence varies with the number of pulses, according to the power law of Eq.68 using the values for $\Phi_{th}(1)$ and ξ from Tab.4, for different values of k. The data were obtained from a Fourier analysis of the micrographs in figures 53 and 54.

4.6.1 The role of the grating depth in the SPP coupling

As mentioned in section 3.1.1, laser light can be coupled from free space into SPPs only by phase-matching; usually via attenuated total reflection or grating-coupling. However, SPPs can also be excited through scattering produced by wavelength-size defects on the surface (Keilmann and Bai, 1982; Derrien *et al.*, 2013; Tsibidis and Stratakis, 2017). Afterward, the SPPs may interfere with the incident light giving rise to the first ripples' formation. Figure 30 shows our results for the LIPSS periodicity Λ as a function of the number of applied pulses N in titanium and bismuth. In both materials, we notice that after the first pulses, the surface roughness increases homogeneously (Fuentes-Edfuf *et al.*, 2019). Nevertheless, once the initial ripples have formed, their period Λ decreases as N increases; the grooves-depth may play an important role in this effect since it also changes with the number of pulses, and its value modifies the shape of the SPP dispersion diagram.

As LIPSS are forming, their presence modifies the way the SPPs couple and propagate (Raether, 2014; Tsibidis and Stratakis, 2017); consequently, it is necessary to change the physical picture of LIPSS formation from a pure interference mechanism to a grating-coupling feedback process (Huang *et al.*, 2009a; Fuentes-Edfuf *et al.*, 2019). As mentioned in section 3.1.3, the SPP grating-coupling requires fulfilling the phase-matching condition of equation 48. Figure 32 shows some LIPSS profiles in titanium produced with a few pulses. As expected, they become more profound with the number of pulses. When the first LIPSS are formed, the electromagnetic field gets enhanced within the grooves (Huang *et al.*, 2009b), which leads to greater energy absorption in those areas, and subsequently, the deepening of the grooves. This feedback process is responsible that LIPSS become deeper and deeper with the number of applied pulses. Several authors (Huang *et al.*, 2009a; Raether, 2014) have pointed out that the SPP dispersion diagram of a grating with deep grooves is severely modified and tends to flatten; consequently, the resonant grating-wavelength Λ shifts to shorter values to ensure the best SPP-coupling. Therefore, when increasing the number of pulses, we expect that the LIPSS periodicity decreases due to the grooves' deepening.

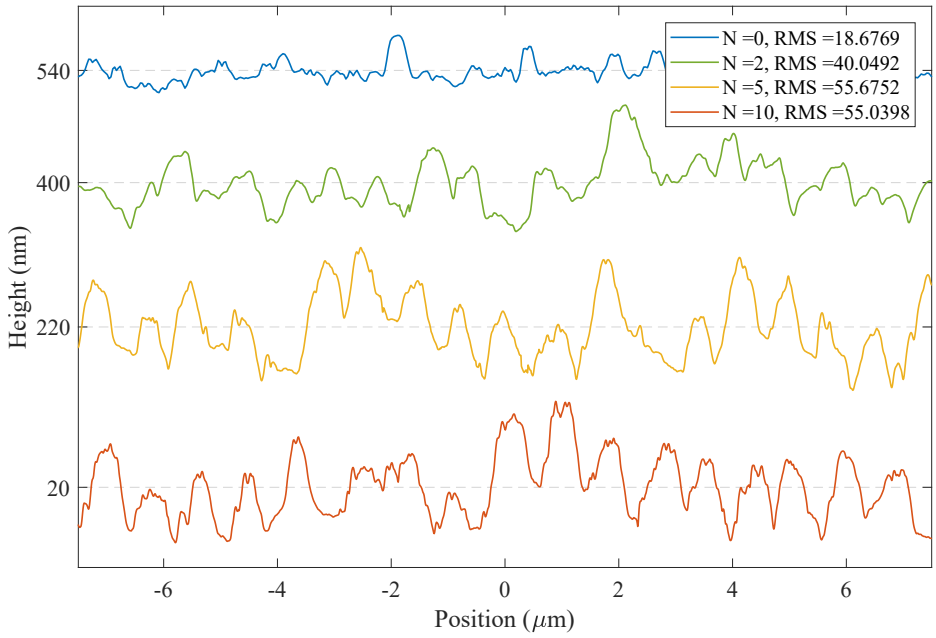

Figure 32. Surface cross-sections acquired by AFM of titanium spots irradiated with 0, 2, 5, and 10 pulses and fluence corresponding to 90% of the ablation ($k = 0.9$).

We used the commercial software COMSOL Multiphysics to simulate a TM-polarized plane wave of 1030 nm striking onto an infinite grating at normal incidence. Figure 33(a) illustrates the simulation domain. Since the grating is a periodic array, we only simulated a unitary cell with periodic walls (Sukhotskiy *et al.*, 2018) so that the cell width corresponds to the grating period Λ. The groove-depth value h was varied from 10 nm to 200 nm in steps of 10 nm. For each groove-depth, we computed the reflectivity varying the grating-period.

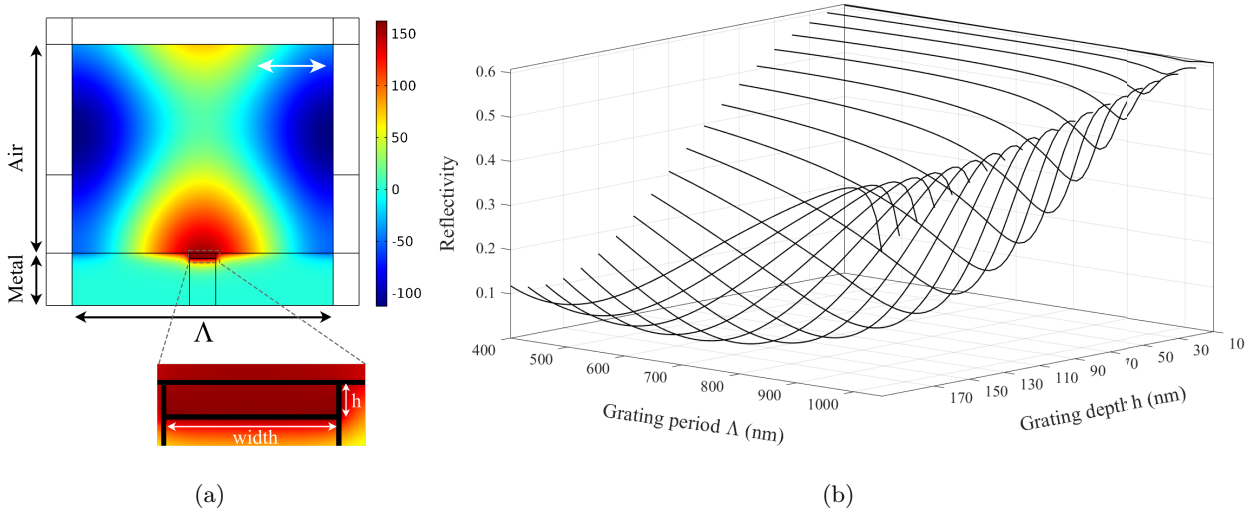

(a) (b)

Figure 33. Simulation of SPP grating-coupling. (a) Grating unit-cell geometry, the light source consists of a p-polarized plane wave at normal incidence. varying the grating depth. (b) Reflectivity plot as a function of the grating period for different values of h, each curve's minimum is attributed to the possible SPP-resonance.

Figure 33(b) shows the reflectivity as a function of the grating-period for each groove-depth in titanium. The minimum in each of those curves corresponds to the SPP-resonance wavelength associated with that value of depth. Figure 34 displays the graphs of the grating period at which the SPP-resonance occurs as a function of the depth of the grooves in titanium (a) and bismuth (b).

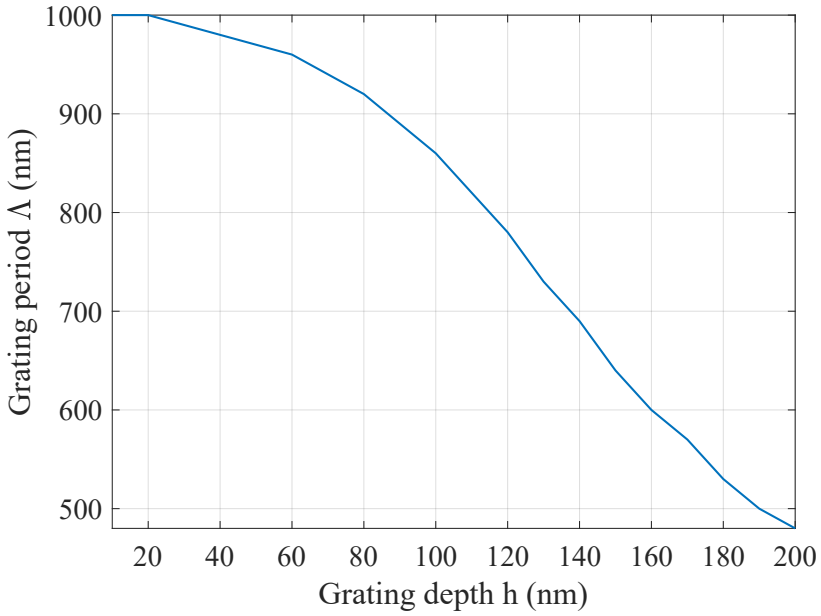

(a)

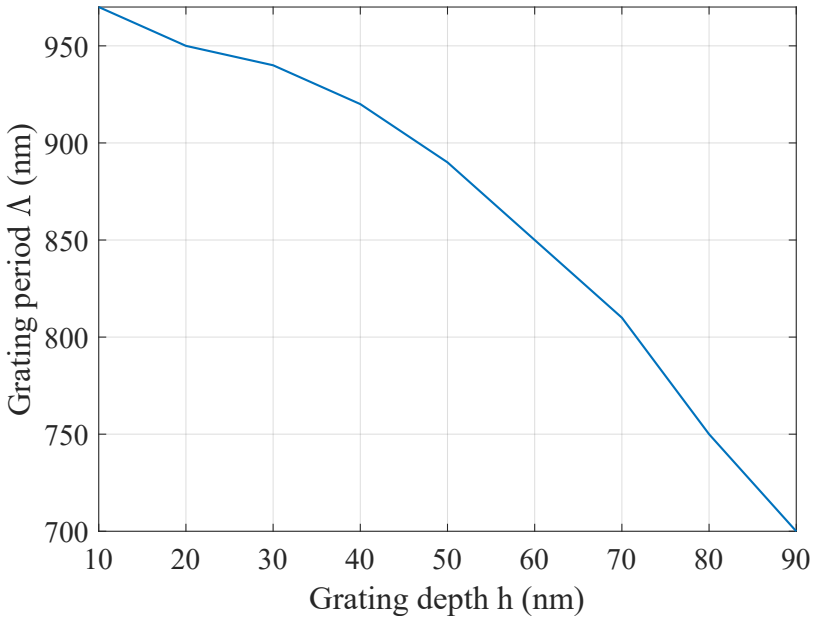

(b)

Figure 34. Dependence of the grating period at which the SPP-resonance occurs on the grating depth h. (a) Simulation for titanium ($\varepsilon = -5.618 + 23.304i$). (b) Simulation for bismuth ($\varepsilon = -1.245 + 8.448i$).

We notice from figure 34 that the grating period's dependence on the depth of the grooves is similar to the trend of the LIPSS periodicity as a function of N in figure 30. Moreover, as seen in figure 32, there is a direct relationship between the grooves' depth and the number of pulses. Therefore, this mechanism may explain our experimental observations about the shift of LIPSS periodicity to lower values as the number of pulses increases. Nonetheless, we should remark that this feedback process is limited by the decrease of the direct SPP-coupling efficacy (see subsection 3.1.3).

4.7 LIPSS produced using oblique incidence

In accordance with both the efficacy factor theory and the SPP model, the incident light wave-vector parallel to the plane, $\mathbf{k}_o \sin(\theta)$, and the wave-vector of the scattered waves, $|\mathbf{k}_s|$, may produce an interference pattern of wave-vector

$$|\mathbf{g}_{\pm}| = |\mathbf{k}_s| \pm |\mathbf{k}_o \sin(\theta)|. \tag{71}$$

The $\pm$ sign represents the possibility of having counter-propagating SPP in the forward or backward directions. The interference between incident and scattered light leads to periodic modulation of energy that is imprinted into the medium as a LIPSS pattern. According to equation 71, when the incidence angle is other than zero, the fringe pattern might exhibit two different periods, $\Lambda_{\pm} = 2\pi(|\mathbf{k}_s| \pm |\mathbf{k}_o \sin(\theta)|)^{-1}$, simultaneously.

To assess the effectiveness of efficacy factor theory and SPP-model in predicting LIPSS periodicity, we produced bismuth LIPSS for oblique incidence, using the optical setup shown in figure 18. We varied the incidence angle θ from 0° (normal incidence) to 12° by tilting the sample mount. The light polarization was adjusted to be transverse-magnetic, which, as mentioned in section 3.1.1, is a necessary condition for exciting SPPs. During the irradiations, we kept the energy per pulse constant while increasing the incidence angle and, consequently, the beam spot effective area. To compensate for the fluence fall, we augmented the number of pulses, as described in section 4.4. Figure 35 shows the Fourier transform of the LIPSS OM-micrographs corresponding to three angles of incidence (0°, 6°, and 10°).

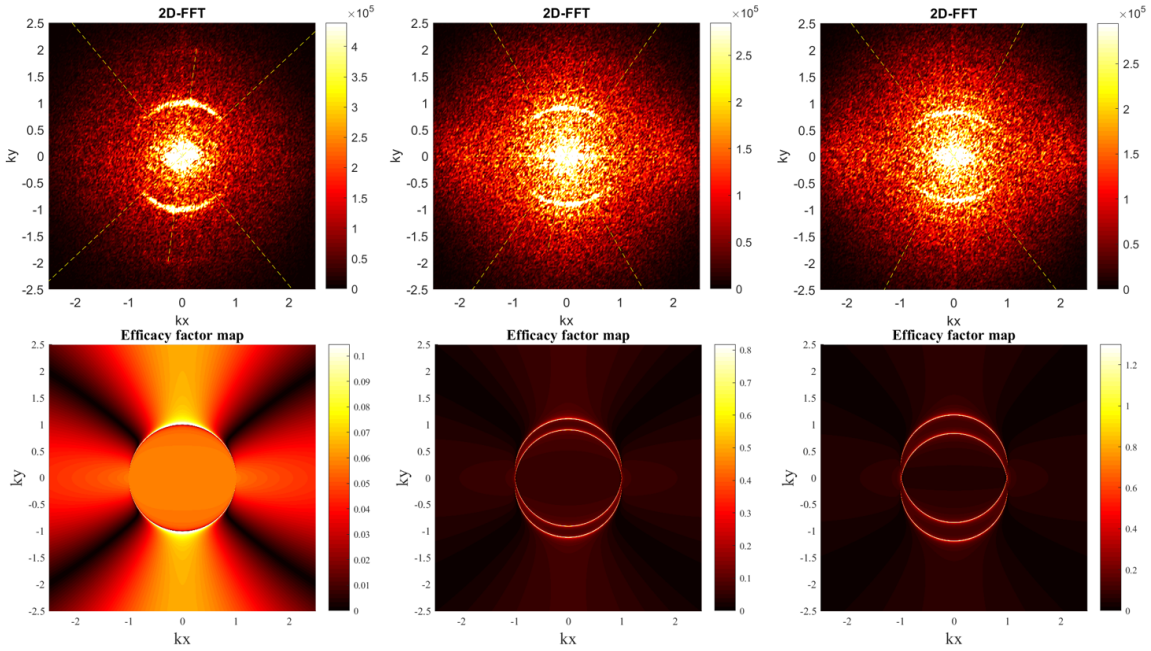

Figure 35. The upper panels present the Fourier transform obtained from the OM-micrographs of the LIPSS produced at $\theta = 0°$ (a), $6°$ (b), and $10°$ (c). The bottom panels show the corresponding Efficacy factor maps numerically calculated with the the dielectric constant, $\varepsilon_{Bi} = -69.9197 + 5.8502i$ at $\lambda = 1030$ nm, provided by (Werner 2009).

Figure 36 shows the angular dependence of LIPSS periodicity and compares the theoretical values of periodicity using the Efficacy factor theory and the SPP interference model with those of our experimental results. The values of Λ_+ and Λ_- were obtained via the filtering technique based on Fourier analysis of the LIPSS micrographs.

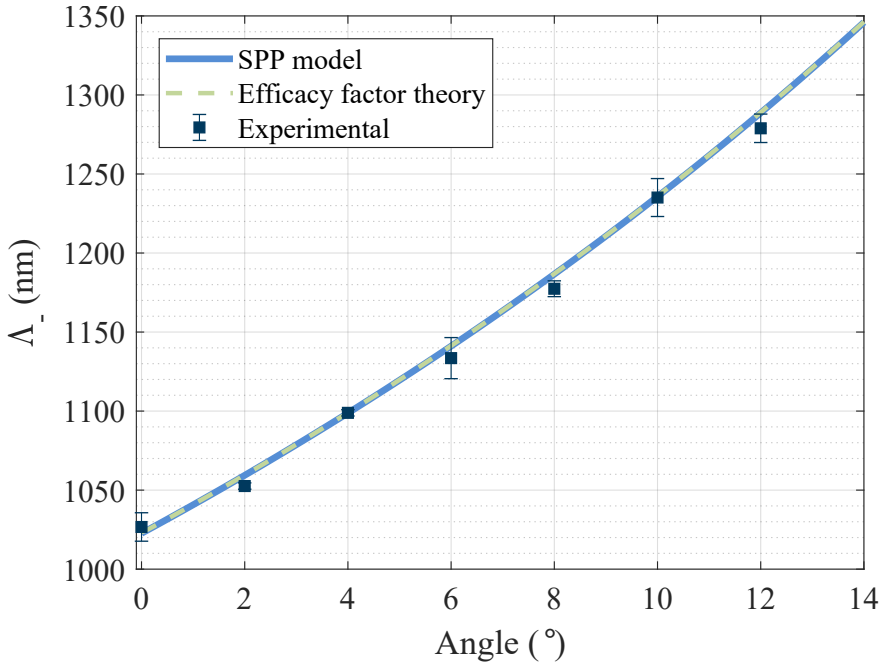

(a)

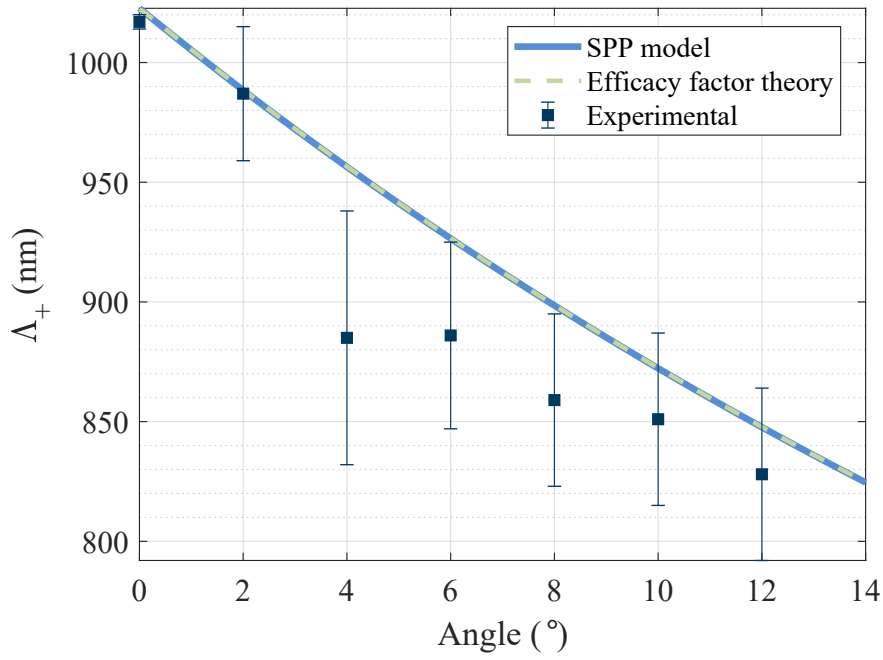

(b)

Figure 36. Comparison between experimental and theoretical periods for oblique incidence. Theoretical curves were calculated with the the dielectric constant, $\varepsilon_{Bi} = -69.9197 + 5.8502i$ at $\lambda = 1030$ nm, provided by (Werner 2009).

Good agreement between experimental and theoretical results in figure 36-(a) demonstrates the efficacy of both theoretical models on predicting LIPSS periodicity Λ_-. However, they fail to predict the other periodicity Λ_+ although they have success to reproduce the general tendency of the LIPSS

period Λ_+. The discrepancy can be attributed to the high noise in the Fourier spectra due to the film roughness. In section 4.4 we demonstrated for normal incidence, the LIPSS periodicity depends on both, the number of pulses and the applied fluence. However the the difference in period due to the range of N and Φ is small compared to the difference due to change the angle of incidence. Hence, the effect of the number of pulses is not noticeable in graphs of figure 36.

Chapter 5. Laser-Induced Oxide Layer in the Formation of LIPSS

After irradiating a substrate some compounds may be formed on the surface, particularly oxides. Raman spectroscopy allow us to study the chemical composition of the Ti and Bi films differentiating the multiple phases (crystallographic forms or polymorphs) that a single compound may exhibit. In this section we study the different compounds that result from irradiating the surface as well as the sub-wavelength structures that they can form.

5.1 HSFL on bismuth

We notice from the bismuth micrographs in figure 51 that many of the spots irradiated with several hundred of pulses show the formation of ripple structures other than LSFL, which emerged upon increasingly irradiating the film surface. Let us consider, for instance, the SEM micrographs in figure 37 corresponding to $k = 0.8$ 10 and 500 pulses; their respective Fourier transform is displayed in the right-top corner inset. In both cases, the Fourier spectrum shows the typical crescents around the unitary circle, associated with LSFL perpendicular to the laser polarization. However, the Fourier spectrum of the LIPSS made with 500 pulses additionally exhibits two clusters of symmetrical points located outside the circle of radius two and perpendicular to the LSFL crescents. Therefore, those clusters can be associated with periodic structures falling into the classification of HSFL type II (see figure 2) whose orientation is parallel to the laser polarization.

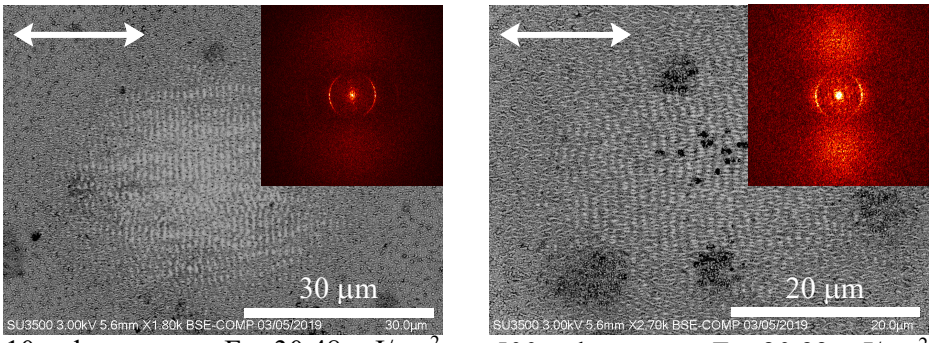

(a) (b)

Figure 37. Comparison of LIPSS formed on bismuth after 10 (left) and 500 (right) pulses. The white horizontal arrows indicate the polarization direction of the incident wave. Right corner insets, 2D-Fast Fourier transform of each SEM micrograph.

As shown in the example of figure 38, a two-dimensional image filtering in the frequency domain allows us to analyze the LSFL separately from the HSFL. In this example the approximate periodicity of LSFL is 1020 nm whereas for the HSFL is 430 nm. As mentioned in section 1.1, HSFL have been observed predominantly in dielectric materials for pulse duration in the femtosecond regime and very close to the damage threshold of the irradiated material. Furthermore, some authors have suggested that oxidation on metal surfaces during the resolidification of a shallow laser-induced melt layer is involved in the formation of HSFL of type II (Bonse *et al.*, 2017). Consequently, the HSFL found in the bismuth film might be composed of some kind of bismuth oxide, grown on top of the previously formed LSFL.

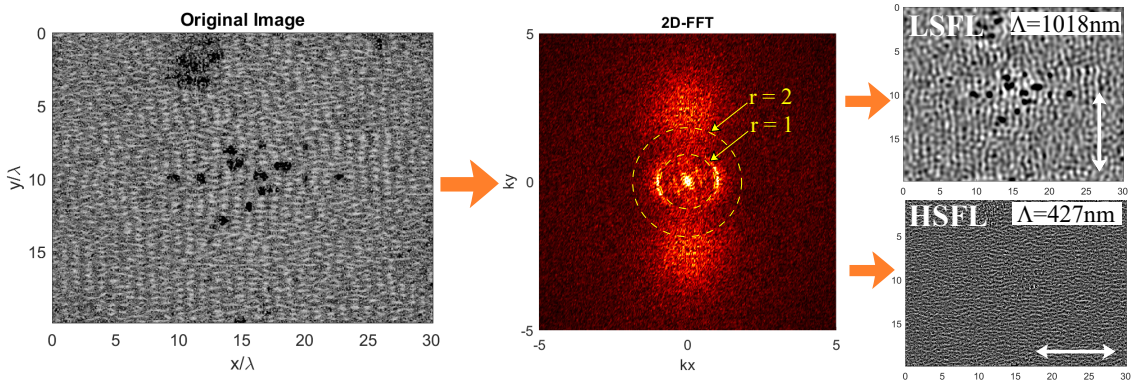

Figure 38. Analysis of LSFL and HSFL on the same bismuth sample through 2D-FFT.

To verify the presence of a possible laser-induced bismuth oxide on the film surface, we studied the chemical composition of the irradiated spots corresponding to $k = 0.8$ in figure 51 through micro-Raman spectroscopy. The resulting Raman spectra are shown in figure 39-(a).

All the Raman measurements exhibit two bands at 74 and 97 cm^{-1}, which are associated with the lattice vibrations and the vibrational modes of the bismuth atoms respectively (Zepeda *et al.*, 2012). In addition, we notice other Raman bands that emerge as the number of pulses is increased, particularly in the 250-350 cm^{-1} range. This progressive change in the Raman spectrum is an indicator that a chemical reaction is occurring, probably a laser-induced oxidation. From measuring the position of the emerging peaks, we are able to determine the specific compounds formed after irradiating the surface. Based on previously reported studies on laser-induced oxidation of bismuth films (Zepeda *et al.*, 2012; Steele and Lewis, 2014; Diaz-Guerra *et al.*, 2017), we focused our attention in identifying bismuth trioxide, Bi_2O_3, which possesses four main polymorph phases: (Diaz-Guerra *et al.*, 2017) α, β, γ, and δ. [1]

[1] Other two metastable phases, ω and ε, have been obtained under special conditions (Gualtieri *et al.*, 1997; Cornei

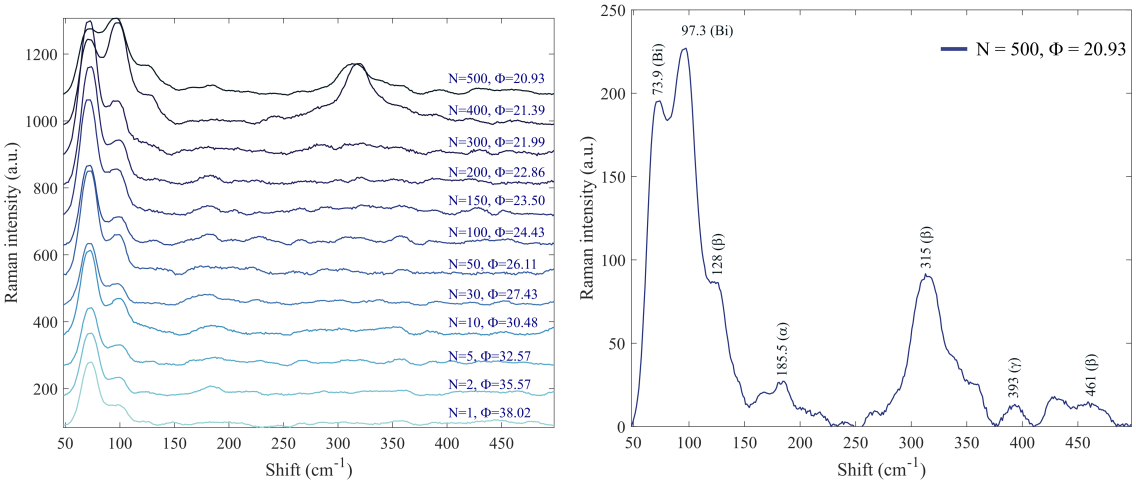

(a) (b)

Figure 39. a) Raman spectra of the irradiations corresponding to $k = 0.8$ in Fig.25 for different number of pulses N and fluence Φ (mJ/cm^2). Pulse repetition rate 5 kHz. b) Raman spectrum at the center of irradiated spot, $N = 500$ pulses, Fluence = 20.93 mJ/cm^2. The peaks are labeled with the corresponding Bi_2O_3.

Bismuth trioxide can be obtained by different techniques like pulsed laser deposition (Steele and Lewis, 2014), sputtering (Fan *et al.*, 2005), chemical vapor deposition and thermal oxidation (Condurache-Bota *et al.*, 2011; Ismail, 2006). Each one of the Bi_2O_3 polymorphs appears in different temperature ranges. The α-Bi_2O_3 (monoclinic) phase is obtained from room temperature (RT) up to 730°C. Above that temperature and up to its melting point (825°C), it transforms into δ-Bi_2O_3 (face centered cubic). The β-Bi_2O_3 (tetragonal) and γ-Bi_2O_3 (body centered cubic) are intermediate metastable phases that appear at 650°C and 640°C, respectively, during the cooling down from the $\delta-$phase. Although, it depends on the purity and texture of the samples.

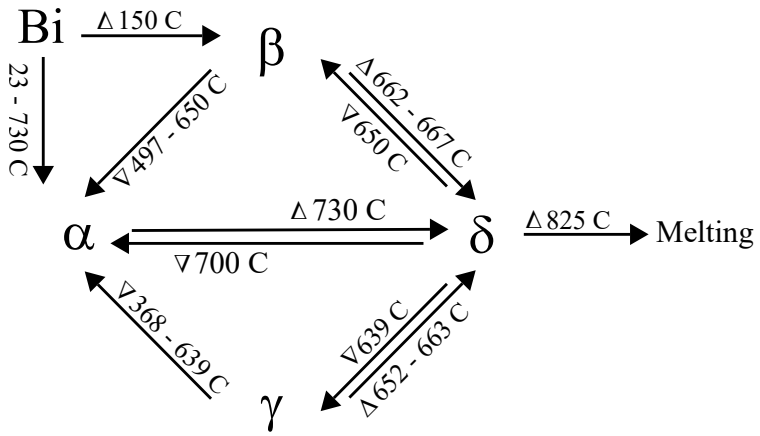

Figure 40. Transformation diagram of Bi and the four main polymorphs of Bi_2O_3 Hardcastle and Wachs (1992),Steele and Lewis (2014). The transitions are indicated by arrows with their respective temperature ranges. ∇ and Δ represent cooling and heating respectively.

et al., 2006).

Table 5 summarizes the main Raman peaks associated with Bi and Bi_2O_3 to the best of our knowledge. We used those values to label the main peaks in the Raman spectrum of the bismuth surface irradiated with 500 pulses that is shown in Fig.39-(b). Besides, we identified the β phase as the most abundant Bi_2O_3-polymorph on the film surface that results upon irradiating the sample.

Table 5. a. Zepeda 2012, b. Steele 2014, c. Hardcastle 1992, d. Narang 1994, e. Salazar-Perez 2005, f. H. T. Fan 2005, g. N. V. Skorodumova 2005

Raman frequency peaks (cm^{-1}) for Bi and Bi_2O_3 phases

Bi		α-Bi_2O_3		β-Bi_2O_3			γ-Bi_2O_3	δ-Bi_2O_3		
a	b	c	d	c	a	b	e	b	f	g
96	98		467	462	455	461	827	625	618	610
76	71	446	448	311	313	315	788			
			410	124	127	128	622			
		338	340				539			
		314	314				500			
		282	281				462			
							393			
		210	210				369			
			184				329			
		158	156				276			
		151	151				250			
			146				205			
		139	138				168			
			118				144			
			101				129			
			91				96			
			82				89			
			65				65			
			57				55			

To verify the peak in the β-Bi_2O_3 Raman spectrum at 315 cm^{-1} results from a laser-induced oxidation process, we scanned the laser beam over an extended area of the film surface (see Fig.41-a) and obtained Raman spectra in different spots within both the irradiated zone and non-irradiated zones. The scanning speed was fixed at 200 μm/s (pulse repetition rate of 5 kHz) so that the average

number of pulses per spot area was 1560. To prevent the sample from ablation, we chose the laser fluence according to equation 68 using the parameters of table 4. As expected, the irradiated area was completely coated with LIPSS (fig.39-b). The objective of acquiring several Raman-spectra on each zone is to assess the homogeneity of the spatial distribution of compounds on the film surface as well as increasing the signal to noise ratio through signal averaging.

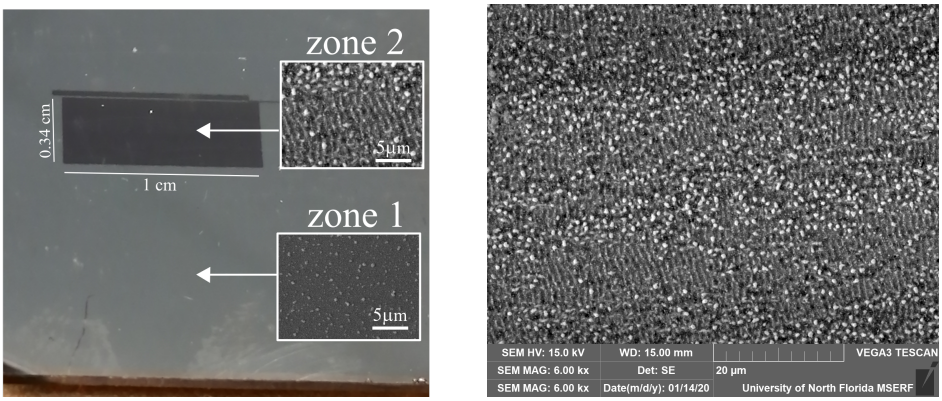

(a) (b)

Figure 41. Picture of the bismuth sample. The non-irradiated area is referred to as zone 1. Whilst zone 2 is the over-irradiated area. The irradiation parameters were: $\Phi = 8.86$ mJ/cm^2, sweep-velocity 200 μm/s, and 1560 average number of pulses. The SEM-micrographs were obtained in the Materials Science and Engineering Research Facility at the University of North Florida.

To obtain the Raman spectra we employed a T64000 triple Raman spectrometer equipped with a liquid nitrogen cooled CCD Detector, an Innova 70 Argon ion laser (central wavelength 532 nm) is used to excite the Raman signal. The Raman spectrometer belongs to the instrumentation equipment of Dr. Lev Gasparov's laboratory at the University of North Florida (UNF). After some screening experiments, we realized that the initial Raman laser power was enough to produce modification on the sample, thus, it was necessary to reduce the laser power from 400 to 40 μW. The decrease in the laser power leads to low signal levels, consequently, each measurement required a longer acquisition time; 360 s per spectrum. Each set of Raman spectra consisted of 25 measurements carried out within a squared array of equally spaced spots. The resulting spectra revealed a uniform distribution of the components in both zones. Figure 43 shows the averaged Raman spectrum corresponding to each zone.

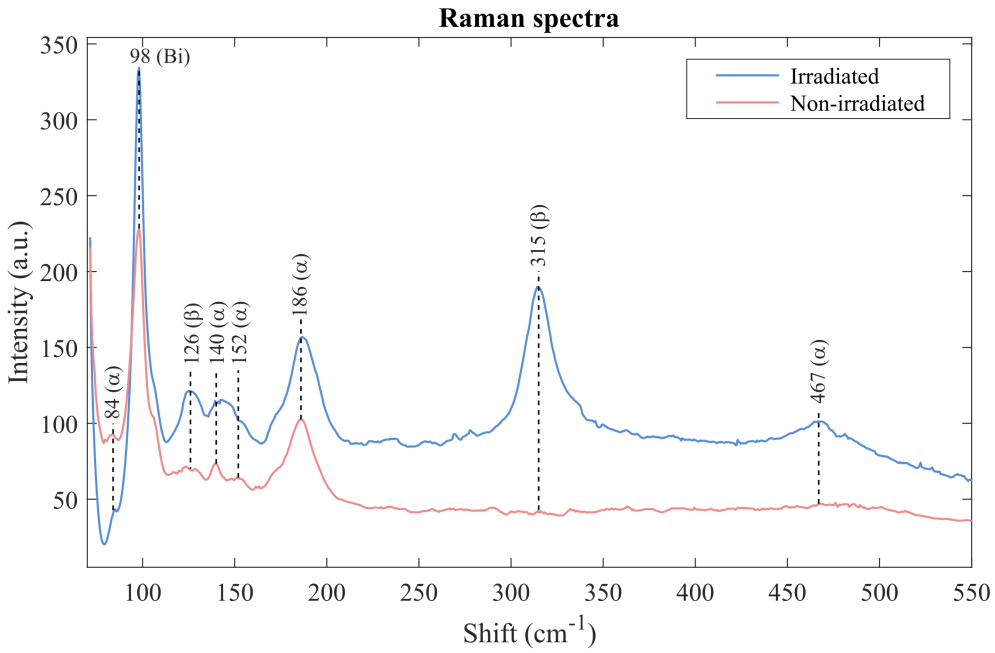

Figure 42. Raman spectra of the irradiated and non-irradiated zones. Overall average of 50 Raman spectra recorded in different spots on the sample, 2 different time series acquisitions, of 25 spectra each and at 60 s per spectrum.

The averaged spectrum of both the irradiated and non-irradiated zones shows the characteristic peak at 98 cm^{-1}, associated with pure bismuth, along with the peaks at 84, 140-146, 152, and 186 cm^{-1} associated with the α-Bi_2O_3 phase. Whereas, only the spectrum of the irradiated zone shows peaks at 315 and 467 cm^{-1} associated with the β-Bi_2O_3 and α-Bi_2O_3 phases respectively. Therefore, we conclude that an oxidation process takes place upon increasingly irradiating the material below the ablation threshold. The main product of this a laser-induced oxidation is the β-Bi_2O_3 phase. As regards to the α-Bi_2O_3, this phase can be obtained from room temperature up to 730° C (Diaz-Guerra *et al.*, 2017), additionally, it is well known that metals kept in atmospheric air tend to create a native oxide layer with of a few nanometers of thickness on their surface (Nanai *et al.*, 1997). Thus, the α-Bi_2O_3 might have been generated in ambient air conditions or during the sputtering used to deposit the film. Because of the dielectric properties of the oxide, we suggest the HSFL observed in figure 39-b on top of the LSFL, can be formed of material from the β-Bi_2O_3 material.

5.2 LSFL of TiO_2

The thermochemical laser induced periodic surface structures (TLIPSS) are generated due to metal oxidation rather than ablation (Dostovalov *et al.*, 2017), their formation of can be induced only on

thin metal films ($\leq$ 400 nm) (Dostovalov, 2017) by fast heat transfer from the irradiated area in case of bulk metal sample that results in the smoothing of temperature distribution corresponding to interference patterns, formed as a results of interference of incident and scattered radiations (Dostovalov, 2017). The topology of TLIPSS consists of oxide periodic structures with height in the range of 50–150 nm, which are orientated parallel to the direction of the electric field and its period depends on the laser wavelength and metal film thickness (Dostovalov, 2017). Previous studies (Xian-Feng Li, 2014) had demonstrated that an extremely thin (a few nanometers) layer of titanium dioxide (TiO_2) may be formed on top of the titanium film after irradiating with fs-laser light using a fluence below the titanium ablation threshold. The presence of that oxide layer may alter the energy absorption and distribution of the laser light onto the sample leading to formation of TLIPSS.

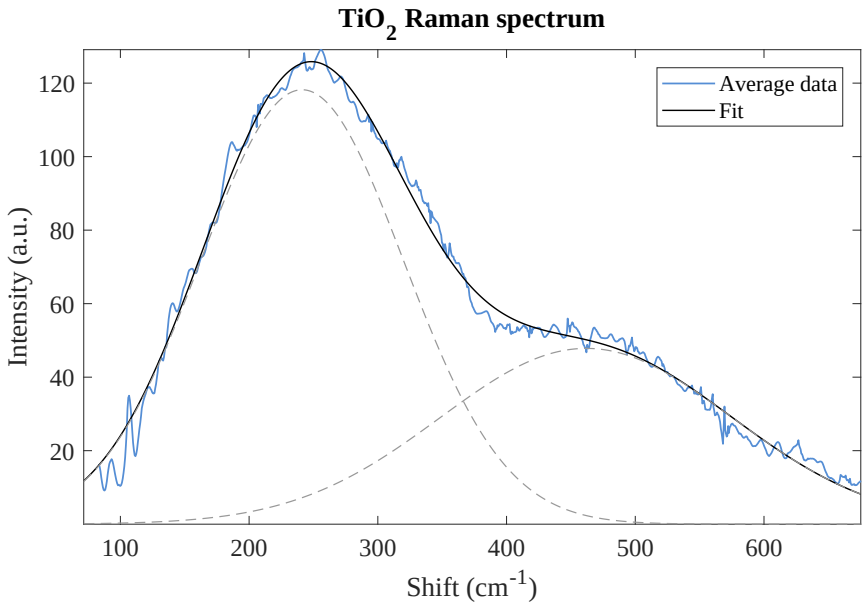

Figure 43. Black line represents the Raman spectrum of the irradiated titanium film, dotted lines the individual Blue line represents Overall average of 9 Raman spectra recorded in different irradiated spots on the sample, 2 different time series acquisitions, of 25 spectra each and at 60 s per spectrum.

Titanium dioxide is a transparent compound in the visible-near infrared region, which exhibits three polymorphs: rutile (tetragonal), brookite (orthorhombic), and anatase (tetragonal). Figure 43 shows the average Raman spectrum in the range 83 cm^{-1} to 675 cm^{-1} of the titanium film surface corresponding to the irradiated spots corresponding to $k = 0.45$ in figure 54. This study reveals two peaks at 241 cm^{-1} and 462 cm^{-2}, the first one is attributed to the characteristic titanium spectrum whereas the second one to the rutile TiO_2 phase. One of the most attractive features of titanium is its potential as a biomaterial due to its excellent chemical resistance and high strength (Shinonaga

et al., 2014). In addition, it has been recently proposed that this biocompatibility may be improved by adding a TiO_2 coating film on the titanium surface. For this reason it is relevant this procedure as a reliable coating method.

Let us focus our attention in figure 54, we can notice that when increasing the number of pulses keeping the irradiation fluence quit bellow to the ablation threshold, some LSFL emerge parallel to the laser polarization. Figure 49 shows a comparison between the LIPSS obtained in titanium irradiated at normal incidence with 10 pulses (a) and those obtained with 10^4 pulses (b), the irradiation fluences are $\Phi = 138.06$ mJ/cm^2 and $\Phi = 29.24$ mJ/cm^2 respectively, the laser of $\Lambda = 1030$ nm is horizontally polarized. The LIPSS periodicities are 770 nm (a) and 810 nm (b). The LIPSS found in figure 49-b can be sorted as thermochemical LIPSS (TLIPSS) due to the presence of oxide in its composition, the orientation parallel to laser polarization and the periodicity close to the laser wavelength.

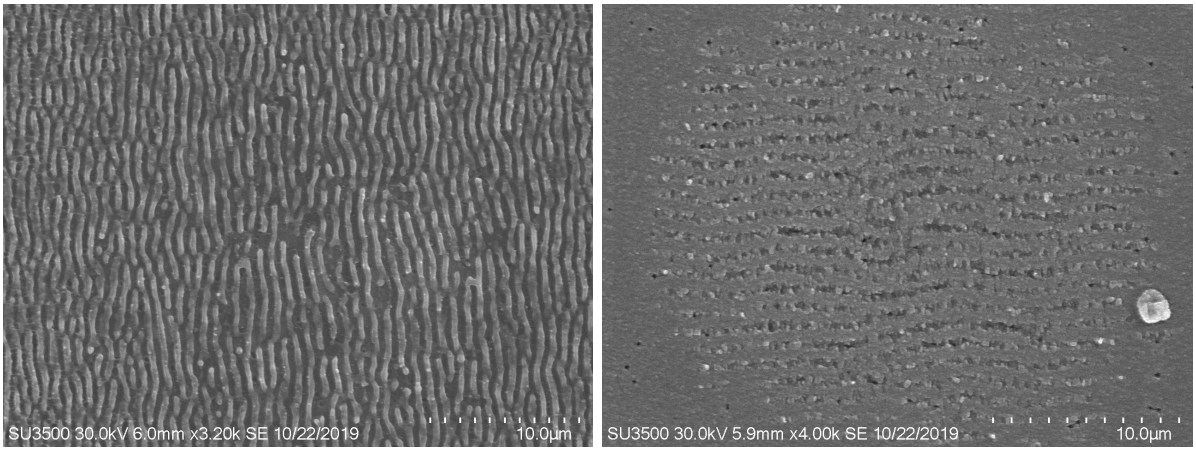

(a) a (b) b

Figure 44. Comparison of LIPSS obtained in titanium irradiated at normal incidence with 10 pulses (a) and 10^4 pulses (b). The direction of the laser polarization is horizontal.

In an attempt to predict the formation of these thermochemical LIPSS, we use the Sipe to compute the LIPSS periodicity of a system formed by a TiO_2 layer on top of the titanium film, we simplify the composite surface using an effective medium approximation, whose optical constants result from combining the optical constants of the underlying titanium with the optical constants of the TiO_2. We use the Bruggeman theory of the Effective Medium Approximation (EMA), assuming a different volume fractions of the composite materials. This approach describes the dielectric constant of the composite surface as

$$f_a \frac{\varepsilon_a - \varepsilon_{\text{eff}}}{\varepsilon_a + 2\varepsilon_{\text{eff}}} + (1 - f_a) \frac{\varepsilon_b - \varepsilon_{\text{eff}}}{\varepsilon_b + 2\varepsilon_{\text{eff}}} = 0, \tag{72}$$

where ε_a and ε_b are the dielectric constants of the composite materials, f_a and $(1 - f_a)$ their respective volume fractions, and ε_{eff} the effective dielectric constant. The value of the titanium dielectric constant at 1030 nm that we used for our calculations is $\varepsilon_{Ti} = -5.6174 + 23.3035i$ (Rakić *et al.*, 1998). On the other hand, rutile is a dielectric whose its crystal structure has some oxygen vacancies and its optical gap is roughly 3.2 eV (Shinonaga *et al.*, 2014; Águas *et al.*, 2008). Since the photon energy of our laser is 1.204 eV we do not expect changes in the dielectric constant due to electrons promoted to the conduction band. Consequently, we can use the following equation from (DeVore, 1951) to describe the rutile dielectric function which is valid in the wavelength range 450 - 1500 nm,

$$\varepsilon_{TiO_2} = 5.913 + \frac{2.441 \times 10^5}{\lambda^2 - 0.803 \times 10^5}. \tag{73}$$

Figure 45 shows the efficacy factor maps that result from varying the composition proportion of Ti and TiO_2.

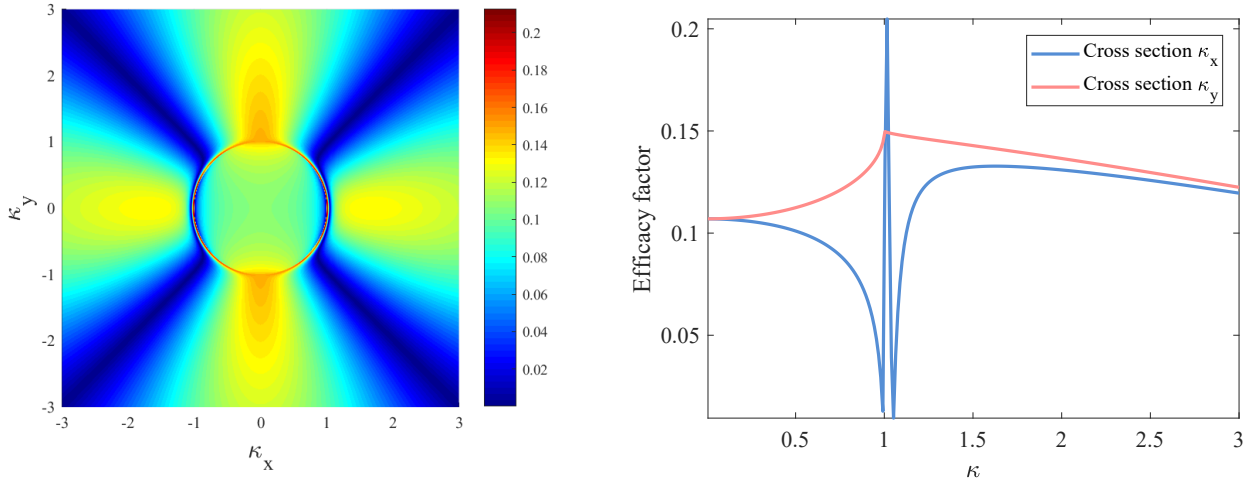

(a) 1.0 Ti, 0.0 TiO_2

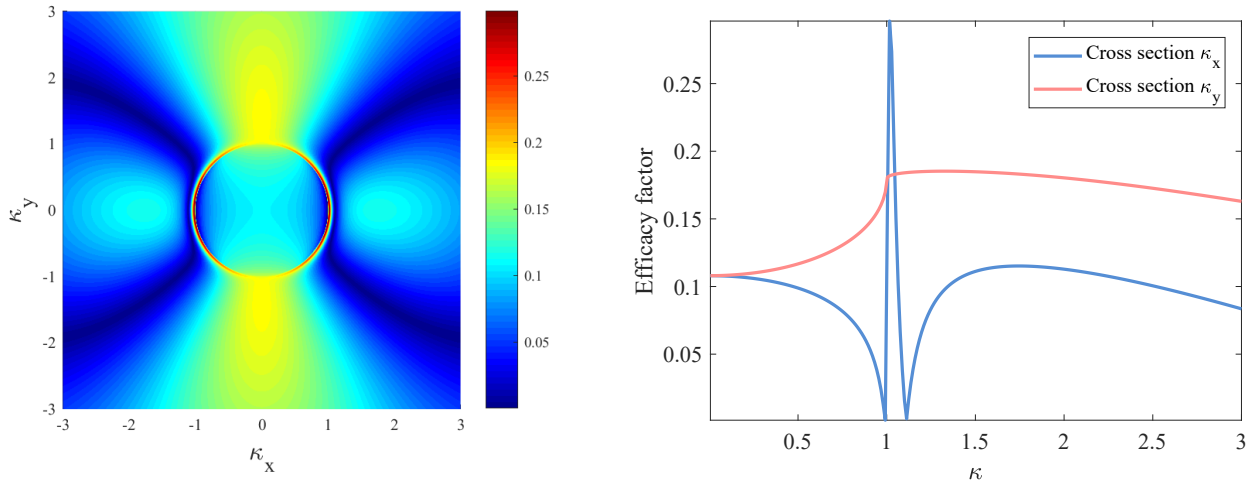

(b) 0.8 Ti, 0.2 TiO_2

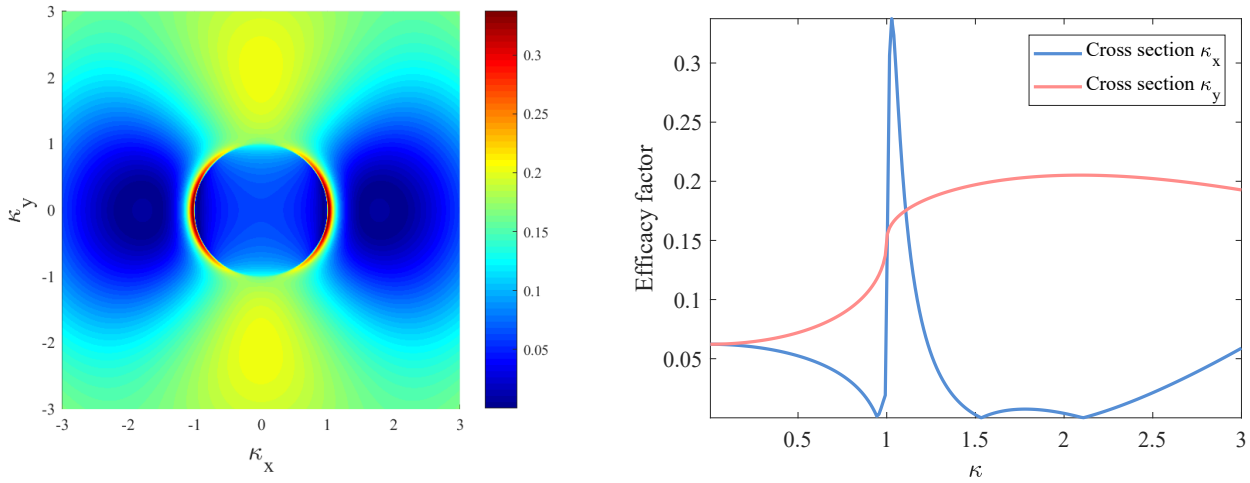

(c) 0.6 Ti, 0.4 TiO_2

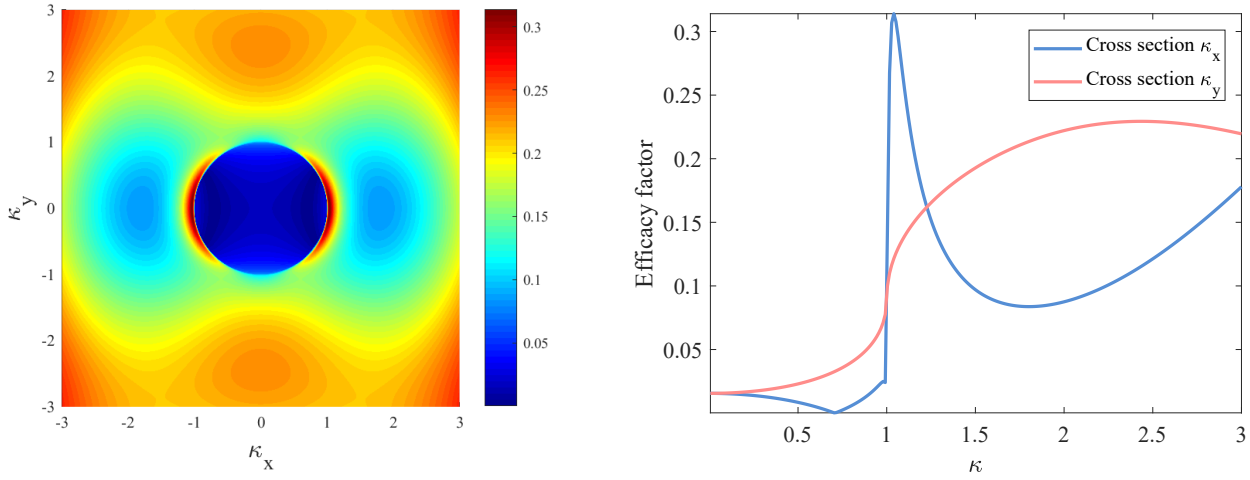

(d) 0.4 Ti, 0.6 TiO_2

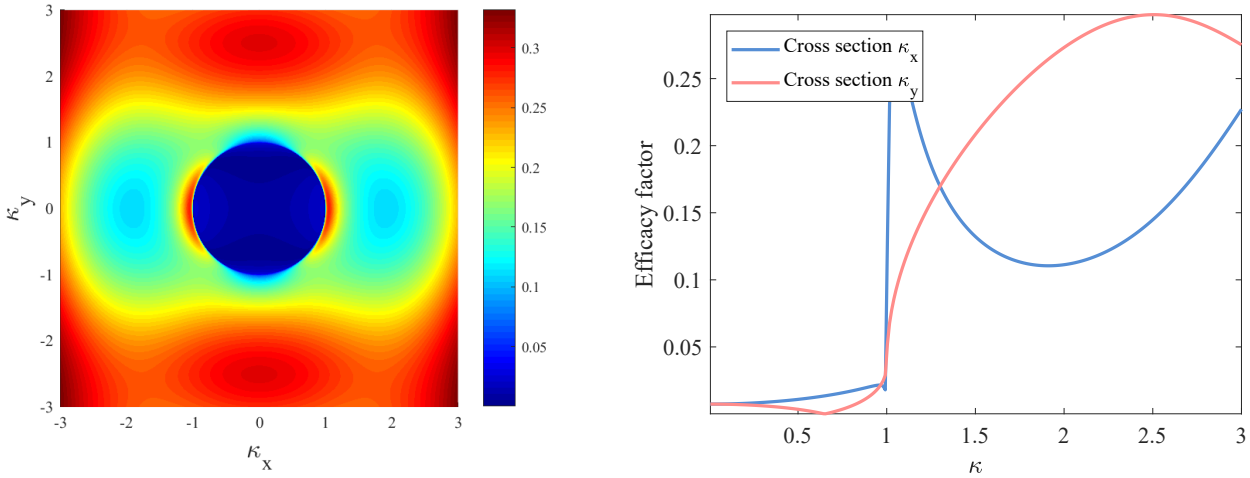

(e) 0.2 Ti, 0.8 TiO_2

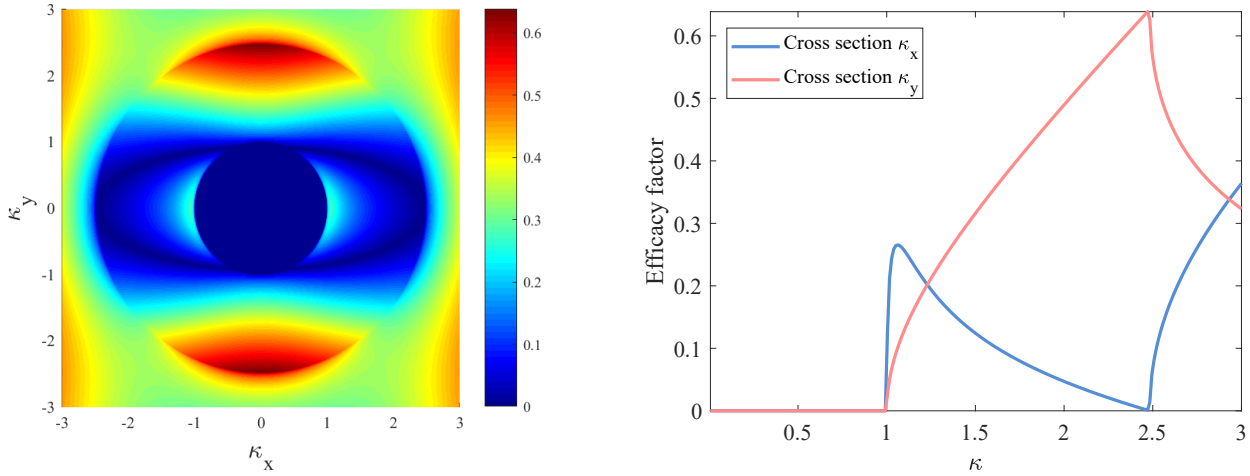

(f) 0.0 Ti, 1.0 TiO_2

Figure 45. Efficacy factor maps of a compound surface of titanium and TiO_2 varying the concentration percentages.

Table 6 summarizes the dielectric constant of the effective medium at 1030 nm as a function of the volume fractions and the LIPSS periodicity and orientations calculated with the Sipe theory. We conclude that when increasing the concentration of TiO_2, the LIPSS eventually invert their orientation with respect to the laser polarization from perpendicular to parallel. The difference between our calculations the LIPSS periods may be attributed to uncertainty in the exact proportions of Ti and TiO_2 or the unsuitable selection of the dielectric constants.

Table 6. LIPSS periods and orientations obtained from the efficacy factor maps of a compound surface of titanium and TiO_2 varying the concentration percentages.

Ti f_a	TiO_2 $(1 - f_a)$	ε_{eff}	Periodicity (nm)	Orientation
1	0	$-5.6174 + 23.3035i$	1013	$\perp$
0.9	0.1	$-3.3110 + 20.0730i$	1014	$\perp$
0.8	0.2	$-0.9226 + 17.0959i$	1014	$\perp$
0.7	0.3	$1.4011 + 14.4769i$	1002	$\perp$
0.6	0.4	$3.4521 + 12.1824i$	1002	$\perp$
0.5	0.5	$5.1115 + 10.070i$	1002	$\perp$
0.4	0.6	$6.3532 + 8.0162i$	990	$\perp$
0.3	0.7	$7.1654 + 5.9514i$	990	$\perp$
0.2	0.8	$7.5006 + 3.8517i$	411	$\parallel$
0.1	0.9	$7.2318 + 1.7649i$	415	$\parallel$
0.0	1.0	6.1619	417	$\parallel$

Chapter 6. Numerical approach: FDTD method

The formation of LIPSS is based on multiple pulse irradiation during which the surface topography evolves with the number of pulses. Several effects occur during and in between consecutive pulses; among the different inter-pulse effects we can highlight: topographical changes, structural changes, chemical changes, incubation effects, and self-organization. While the intra-pulse effects may include: transient change of optical properties and defect states, surface wave excitation, nonlinear effects, and inhomogeneous absorption. To shed light on the intra-pulse effects, we present a numerical model based on the finite-difference time-domain method (FDTD) to model the formation of ablative LIPSS simulating our irradiation conditions with the possibility of tailoring the irradiating surface topography. In addition, we incorporated an auxiliary differential equation (ADE) method to address the propagation of electromagnetic waves in lossy media, which allows us to calculate the fraction of the electric field power that is transferred into conduction current by means of ohmic losses. The induced currents generate a localized increase in temperature, which ultimately leads to the ablation of the material. This last step is incorporated into the model by a holographic ablation method (HAM). Our model uses subroutines developed by (Elsherbeni and Demir, 2009) to create and display the simulation domain.

6.1 Fundamentals of the FDTD method

It is convenient to write the equations 12a and 12b in a form suitable for the treatment of lossy materials. To this aim, we start by substituting the constitutive relation derived in section 2.2.1 for linear, isotropic materials, $\widetilde{\mathbf{D}} = \varepsilon_0 \tilde{\varepsilon}_r \widetilde{\mathbf{E}}(\mathbf{k}, \omega)$, into the Fourier transform of the Ampere's law , $i\mathbf{k} \times \widetilde{\mathbf{H}} = -i\omega \widetilde{\mathbf{D}} + \widetilde{\mathbf{J}}$. Then, let us separate the complex relative permittivity into its real and imaginary parts $\tilde{\varepsilon}_r = \mathrm{Re}\{\tilde{\varepsilon}_r\} + i\mathrm{Im}\{\tilde{\varepsilon}_r\}$. So that, we obtain the equation

$$i\mathbf{k} \times \widetilde{\mathbf{H}} = -i\omega\varepsilon_0 \mathrm{Re}\{\tilde{\varepsilon}_r\}\widetilde{\mathbf{E}} + \omega\varepsilon_0 \mathrm{Im}\{\tilde{\varepsilon}_r\}\widetilde{\mathbf{E}} + \widetilde{\mathbf{J}}. \tag{74}$$

Introducing the electric conductivity $\sigma^e = \varepsilon_0 \omega \mathrm{Im}\{\tilde{\varepsilon}\}$, the inverse Fourier transform, of equation 74 becomes

$$\nabla \times \mathbf{H} = \varepsilon_0 \frac{\partial \varepsilon_r \mathbf{E}}{\partial t} + \sigma^e \mathbf{E} + \mathbf{J}. \tag{75}$$

If we further assume non-dispersive materials, the time-depended Maxwell's curl equations are

$$\nabla \times \mathbf{H} = \varepsilon_0 \varepsilon_r \frac{\partial \mathbf{E}}{\partial t} + \sigma^e \mathbf{E} + \mathbf{J}, \tag{76a}$$

$$\nabla \times \mathbf{E} = -\mu \frac{\partial \mathbf{H}}{\partial t}. \tag{76b}$$

Let us consider an arbitrary continuous function $f(x)$, sampled at any number of discrete points separated by a sampling period Δx. The central-difference method is a second-order accurate numerical method to approximate the derivatives of $f(x)$ at x using the immediate forward $(x+\Delta x)$ and backward $(x-\Delta x)$ points around the center. According to this method, the first- and second-order derivatives of $f(x)$, can be approximated by the following equations

$$f'(x) = \frac{f(x+\Delta x) - f(x-\Delta x)}{2\Delta x} + O(\Delta x^2), \tag{77a}$$

$$f''(x) = \frac{f(x+\Delta x) - 2f(x) + f(x-\Delta x)}{(\Delta x)^2} + O(\Delta x^2). \tag{77b}$$

The FDTD method solves the time-dependent Maxwell's curl equations, represented in a discrete form in space and time by means of the central difference formula (CDF). With this aim, we expand Maxwell's curl equations 76a and 76b in the following set of scalar equations

$$\frac{\partial E_x}{\partial t} = \frac{1}{\varepsilon_0 \varepsilon_x}\left(\frac{\partial H_z}{\partial y} - \frac{\partial H_y}{\partial z} - \sigma_x^e E_x - J_x\right), \tag{78a}$$

$$\frac{\partial E_y}{\partial t} = \frac{1}{\varepsilon_0 \varepsilon_y}\left(\frac{\partial H_x}{\partial z} - \frac{\partial H_z}{\partial x} - \sigma_y^e E_y - J_y\right), \tag{78b}$$

$$\frac{\partial E_z}{\partial t} = \frac{1}{\varepsilon_0 \varepsilon_z}\left(\frac{\partial H_y}{\partial x} - \frac{\partial H_x}{\partial y} - \sigma_z^e E_z - J_z\right), \tag{78c}$$

$$\frac{\partial H_x}{\partial t} = \frac{1}{\mu_x}\left(\frac{\partial E_y}{\partial z} - \frac{\partial E_z}{\partial y}\right), \tag{78d}$$

$$\frac{\partial H_y}{\partial t} = \frac{1}{\mu_y}\left(\frac{\partial E_z}{\partial x} - \frac{\partial E_x}{\partial z}\right), \tag{78e}$$

$$\frac{\partial H_z}{\partial t} = \frac{1}{\mu_z}\left(\frac{\partial E_x}{\partial y} - \frac{\partial E_y}{\partial x}\right). \tag{78f}$$

Additionally, the three dimensional geometry associated with the problem is divided into a spatial grid composed of $N_x \times N_y \times N_z$ cells referred to as Yee cells after Kane Yee. As shown in figure 46, the electric and magnetic field components are placed at specific discrete positions in the Yee cells to create a simple picture of a three-dimensional space being filled by an interlinked array of Faraday's law and Ampere's law contours. It is worth mentioning that the divergence Maxwell equations 5c and 5d are automatically satisfied by solving the FDTD updating equations.

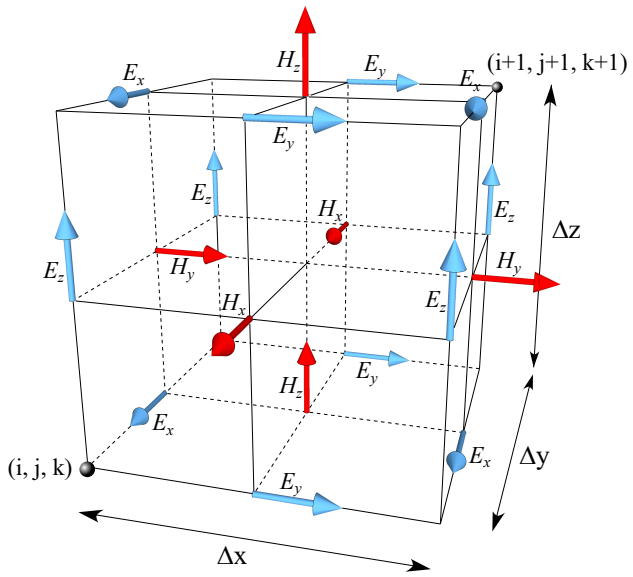

Figure 46. Components of **E** and **H** fields on a Yee cell arrangement indexed as (i, j, k). The electric field components are placed at the centers of the edges heading parallel to the edges, whereas the magnetic field components are placed at the centers of the faces heading normal to the faces.

To illustrate how the FDTD updating equations are derived, let us consider the scalar equation

78a associated with the electric field component E_x, taking $E_x(i,j,k)$ as the center point for the CDF in space and the time instant $(n+\frac{1}{2})\Delta t$ as the center points for the CDF in time. The representation of equation 78a in finite differences is

$$\begin{aligned}\frac{E_x^{n+1}(i,j,k)-E_x^{n}(i,j,k)}{\Delta t} =& \frac{1}{\varepsilon_0\varepsilon_x(i,j,k)}\frac{H_z^{n+\frac{1}{2}}(i,j,k)-H_z^{n+\frac{1}{2}}(i,j-1,k)}{\Delta y}\\ &-\frac{1}{\varepsilon_0\varepsilon_x(i,j,k)}\frac{H_y^{n+\frac{1}{2}}(i,j,k)-H_y^{n+\frac{1}{2}}(i,j,k-1)}{\Delta z}\\ &-\frac{\sigma_x^e(i,j,k)}{\varepsilon_0\varepsilon_x(i,j,k)}E_x^{n+\frac{1}{2}}(i,j,k)-\frac{1}{\varepsilon_0\varepsilon_x(i,j,k)}J_x^{n+\frac{1}{2}}(i,j,k).\end{aligned} \tag{79}$$

The electric field components are calculated at the integer time-step indicated by the superscript n, whereas the magnetic field components at the half-integer indicated by the superscript $n+\frac{1}{2}$. In consequence, we need to approximate the value of the electric field component E_x at time instant $(n+\frac{1}{2})\Delta t$ in the right-hand side of equation 79 in terms of the electric field components at the time instants $n\Delta t$ and $(n+1)\Delta t$, via the arithmetic average,

$$E_x^{n+\frac{1}{2}}(i,j,k)=\frac{E_x^{n+1}(i,j,k)+E_x^{n}(i,j,k)}{2}. \tag{80}$$

After substituting equation 80 into equation 79 and collecting like terms, the expression for the electric field component at time-step, $n+1$ is

$$\begin{aligned}E_x^{n+1}(i,j,k) =& \frac{2\varepsilon_0\varepsilon_x(i,j,k)-\Delta t\sigma_x^e(i,j,k)}{2\varepsilon_0\varepsilon_x(i,j,k)+\Delta t\sigma_x^e(i,j,k)}E_x^{n}(i,j,k)\\ &+\frac{2\Delta t}{\left(2\varepsilon_0\varepsilon_x(i,j,k)+\Delta t\sigma_x^e(i,j,k)\right)\Delta y}\left(H_z^{n+\frac{1}{2}}(i,j,k)-H_z^{n+\frac{1}{2}}(i,j-1,k)\right)\\ &-\frac{2\Delta t}{\left(2\varepsilon_0\varepsilon_x(i,j,k)+\Delta t\sigma_x^e(i,j,k)\right)\Delta z}\left(H_y^{n+\frac{1}{2}}(i,j,k)-H_y^{n+\frac{1}{2}}(i,j,k-1)\right)\\ &-\frac{2\Delta t}{2\varepsilon_0\varepsilon_x(i,j,k)+\Delta t\sigma_x^e(i,j,k)}J_x^{n+\frac{1}{2}}(i,j,k).\end{aligned} \tag{81}$$

Equation 81 is known as the FDTD updating equation for $E_x^{n+1}(i,j,k)$. Following the same methodology, we can obtain the FDTD updating equations for $E_y^{n+1}(i,j,k)$ and $E_z^{n+1}(i,j,k)$, $H_x^{n+\frac{1}{2}}(i,j,k)$, $H_y^{n+\frac{1}{2}}(i,j,k)$, and $H_z^{n+\frac{1}{2}}(i,j,k)$. Therefore the six components of electro-magnetic fields are:

$$
\begin{aligned}
E_x^{n+1}(i,j,k) =& C_{E_x}(i,j,k) \times E_x^n(i,j,k) \\
&+ C_{E_xH_z}(i,j,k) \times \left(H_z^{n+\frac{1}{2}}(i,j,k) - H_z^{n+\frac{1}{2}}(i,j-1,k) \right) \\
&+ C_{E_xH_y}(i,j,k) \times \left(H_y^{n+\frac{1}{2}}(i,j,k) - H_y^{n+\frac{1}{2}}(i,j,k-1) \right), \\
&+ C_{E_xJ}(i,j,k) \times J_x^{n+\frac{1}{2}}(i,j,k),
\end{aligned} \tag{82}
$$

where

$$
\begin{aligned}
C_{E_x}(i,j,k) =& \frac{2\varepsilon_0\varepsilon_x(i,j,k) - \Delta t\sigma_x^e(i,j,k)}{2\varepsilon_0\varepsilon_x(i,j,k) + \Delta t\sigma_x^e(i,j,k)} \\
C_{E_xH_z}(i,j,k) =& \frac{2\Delta t}{(2\varepsilon_0\varepsilon_x(i,j,k) + \Delta t\sigma_x^e(i,j,k))\,\Delta y}, \\
C_{E_xH_y}(i,j,k) =& -\frac{2\Delta t}{(2\varepsilon_0\varepsilon_x(i,j,k) + \Delta t\sigma_x^e(i,j,k))\,\Delta z}, \\
C_{E_xJ}(i,j,k) =& -\frac{2\Delta t}{2\varepsilon_0\varepsilon_x(i,j,k) + \Delta t\sigma_x^e(i,j,k)}.
\end{aligned} \tag{83}
$$

$$
\begin{aligned}
E_y^{n+1}(i,j,k) =& C_{E_y}(i,j,k) \times E_y^n(i,j,k) \\
&+ C_{E_yH_x}(i,j,k) \times \left(H_x^{n+\frac{1}{2}}(i,j,k) - H_x^{n+\frac{1}{2}}(i,j,k-1) \right) \\
&+ C_{E_yH_y}(i,j,k) \times \left(H_z^{n+\frac{1}{2}}(i,j,k) - H_z^{n+\frac{1}{2}}(i-1,j,k) \right) \\
&+ C_{E_yJ}(i,j,k) \times J_y^{n+\frac{1}{2}}(i,j,k),
\end{aligned} \tag{84}
$$

where

$$
\begin{aligned}
C_{E_y}(i,j,k) =& \frac{2\varepsilon_0\varepsilon_y(i,j,k) - \Delta t\sigma_y^e(i,j,k)}{2\varepsilon_0\varepsilon_y(i,j,k) + \Delta t\sigma_y^e(i,j,k)} \\
C_{E_yH_x}(i,j,k) =& \frac{2\Delta t}{\left(2\varepsilon_0\varepsilon_y(i,j,k) + \Delta t\sigma_y^e(i,j,k)\right)\Delta y}, \\
C_{E_yH_z}(i,j,k) =& -\frac{2\Delta t}{\left(2\varepsilon_0\varepsilon_y(i,j,k) + \Delta t\sigma_y^e(i,j,k)\right)\Delta x}, \\
C_{E_yJ}(i,j,k) =& -\frac{2\Delta t}{2\varepsilon_0\varepsilon_y(i,j,k) + \Delta t\sigma_y^e(i,j,k)}.
\end{aligned} \tag{85}
$$

$$
\begin{aligned}
E_z^{n+1}(i,j,k) =& C_{E_z}(i,j,k) \times E_z^n(i,j,k) \\
&+ C_{E_z H_y}(i,j,k) \times \left(H_y^{n+\frac{1}{2}}(i,j,k) - H_y^{n+\frac{1}{2}}(i-1,j,k) \right) \\
&+ C_{E_z H_x}(i,j,k) \times \left(H_x^{n+\frac{1}{2}}(i,j,k) - H_x^{n+\frac{1}{2}}(i,j-1,k) \right) \\
&+ C_{E_z J}(i,j,k) \times J_z^{n+\frac{1}{2}}(i,j,k),
\end{aligned} \tag{86}
$$

where

$$
\begin{aligned}
C_{E_z}(i,j,k) =& \frac{2\varepsilon_0\varepsilon_z(i,j,k) - \Delta t \sigma_z^e(i,j,k)}{2\varepsilon_0\varepsilon_z(i,j,k) + \Delta t \sigma_z^e(i,j,k)} \\
C_{E_z H_y}(i,j,k) =& \frac{2\Delta t}{\left(2\varepsilon_0\varepsilon_z(i,j,k) + \Delta t \sigma_z^e(i,j,k)\right)\Delta x}, \\
C_{E_z H_x}(i,j,k) =& -\frac{2\Delta t}{\left(2\varepsilon_0\varepsilon_z(i,j,k) + \Delta t \sigma_z^e(i,j,k)\right)\Delta y}, \\
C_{E_z J}(i,j,k) =& -\frac{2\Delta t}{2\varepsilon_0\varepsilon_z(i,j,k) + \Delta t \sigma_z^e(i,j,k)}.
\end{aligned} \tag{87}
$$

$$
\begin{aligned}
H_x^{n+\frac{1}{2}}(i,j,k) =& C_{H_x}(i,j,k) \times H_x^{n-\frac{1}{2}}(i,j,k) \\
&+ C_{H_x E_y}(i,j,k) \times \left(E_y^n(i,j,k+1) - E_y^n(i,j,k) \right) \\
&+ C_{H_x E_z}(i,j,k) \times \left(E_z^n(i,j+1,k) - E_z^n(i,j,k) \right),
\end{aligned} \tag{88}
$$

where

$$
\begin{aligned}
C_{H_x}(i,j,k) =& \frac{2\mu_x(i,j,k) - \Delta t \sigma_x^m(i,j,k)}{2\mu_x(i,j,k) + \Delta t \sigma_x^m(i,j,k)} \\
C_{H_x E_y}(i,j,k) =& \frac{2\Delta t}{\left(2\mu_x(i,j,k) + \Delta t \sigma_x^m(i,j,k)\right)\Delta z}, \\
C_{H_x E_z}(i,j,k) =& -\frac{2\Delta t}{\left(2\mu_x(i,j,k) + \Delta t \sigma_x^m(i,j,k)\right)\Delta y}.
\end{aligned} \tag{89}
$$

$$
\begin{aligned}
H_y^{n+\frac{1}{2}}(i,j,k) =& C_{H_y}(i,j,k) \times H_y^{n-\frac{1}{2}}(i,j,k) \\
&+ C_{H_yE_z}(i,j,k) \times (E_z^n(i+1,j,k) - E_z^n(i,j,k)) \\
&+ C_{H_yE_x}(i,j,k) \times (E_x^n(i,j,k+1) - E_x^n(i,j,k)),
\end{aligned} \tag{90}
$$

where

$$
\begin{aligned}
C_{H_y}(i,j,k) =& \frac{2\mu_y(i,j,k) - \Delta t \sigma_y^m(i,j,k)}{2\mu_y(i,j,k) + \Delta t \sigma_y^m(i,j,k)} \\
C_{H_yE_z}(i,j,k) =& \frac{2\Delta t}{\left(2\mu_y(i,j,k) + \Delta t \sigma_y^m(i,j,k)\right)\Delta x}, \\
C_{H_yE_x}(i,j,k) =& -\frac{2\Delta t}{\left(2\mu_y(i,j,k) + \Delta t \sigma_y^m(i,j,k)\right)\Delta z}.
\end{aligned} \tag{91}
$$

$$
\begin{aligned}
H_z^{n+\frac{1}{2}}(i,j,k) =& C_{H_z}(i,j,k) \times H_z^{n-\frac{1}{2}}(i,j,k) \\
&+ C_{H_zE_x}(i,j,k) \times (E_x^n(i,j+1,k) - E_x^n(i,j,k)) \\
&+ C_{H_zE_y}(i,j,k) \times \left(E_y^n(i+1,j,k) - E_y^n(i,j,k)\right),
\end{aligned} \tag{92}
$$

where

$$
\begin{aligned}
C_{H_z}(i,j,k) =& \frac{2\mu_z(i,j,k) - \Delta t \sigma_z^m(i,j,k)}{2\mu_z(i,j,k) + \Delta t \sigma_z^m(i,j,k)}, \\
C_{H_zE_x}(i,j,k) =& \frac{2\Delta t}{(2\mu_z(i,j,k) + \Delta t \sigma_z^m(i,j,k))\Delta y}, \\
C_{H_zE_y}(i,j,k) =& -\frac{2\Delta t}{(2\mu_z(i,j,k) + \Delta t \sigma_z^m(i,j,k))\Delta x}.
\end{aligned} \tag{93}
$$

6.1.1 Numerical stability of FDTD method

As mentioned previously, the simulated domain is approximated by a staircase-gridding composed of small Yee cells. The dimensions of each cell correspond to the space increments Δx, Δ_y, and Δ_z. Consequently, the smaller the increments, the more accurate the approximation will result. Nevertheless, the cost of choosing extremely small increments is the reduction in computational speed and an increase in memory usage. It is commonly accepted choosing the cell dimensions in

a way that ten or twenty cells may fit within the shortest wavelength to obtain accurate results (Skolski, 2010). In 1975, Taflove and Brodwin studied the numerical stability of the FDTD method applied to lossless media (Taflove and Brodwin, 1975), and determined that the time step Δt must exhibit a specific bound relative to the lattice space increments. This constriction can be formulated as a criterion, referred to as the Courant-Friedrichs-Lewy (CFL) condition, expressed as

$$\Delta t_{max} \leq \frac{1}{c\sqrt{\left(\frac{1}{\Delta x}\right)^2 + \left(\frac{1}{\Delta y}\right)^2 + \left(\frac{1}{\Delta z}\right)^2}}. \tag{94}$$

Fulfilling the inequality of equation 94 ensures that the wave cannot travel more than one cell size during one time-step. Despite this condition was developed for a lossless medium, Chun *et al* demonstrated the same stability criterion is valid in Drude media (Chun, 2013). However, regardless of the geometrical grid dimensions, the FDTD method becomes unstable when ε_r is negative (Römer *et al.*, 2014). Therefore the dispersive media response needs to be handled by a Drude or Lorentz-Drude model.

6.1.2 Modeling dispersive media using ADE technique

Up to this point, we have developed the FDTD updating equations assuming that the material permittivity is a constant parameter. However, this is not true for dispersive materials, particularly metals, whose permittivity values make the FDTD method to become unstable. To simulate frequency-dispersive materials, we need to modify the electric field updating equations by incorporating a Drude-Lorentz model. In subsection 2.2.4, we expressed the material permittivity of frecuency-dispersive materials as a sum of rational functions of the laser frequency (poles) of the form

$$\varepsilon(\omega) = \varepsilon_\infty - \frac{\omega_p^2}{\omega^2 + i\Gamma_D\omega} + \sum_{j=1}^{P} \frac{A_j(\varepsilon_s - \varepsilon_\infty)\omega_j^2}{\omega_j^2 - i\Gamma_j\omega - \omega^2}. \tag{95}$$

For convenience, we will express the Drude contribution as a particular case of the Lorentz oscillators when the restoring force and the resonance frequency are null. Hence, defining $\Delta\varepsilon = \varepsilon_s - \varepsilon_\infty$, we can rewrite equation 95 as

$$\varepsilon(\omega) = \varepsilon_\infty + \sum_{j=0}^{P} \frac{A_j \Delta\varepsilon \omega_j^2}{B_j \omega_j^2 - i\Gamma_j \omega - \omega^2}. \tag{96}$$

We can insert the frequency-depend permittivity of eq.96 into the Fourier transform of the Ampere's law (eq.75) in absence of free currents,

$$\nabla \times \widetilde{\mathbf{H}} = -i\omega\varepsilon_0 \left(\varepsilon_\infty + \sum_{j=0}^{P} \frac{A_j \Delta\varepsilon \omega_j^2}{B_j \omega_j^2 - i\Gamma_j \omega - \omega^2} \right) \widetilde{\mathbf{E}} + \sigma^e \widetilde{\mathbf{E}}, \tag{97a}$$

$$\nabla \times \widetilde{\mathbf{H}} = -i\omega\varepsilon_0\varepsilon_\infty \widetilde{\mathbf{E}} + \sigma^e \widetilde{\mathbf{E}} - \sum_{j=0}^{P} i\omega \left(\frac{A_j \varepsilon_0 \Delta\varepsilon \omega_j^2}{B_j \omega_j^2 - i\Gamma_j \omega - \omega^2} \widetilde{\mathbf{E}} \right). \tag{97b}$$

Let us define the induced polarization,

$$\widetilde{\mathbf{Q}}_j \equiv \frac{A_j \varepsilon_0 \Delta\varepsilon \omega_j^2}{B_j \omega_j^2 - i\Gamma_j \omega - \omega^2} \widetilde{\mathbf{E}}, \tag{98}$$

therefore, the Ampere's law for dispersive materials can be written in the time domain as

$$\nabla \times \mathbf{H} = \varepsilon_0\varepsilon_\infty \frac{\partial \mathbf{E}}{\partial t} + \sigma^e \mathbf{E} + \sum_{j}^{P} \frac{\partial \mathbf{Q}_j}{\partial t}. \tag{99}$$

We notice that the last term in this equation represents the induced polarization currents, $\mathbf{J}_j = \frac{d\mathbf{Q}_j}{dt}$. Let us now express the equation 99 in finite differences via the central difference approximation, so that the curl of the magnetic field at time step $(n + \frac{1}{2})$ is given by

$$\nabla \times \mathbf{H}^{n+\frac{1}{2}} = \varepsilon_0\varepsilon_\infty \left(\frac{\mathbf{E}^{n+1} - \mathbf{E}^n}{\Delta t} \right) + \sigma \mathbf{E}^{n+\frac{1}{2}} + \sum_{p=1}^{P} \left(\frac{\mathbf{Q}^{n+1} - \mathbf{Q}^n}{\Delta t} \right). \tag{100}$$

Upon substituting equation 80 into eq.100, we are able to obtain an updating equation for the electric field that includes the contribution of the induced polarization,

$$\mathbf{E}^{n+1} = \frac{2\varepsilon_0\varepsilon_\infty - \sigma\Delta t}{2\varepsilon_0\varepsilon_\infty + \sigma\Delta t}\mathbf{E}^n + \frac{2\Delta t}{2\varepsilon_0\varepsilon_\infty + \sigma\Delta t}\nabla \times \mathbf{H}^{n+\frac{1}{2}} - \frac{2}{2\varepsilon_0\varepsilon_\infty + \sigma\Delta t}\sum_{p=1}^{P}(\mathbf{Q}_j^{n+1} - \mathbf{Q}_j^n). \tag{101}$$

It is necessary to derive an updating equation for $\mathbf{Q}_j$. We start by multiplying both sides of eq.98 by the denominator of the right-side fraction,

$$-\omega^2\widetilde{\mathbf{Q}}_j - i\omega\Gamma_j\widetilde{\mathbf{Q}}_j + B_j\omega_j^2\widetilde{\mathbf{Q}}_j = A_j\varepsilon_0\Delta\varepsilon\omega_j^2\widetilde{\mathbf{E}}. \tag{102}$$

Taking the inverse Fourier transform of equation 102, we obtain the following differential equation for $\mathbf{Q}$ in the time domain,

$$\frac{\partial^2\mathbf{Q}_j}{\partial t^2} + \Gamma_j\frac{\partial\mathbf{Q}_j}{\partial t} + B_j\omega_j^2\mathbf{Q}_j = A_j\varepsilon_0\Delta\varepsilon\omega_j^2\mathbf{E}. \tag{103}$$

By using the central difference formulas 77a and 77b, the equation 103 can be approximated as

$$\left(\frac{\mathbf{Q}_j^{n+1} - 2\mathbf{Q}_j^n + \mathbf{Q}_j^{n-1}}{(\Delta t)^2}\right) + \Gamma_j\left(\frac{\mathbf{Q}_j^{n+1} - \mathbf{Q}_j^{n-1}}{2\Delta t}\right) + B_j\omega_j^2\mathbf{Q}_j^n = A_j\varepsilon_0\Delta\varepsilon\omega_j^2\mathbf{E}^n. \tag{104}$$

Solving for $\mathbf{Q}_j^{n+1}$ allows us to obtain an updating equation for the induced polarization $\mathbf{Q}$ in the framework of the Drude-Lorentz model,

$$\mathbf{Q}_j^{n+1} = \frac{4 - 2B_j(\Delta_t\omega_j)^2}{\Gamma_j\Delta t + 2}\mathbf{Q}_j^n + \frac{\Gamma_j\Delta t - 2}{\Gamma_j\Delta t + 2}\mathbf{Q_j}^{n-1} + \frac{2A_j\varepsilon_0\Delta\varepsilon(\Delta t\omega_j)^2}{\Gamma_j\Delta t + 2}\mathbf{E}^n. \tag{105}$$

Equations 105 and 101 allow us to describe dispersive media in the FDTD framework. For this reason, this method is known as the auxiliary differential equation (ADE) technique.

6.1.3 Total-field scattered-field technique

Scattered fields result from the interaction of an incident field with scattering objects. As shown in figure 47b, the total-field scattered-field (TF/SF) technique divides the simulation domain into

two nested regions. All scattering objects are placed within the core region known as total-field region (TF-region) through which the incident and scattered fields superpose. Unlike this region, only scattered waves propagate through in the scattered-field region (SF-region) which surrounds the TF-region. At the boundary between the TF and SF regions, there is a discontinuity of the electromagnetic fields corresponding to the source of the incident fields, known at any grid point of the whole domain. On the other hand, To simulate an infinite substrate we use periodic lateral boundaries. The top and bottom of the simulation domain are limited by a perfectly matched layer (PML) boundary to absorb outgoing waves. Due to the linearity of Maxwell's equations, the FDTD calculations of the total and scattered fields can be treated separately.

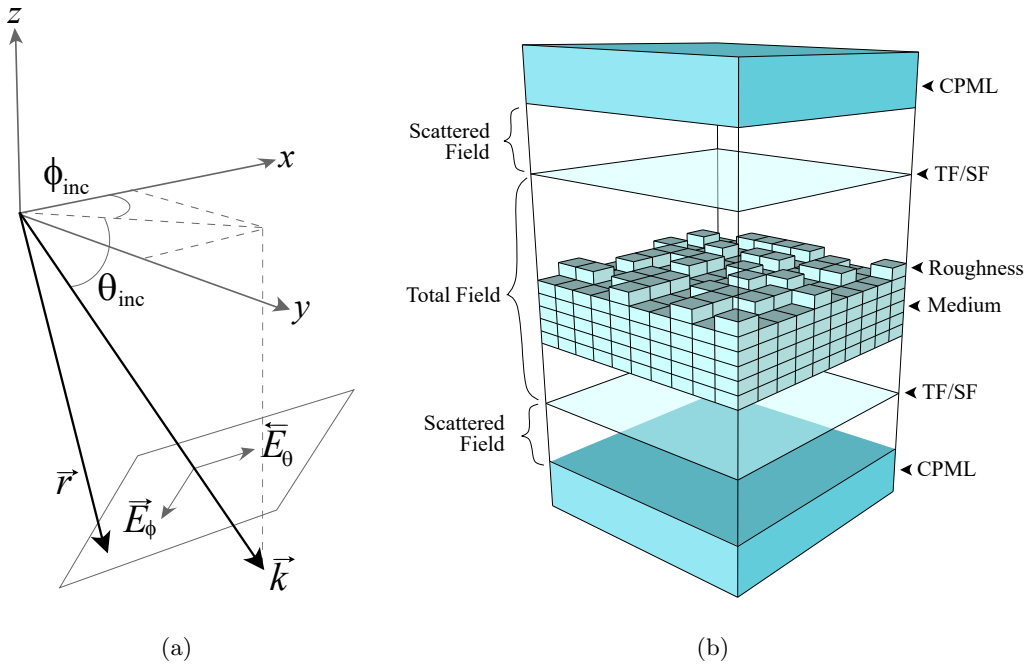

Figure 47. (a) Incident plane wave representation. (b) Problem space geometry.

6.1.4 Electromagnetic field source

The incident fields arise from the TF/SF boundary and propagate within the TF region. Figure 47a illustrates the components in spherical coordinates of a linearly polarized plane wave traveling

in the direction of the unit vector $\hat{k}$ whose expressions are

$$\mathbf{E}_{inc} = (E_\theta \hat{\theta} + E_\phi \hat{\phi}) E \left(t - \frac{\hat{k} \cdot \mathbf{r}}{c} \right), \tag{106a}$$

$$\mathbf{H}_{inc} = \frac{\varepsilon_0}{\mu_0} \hat{k} \times \mathbf{E}_{inc}. \tag{106b}$$

The mutually orthogonal components E_θ and E_ϕ describe the electric field polarization vector. The laser beam possesses a Gaussian distribution in time and space, however, due to our computational resource limits we restrict the simulations to the central region of the beam spot so that the pulse waveform $E(t - \hat{k} \cdot \mathbf{r}/c)$ is approximated by the Gaussian time-modulated plane-wave,

$$E(\mathbf{r}, t) = E_0 \cos \left(2\pi \nu_c (t - t_0 - \frac{\hat{k} \cdot \mathbf{r} - l_0}{c}) \right) \exp \left(- \left(\frac{t - t_0 - \frac{\hat{k} \cdot \mathbf{r} - l_0}{c}}{\tau} \right)^2 \right). \tag{107}$$

Variables ν_c and τ represent the wave central-frequency and the pulse half-width at $1/e^2$, respectively. The pulse width $\Delta\tau$ determines the frequency bandwidth through the expression $\Delta\tau \approx 0.966/\Delta\nu$ (Elsherbeni and Demir, 2009). To make the waveform enter into the simulation domain with negligible intensity at the beginning of FDTD iterations, we use the parameters t_0 and l_0 to shift the waveform in time and space. As we know, the fluence per pulse is equal to the energy deposited upon one single pulse irradiation; additionally, we can calculate the fluence per pulse from integrating to the laser intensity over the pulse duration. Therefore, we can estimate the value of the electric field amplitude by measuring the fluence per pulse Φ and numerically solving the following equation for E_0.

$$\Phi = \int_0^\infty |E_0|^2 \cos^2 \left(2\pi \nu_c (t - t_0) \right) e^{-2 \frac{t - t_0}{\tau}^2} dt. \tag{108}$$

Ultrafast laser processing is characterized by large peak electric fields (even orders of magnitude larger than the fields that bind electrons to atoms). For instance, figure 48 illustrates the electric field waveform corresponding to one of the pulses that we used to irradiate.

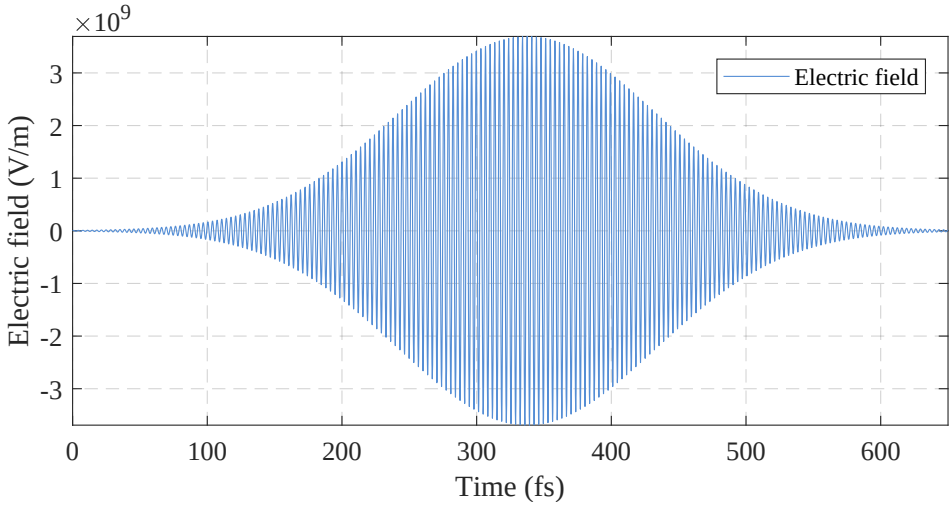

Figure 48. Electric field corresponding to a cosine modulated Gaussian waveform, central frequency $\nu_c = 291.26$ THz ($\lambda_c = 1030$ nm), pulse width at $1/e^2$ of 270 fs, and fluence per pulse of 153 mJ/cm^2.

6.1.5 Modeling ablation using the holographic ablation method

Each cell within the simulation domain possesses a set of parameters that describe its optical properties. As the electromagnetic wave propagates through the sample, part of its energy is absorbed via electric losses. The absorbed energy per cell is given by

$$En = \left(\sigma |\mathbf{E}|^2 + \sum_{p}^{P} \mathbf{J}_p \cdot \mathbf{E} \right) \Delta x \Delta y \Delta z \Delta t, \tag{109}$$

where $\mathbf{J}$ are the induced polarization currents considering P poles. The ablation of the substrate is incorporated into the simulation using a computational method known as the holographic ablation method (HAM). This consists of calculating the absorbed energy in every cell within the substrate domain. If the absorbed energy of a substrate-cell exceeds a, previously established, threshold. Then, that cell will be replace by an air-cell.

6.2 Physical model and experimental details

6.2.1 LSFL on titanium

The simulation domain of the titanium films consists of a dispersive plate of 400 nm whose roughness is composed of yee cells randomly distributed on the surface, the average roughness amplitude is 10 nm. The electromagnetic field source is a Gaussian-modulated plane-wave, central frequency $\nu_c = 291.26$ THz ($\lambda_c = 1030$ nm), pulse width at $1/e^2$ of 270 fs. On top of the Ti film we placed a thin layer (10 nm thickness) of titanium dioxide of dielectric constant $\varepsilon = 6.1619$ (DeVore, 1951). Figure 6.2.1 shows the evolution of the film surface. After 20 pulses, the resulting LIPSS consists of highly regular LSFL (DLOA = 2°) oriented perpendicular to the laser polarization whose periodicity is 897 nm.

In addition, we compute the intensity distribution beneath a 4.5 μm × 4.5 μm thin film (100 nm) of titanium dioxide (dielectric constant obtained from equation). A comparison between the light intensity profile is directly compared with a SEM micrograph of the LIPSS that we found in section 5.2. In both cases it is considered horizontal polarization.

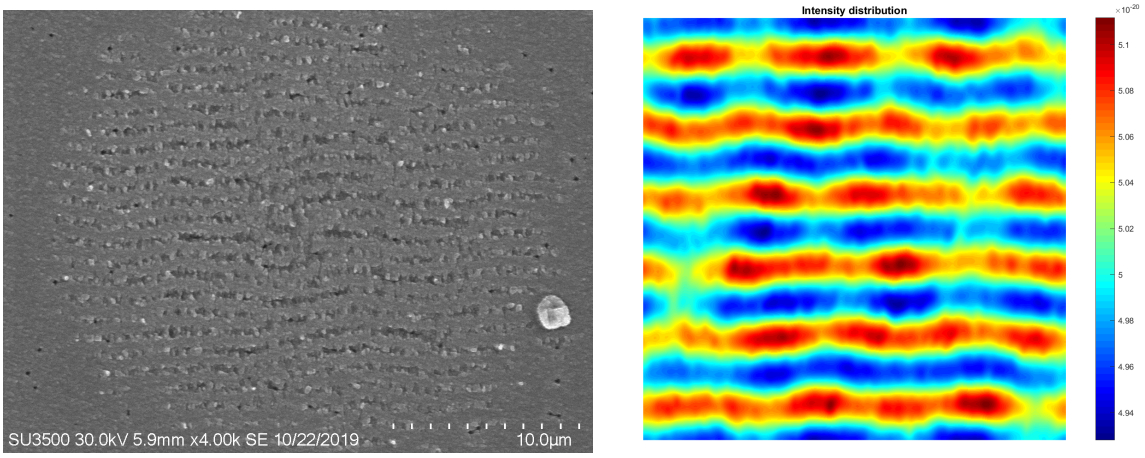

(a) a (b) b

Figure 49. Comparison of LIPSS obtained in titanium irradiated at normal incidence using 10^4 pulses (a) and the intensity distribution beneath a 100 nm TiO_2 film (b), periodicities of 810 nm and 750 nm respectively. The direction of the laser polarization is horizontal.

Both the LIPSS on TiO_2 and the simulation share the same orientation parallel to the light polarization and their periodicities are quite similar (810nm and 750 nm), the small difference may

result from the consecutive pulse irradiation as it is the case on the LIPSS described in section 4.6, we do not modified the surface after the first pulse since the physical mechanism may involve a mechanism different than that of the metals ablation, particularly since the electrical conductivity of the oxides is practically negligible so that we could not use the holographic ablation method described in section 6.1.5.

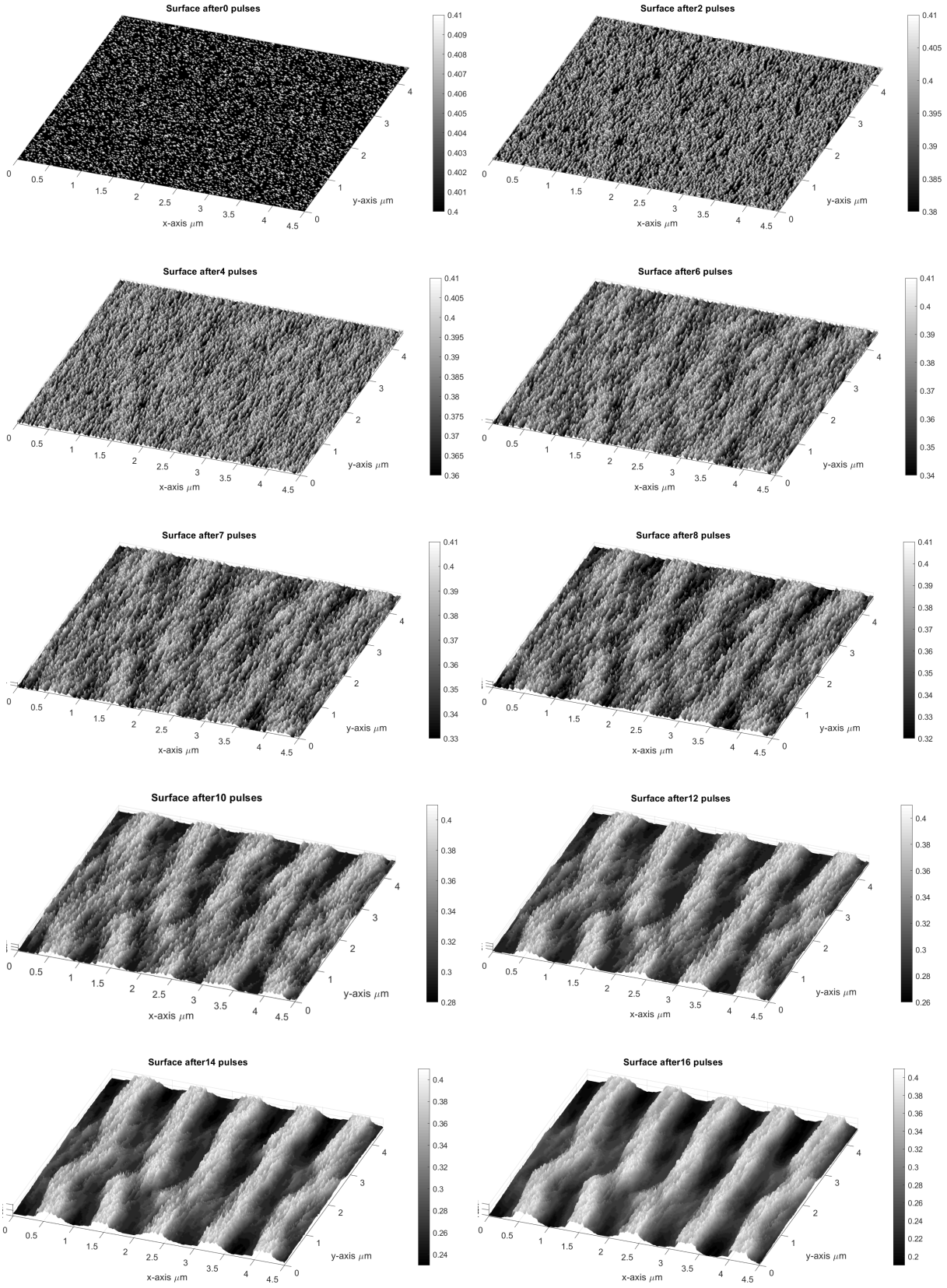

Figure 50. Simulation of a 400 nm titanium film, after beam irradiated with 16 pulses. Irradiation parameters are those of figure 48

Chapter 7. Conclusions

In this work, we demonstrated the effectiveness of equation 68 to provide suitable values of fluence and number of pulses to ensure the formation of LSFL and HSFL in Bi (figure 51) using fs-laser pulses far below the ablation threshold of bismuth. From the Fourier analysis of the corresponding SEM-micrographs, we studied the dependence of periodicity and DLOA on the number of pulses. Part of these results were published for first time in (Santillan *et al.*, 2020). Also, for first time, a theoretical study is carried on the formation of LIPSS in this material. In addition, we grew and studied LIPSS on titanium (figure 52).

We suggested an explanation for the LIPSS periodicity's dependence on the number of pulses based on a feedback process in which the grooves' depth plays a fundamental role. We assessed this hypothesis through numerical simulations in which we demonstrated the electromagnetic field is enhanced within the grooves. If the absorbed energy in this region exceeds that of the ablation threshold, then the LIPSS will become more profound with each pulse. As a consequence of the phase-matching condition, the SPPs dispersion diagram is modified so that the grating period, at which the SPP resonance occurs, is shifted to shorter periods (see figure 34). This feedback mechanism can explain the evolution in the LIPSS periodicity (see figure 25).

For a large number of pulses (> 300) we observed the emergence of LIPSS oriented parallel to the laser polarization, HSFL in the case of Bi and LSFL in the case of Ti. Using Raman spectroscopy we demonstrated the laser-induced oxidation of the samples. In this sense, the Effective Medium Approximation (EMA) was implemented to study the effect of the laser induce oxidation process in Ti. We conclude that it is a very useful tool and a deepest study should be carried out in this direction.

In regards to the predictive capacity of the theoretical models, we realized that both the SPP-interference Model and the Efficacy Factor Theory are capable of predicting the initial LIPSS periods, on the other hand the FDTD resulted a useful tool to simulate the specific features of the irradiated sample although the computational requirements might compromise the size of the simulated sample. Comparing the behavior of both materials, we found out that their intrinsic characteristics have a big impact in the LIPSS formation process. Due to the low fusion temperature of Bi (271.4^{o} C) lower values of fluence are needed to modify the surface morphology in comparison with Ti. Therefore, less energy is required to generate ablation in Bi. All this is consistent with the ablation fluence values reported in this work. On the other hand, laser processing performed in

air allow oxidation reaction, in particular, Ti is a highly reactive material. As was observed in this work this chemical effect accompanies this material during the formation of LIPSS.

References

Águas, H., Popovici, N., Pereira, L., Conde, O., Branford, W. R., Cohen, L. F., Fortunato, E., and Martins, R. 2008 . Spectroscopic ellipsometry study of co-doped tio2 films. *physica status solidi (a)*, **205**(4): 880–883.

Anisimov, S. I. 1974 . Electron emission from metal surfaces exposed to ultrashort laser pulses. *Sov. Phys.-JETP*, **39**(2): 375–377.

Birnbaum, M. 1965 . Semiconductor surface damage produced by ruby lasers. *Journal of Applied Physics*, **36**(11): 3688–3689.

Bonch-Bruevich, A. M., Libenson, M. N., Makin, V. S., and Trubaev, V. V. 1992 . Surface electromagnetic waves in optics. *Optical Engineering*, **31**(4): 718–731.

Bonse, J., Munz, M., and Sturm, H. 2005 . Structure formation on the surface of indium phosphide irradiated by femtosecond laser pulses. *Journal of Applied Physics*, **97**(1): 13538.

Bonse, J., Rosenfeld, A., and Krüger, J. 2009 . On the role of surface plasmon polaritons in the formation of laser-induced periodic surface structures upon irradiation of silicon by femtosecond-laser pulses. *Journal of Applied Physics*, **106**(10): 104910.

Bonse, J., Krüger, J., Höhm, S., and Rosenfeld, A. 2012 . Femtosecond laser-induced periodic surface structures. *Journal of Laser Applications*, **24**(4): 042006.

Bonse, J., Hohm, S., Kirner, S. V., Rosenfeld, A., and Krüger, J. 2017 . Laser-induced periodic surface structures— a scientific evergreen. *IEEE Journal of Selected Topics in Quantum Electronics*, **23**(3).

Borowiec, A. and K. Haugen, H. 2003 . Subwavelength ripple formation on the surfaces of compound semiconductors irradiated with femtosecond laser pulses. **82**: 4462 – 4464.

Camacho-López, S., Evans, R., Escobar-Alarcón, L., Camacho-López, M. A., and Camacho-López, M. A. 2008 . Polarization-dependent single-beam laser-induced grating-like effects on titanium films. *Applied Surface Science*, **255**(5): 3028 – 3032.

Chen, F., Zhang, D., Yang, Q., Yong, J., Du, G., Si, J., Yun, F., and Hou, X. 2013 . Bioinspired wetting surface via laser microfabrication. *ACS Applied Materials & Interfaces*, **5**(15): 6777–6792. PMID: 23865499.

Chun, Kyungwon & Kim, H. . K. H. . C. Y. 2013 . Plrc and ade implementations of drude-critical point dispersive model for the fdtd method. *Progress In Electromagnetics Research*, **135**: 373–390.

Condurache-Bota, S., Tigau, N., Rambu, A., Rusu, G., and Rusu, G. 2011 . Optical and electrical properties of thermally oxidized bismuth thin films. *Applied Surface Science*, **257**(24): 10545 – 10550.

Cornei, N., Tancret, N., Abraham, F., and Mentré, O. 2006 . New ε-bi2o3 metastable polymorph. *Inorganic Chemistry*, **45**(13): 4886–4888. PMID: 16780306.

Derkachova, A., K. K. and Demchenko, I. 2016 . Dielectric function for gold in plasmonics applications: Size dependence of plasmon resonance frequencies and damping rates for nanospheres. *Plasmonics*, **11**: 941–951.

Derrien, T. J.-Y., Itina, T. E., Torres, R., Sarnet, T., and Sentis, M. 2013 . Possible surface plasmon polariton excitation under femtosecond laser irradiation of silicon. *Journal of Applied Physics*, **114**(8): 083104.

DeVore, J. R. 1951 . Refractive indices of rutile and sphalerite. *J. Opt. Soc. Am.*, **41**(6): 416–419.

Diaz-Guerra, C., Almodovar, P., Camacho-Lopez, M., Camacho-Lopez, S., and Piqueras, J. 2017 . Formation of β-bi2o3 and δ-bi2o3 during laser irradiation of bi films studied in-situ by spatially resolved raman spectroscopy. *Journal of Alloys and Compounds*, **723**: 520 – 526.

Dorey, R. 2011 . *Ceramic Thick Films for MEMS and Microdevices*. Micro and Nano Technologies. Elsevier Science.

Dostovalov, A., Korolkov, V., Terentyev, V., Okotrub, K., Dultsev, F., and Babin, S. 2017 . Study of the formation of thermochemical laser-induced periodic surface structures on cr, ti, ni and nicr films under femtosecond irradiation. *Quantum Electronics*, **47**(7): 631–637.

Dostovalov, A.V., K.-V. B. S. 2017 . Formation of thermochemical laser-induced periodic surface structures on ti films by a femtosecond ir gaussian beam: regimes, limiting factors, and optical properties. *Appl. Phys. B*, **123**(30).

Dufft, D., Rosenfeld, A., Das, S. K., Grunwald, R., and Bonse, J. 2009 . Femtosecond laser-induced periodic surface structures revisited: A comparative study on zno. *Journal of Applied Physics*, **105**(3): 034908.

Dusser, B., Sagan, Z., Soder, H., Faure, N., Colombier, J., Jourlin, M., and Audouard, E. 2010 . Controlled nanostructrures formation by ultra fast laser pulses for color marking. *Opt. Express*, **18**(3): 2913–2924.

Elsherbeni, A. and Demir, V. 2009 . *The Finite-difference Time-domain Method for Electromagnetics with MATLAB Simulations*. SciTech Pub.

Emelyanov, V. I., Zayarniy, D. A., Ionin, A. A., Kiseleva, I. V., Kudryashov, S. I., Makarov, S. V., Nguyen, T. H. T., and Rudenko, A. A. 2014 . Nanoscale hydrodynamic instability in a molten thin gold film induced by femtosecond laser ablation. *JETP Letters*, **99**(9): 518–522.

Emmony, D. C., Howson, R. P., and Willis, L. J. 1973 . Laser mirror damage in germanium at 10.6 um. *Applied Physics Letters*, **23**(11): 598–600.

Fan, H. T., Teng, X. M., Pan, S. S., Ye, C., Li, G. H., and Zhang, L. D. 2005 . Optical properties of δ-bi2o3 thin films grown by reactive sputtering. *Applied Physics Letters*, **87**(23): 231916.

Fuentes-Edfuf, Y., Sánchez-Gil, J. A., Florian, C., Giannini, V., Solis, J., and Siegel, J. 2019 . Surface plasmon polaritons on rough metal surfaces: Role in the formation of laser-induced periodic surface structures. *ACS Omega*, **4**(4): 6939–6946.

Fujiwara, H. 2007 . *Spectroscopic Ellipsometry: Principles and Applications*. Wiley.

Gnilitskyi, I., Derrien, T. J., Levy, Y., Bulgakova, N., Mocek, T., and Orazi, L. 2017 . High-speed manufacturing of highly regular femtosecond laser-induced periodic surface structures: Physical origin of regularity. **7**.

Graf, S., Kunz, C., and Muller, F. A. 2017 . Formation and properties of laser-induced periodic surface structures on different glasses. *Materials*, **10**(8).

Gualtieri, A. F., Immovilli, S., and Prudenziati, M. 1997 . Powder x-ray diffraction data for the new polymorphic compound w-bi2o3. *Powder Diffraction*, **12**(2): 90–92.

Gujar, T., Shinde, V., and Lokhande, C. 2008 . The influence of oxidation temperature on structural, optical and electrical properties of thermally oxidized bismuth oxide films. *Applied Surface Science*, **254**(13): 4186 – 4190.

Gutiérrez, A. W. 2019 . Optimización del proceso de generación de lipss en metales con pulsos ultra-cortos. *Master thesis*.

Hagemann, H.-J., Gudat, W., and Kunz, C. 1975 . Optical constants from the far infrared to the x-ray region: Mg, al, cu, ag, au, bi, c, and al2o3. *J. Opt. Soc. Am.*, **65**(6): 742–744.

Hardcastle, F. D. and Wachs, I. E. 1992 . The molecular structure of bismuth oxide by raman spectroscopy. *Journal of Solid State Chemistry*, **97**(2): 319 – 331.

Huang, M., Zhao, F., Cheng, Y., Xu, N., and Xu, Z. 2009a . Origin of laser-induced near-subwavelength ripples: Interference between surface plasmons and incident laser. *ACS nano*, **3**: 4062–70.

Huang, M., Zhao, F., Cheng, Y., Xu, N., and Xu, Z. 2009b . Mechanisms of ultrafast laser-induced deep-subwavelength gratings on graphite and diamond. *Phys. Rev. B*, **79**: 125436.

Huynh, T. T. D. 2014 . *Etude de la dynamique de formation de nanostructures périodiques sur une couche mince de cuivre induites par impulsions laser nanoseconde et picoseconde à 266 nm*. Ph.D. Thesis, Université d'Orléans, Français.

Ismail, R. A. 2006 . Characteristics of bismuth trioxide film prepared by rapid thermal oxidation. *e-Journal of Surface Science and Nanotechnology*, **4**: 563–565.

Jee, Y., Becker, M. F., and Walser, R. M. 1988a . Laser-induced damage on single-crystal metal surfaces. *J. Opt. Soc. Am. B*, **5**(3): 648–659.

Jee, Y., Becker, M. F., and Walser, R. M. 1988b . Laser-induced damage on single-crystal metal surfaces. *J. Opt. Soc. Am. B*, **5**(3): 648–659.

Keilmann, F. and Bai, Y. H. 1982 . Periodic surface structures frozen into co2 laser-melted quartz. *Applied Physics A*, **29**(1): 9–18.

Krüger, J., Dufft, D., Koter, R., and Hertwig, A. 2007 . Femtosecond laser-induced damage of gold films. *Applied Surface Science*, **253**(19): 7815 – 7819.

Kuett, W., Esser, A., Seibert, K., Lemmer, U., and Kurz, H. 1990 . *Femtosecond studies of plasma formation in crystalline and amorphous silicon*, Vol. 1268. SPIE. pp. 154 – 165.

Leontie, L., Caraman, M., Alexe, M., and Harnagea, C. 2002 . Structural and optical characteristics of bismuth oxide thin films. *Surface Science*, **507-510**: 480 – 485.

Lide, D. 2003 . *CRC Handbook of Chemistry and Physics, 84th Edition*. CRC Handbook of Chemistry and Physics. Taylor & Francis.

Liu, J. M. 1982 . Simple technique for measurements of pulsed gaussian-beam spot sizes. *Opt. Lett.*, **7**(5): 196–198.

Maier, S. A. 2007 . *Plasmonics Fundamentals and Applications*. Springer.

Martsinovskiĭ, G. A., Shandybina, G. D., Smirnov, D. S., Zabotnov, S. V., Golovan', L. A., Timoshenko, V. Y., and Kashkarov, P. K. 2008 . Ultrashort excitations of surface polaritons and waveguide modes in semiconductors. *Optics and Spectroscopy*, **105**(1): 67–72.

Mendoza Herrera, L. J., Arboleda, D. M., Schinca, D. C., and Scaffardi, L. B. 2014 . Determination of plasma frequency, damping constant, and size distribution from the complex dielectric function of noble metal nanoparticles. *Journal of Applied Physics*, **116**(23): 233105.

Nanai, L., Vajtai, R., and Thomas, F. G. 1997 . Laser-induced oxidation of metals: state of the art. *Thin Solid Films*, **298**(1): 160–164.

Neuenschwander, B., Jaeggi, Schmid, M., Rouffiange, V., and Martin, P.-E. 2012 . *Optimization of the volume ablation rate for metals at different laser pulse-durations from ps to fs*, Vol. 8243. SPIE. pp. 43 – 55.

Neuenschwander, B., , Jaeggi, B., Schmid, M., Dommann, A., Neels, A., Bandi, T., and Hennig, G. 2013 . *Factors controlling the incubation in the application of ps laser pulses on copper and iron surfaces*, Vol. 8607. SPIE. pp. 26 – 35.

Niso, F. D., Gaudiuso, C., Sibillano, T., Mezzapesa, F. P., Ancona, A., and Lugarà, P. M. 2014a . Role of heat accumulation on the incubation effect in multi-shot laser ablation of stainless steel at high repetition rates. *Opt. Express*, **22**(10): 12200–12210.

Niso, F. D., Gaudiuso, C., Sibillano, T., Mezzapesa, F. P., Ancona, A., and Lugarà, P. M. 2014b . Role of heat accumulation on the incubation effect in multi-shot laser ablation of stainless steel at high repetition rates. *Opt. Express*, **22**(10): 12200–12210.

Okoniewski, M. and Okoniewska, E. 2006 . Drude dispersion in ade fdtd revisited. *Electronics Letters*, **42**(9): 503–504.

Okoniewski, M., Mrozowski, M., and Stuchly, M. A. 1997 . Simple treatment of multi-term dispersion in fdtd. *IEEE Microwave and Guided Wave Letters*, **7**(5): 121–123.

Ossi, P. 2018 . *Advances in the Application of Lasers in Materials Science*. Springer Series in Materials Science. Springer International Publishing.

Phillips, K. C., Gandhi, H. H., Mazur, E., and Sundaram, S. K. 2015 . Ultrafast laser processing of materials: a review. *Adv. Opt. Photon.*, **7**(4): 684–712.

Raether, H. 2006 . *Surface Plasmons on Smooth and Rough Surfaces and on Gratings*. Springer Tracts in Modern Physics. Springer Berlin Heidelberg.

Raether, H. 2014 . *Surface Plasmons on Smooth and Rough Surfaces and on Gratings*. Springer.

Rakić, A. D., Djurišić, A. B., Elazar, J. M., and Majewski, M. L. 1998 . Optical properties of metallic films for vertical-cavity optoelectronic devices. *Appl. Opt.*, **37**(22): 5271–5283.

Reif, J., Costache, F., Henyk, M., and Pandelov, S. 2002 . Ripples revisited: non-classical morphology at the bottom of femtosecond laser ablation craters in transparent dielectrics. *Applied Surface Science*, **197**: 891–895.

Reyes-Contreras, A., Camacho-López, M., Camacho-López, S., Olea-Mejía, O., Esparza-García, A., Bañuelos-Muñetón, J. G., and Camacho-López, M. A. 2017a . Laser-induced periodic surface structures on bismuth thin films with ns laser pulses below ablation threshold. *Opt. Mater. Express*, **7**(6): 1777–1786.

Reyes-Contreras, A., Camacho-López, M., Camacho-López, S., Olea-Mejía, O., Esparza-García, A., nuelos Muñetón, J. G. B., and Camacho-López, M. A. 2017b . Laser-induced periodic surface structures on bismuth thin films with ns laser pulses below ablation threshold. *Opt. Mater. Express*, **7**(6): 1777–1786.

Römer, G., Skolski, J., Oboňa, J. V., and in't Veld, A. H. 2014 . Finite-difference time-domain modeling of laser-induced periodic surface structures. *Physics Procedia*, **56**: 1325 – 1333. 8th International Conference on Laser Assisted Net Shape Engineering LANE 2014.

Rzeszotarski, M.S., R. F. and Gilmore, G. 1983 . Introduction to two-dimensional fourier analysis. *Behavior Research Methods & Instrumentation*, **15**: 308–3018.

Sakabe, S., Lienau, C., and Grunwald, R. 2014 . *Progress in Nonlinear Nano-Optics*. Springer International Publishing.

Salazar, A. J., Camacho-Lopez, M. A., Morales-Luckie, R. A., Sanchez-Mendieta, F., and Arenas-Alatorre, J. 2005 . Structural evolution of bi2o3 prepared by thermal oxidation of bismuth nano-particles. *Superficies y vacio*, **18**: 4–8.

Santillan, R., Wong, A., Segovia, P., Camacho-Lopez, M., and Camacho-Lopez, S. 2020 . Femtosecond laser-induced periodic surface structures formation on bismuth thin films upon irradiation in ambient air. *Opt. Mater. Express*, **10**(2): 674–681.

Schaaf, P. 2010 . *Laser Processing of Materials: Fundamentals, Applications and Developments*, Vol. 139.

Segovia, P. and Coello, V. 2012 . Elastic surface plasmon polariton scattering: Near- and far-field interactions. *Nano*, **07**(01): 1150003.

Shinonaga, T., Tsukamoto, M., and Miyaji, G. 2014 . Periodic nanostructures on titanium dioxide film produced using femtosecond laser with wavelengths of 388 nm and 775 nm. *Opt. Express*, **22**(12): 14696–14704.

Shugaev, M. V., Wu, C., Armbruster, O., Naghilou, A., Brouwer, N., Ivanov, D. S., Derrien, T. J.-Y., Bulgakova, N. M., Kautek, W., Rethfeld, B., and et al. 2016 . Fundamentals of ultrafast laser–material interaction. *MRS Bulletin*, **41**(12): 960–968.

Sipe, J. E., Young, J. F., Preston, J. S., and van Driel, H. M. 1983 . Laser-induced periodic surface structure. i. theory. *Phys. Rev. B*, **27**: 1141–1154.

Skolski, J. 2010 . Modeling of laser induced periodic surface structures. *JLMN-Journal of Laser Micro/Nanoengineering*, **5**(3).

Sokolowski-Tinten, K. and von der Linde, D. 2000 . Generation of dense electron-hole plasmas in silicon. *Phys. Rev. B*, **61**: 2643–2650.

Steele, J. A. and Lewis, R. A. 2014 . In situ micro-Raman studies of laser-induced bismuth oxidation reveals metastability of β-Bi2O3 microislands. *Opt. Mater. Express*, **4**(10): 2133–2142.

Sukhotskiy, V., Cady, N., Chou, E., Reddy, I., and Furlani, E. 2018 . Numerical modelling of a sinusoidal grating-based surface plasmon coupled emission biosensor. *TechConnect Briefs*, **4**: 205–208.

Taflove, A. and Brodwin, M. E. 1975 . Numerical solution of steady-state electromagnetic scattering problems using the time-dependent maxwell's equations. *IEEE Transactions on Microwave Theory and Techniques*, **23**(8): 623–630.

Taflove, A. and Hagness, S. 2005 . *Computational Electrodynamics: The Finite-difference Time-domain Method*. Artech House Antennas and Prop. Artech House.

Takayama, Y. and Klaus, W. 2002 . Reinterpretation of the auxiliary differential equation method for fdtd. *IEEE Microwave and Wireless Components Letters*, **12**(3): 102–104.

Toudert, J., Serna, R., Camps, I., Wojcik, J., Mascher, P., Rebollar, E., and Ezquerra, T. A. 2017 . Unveiling the far infrared-to-ultraviolet optical properties of bismuth for applications in plasmonics and nanophotonics. *The Journal of Physical Chemistry C*, **121**(6): 3511–3521.

Toudert, J., Serna, R., Deeb, C., and Rebollar, E. 2019 . Optical properties of bismuth nanostructures towards the ultrathin film regime. *Opt. Mater. Express*, **9**(7): 2924–2936.

Tsibidis, G. D. and Stratakis, E. 2017 . Ripple formation on silver after irradiation with radially polarised ultrashort-pulsed lasers. *Journal of Applied Physics*, **121**(16): 163106.

Werner, W. S. M., Glantschnig, K., and Ambrosch-Draxl, C. 2009 . Optical constants and inelastic electron-scattering data for 17 elemental metals. *Journal of Physical and Chemical Reference Data*, **38**(4): 1013–1092.

Xia, F., Jiao, L., Wu, D., Li, S., Zhang, K., Kong, W., Yun, M., Liu, Q., and Zhang, X. 2019 . Mechanism of pulsed-laser-induced oxidation of titanium films. *Opt. Mater. Express*, **9**(10): 4097–4103.

Xian-Feng Li, Cheng-Yun Zhang, H. L. Q.-F. D. S. L. S.-L. T. 2014 . Formation of 100-nm periodic structures on a titanium surface by exploiting the oxidation and third harmonic generation induced by femtosecond laser pulses. *Opt. Express*, **22**(23): 28086–28099.

Xiaofan Yang, Xiaoming Liu, S. Y. L. G. J. Z. and Zeng, Y. 2019 . Permittivity of undoped silicon in the millimeter wave range. *Electronics*, **8**(886).

Young, J. F., Preston, J. S., van Driel, H. M., and Sipe, J. E. 1983 . Laser-induced periodic surface structure. ii. experiments on ge, si, al, and brass. *Phys. Rev. B*, **27**: 1155–1172.

Zeng, Y., Hoyer, W., Liu, J., Koch, S. W., and Moloney, J. V. 2009 . Classical theory for second-harmonic generation from metallic nanoparticles. *Phys. Rev. B*, **79**: 235109.

Zepeda, M. A., Picquart, M., and Haro-Poniatowski, E. 2012 . Laser induced oxidation effects in bismuth thin films. *MRS Proceedings*, **1477**: imrc12–1477–s1a–p016.

Appendix A. Optical micrographs

Bismuth

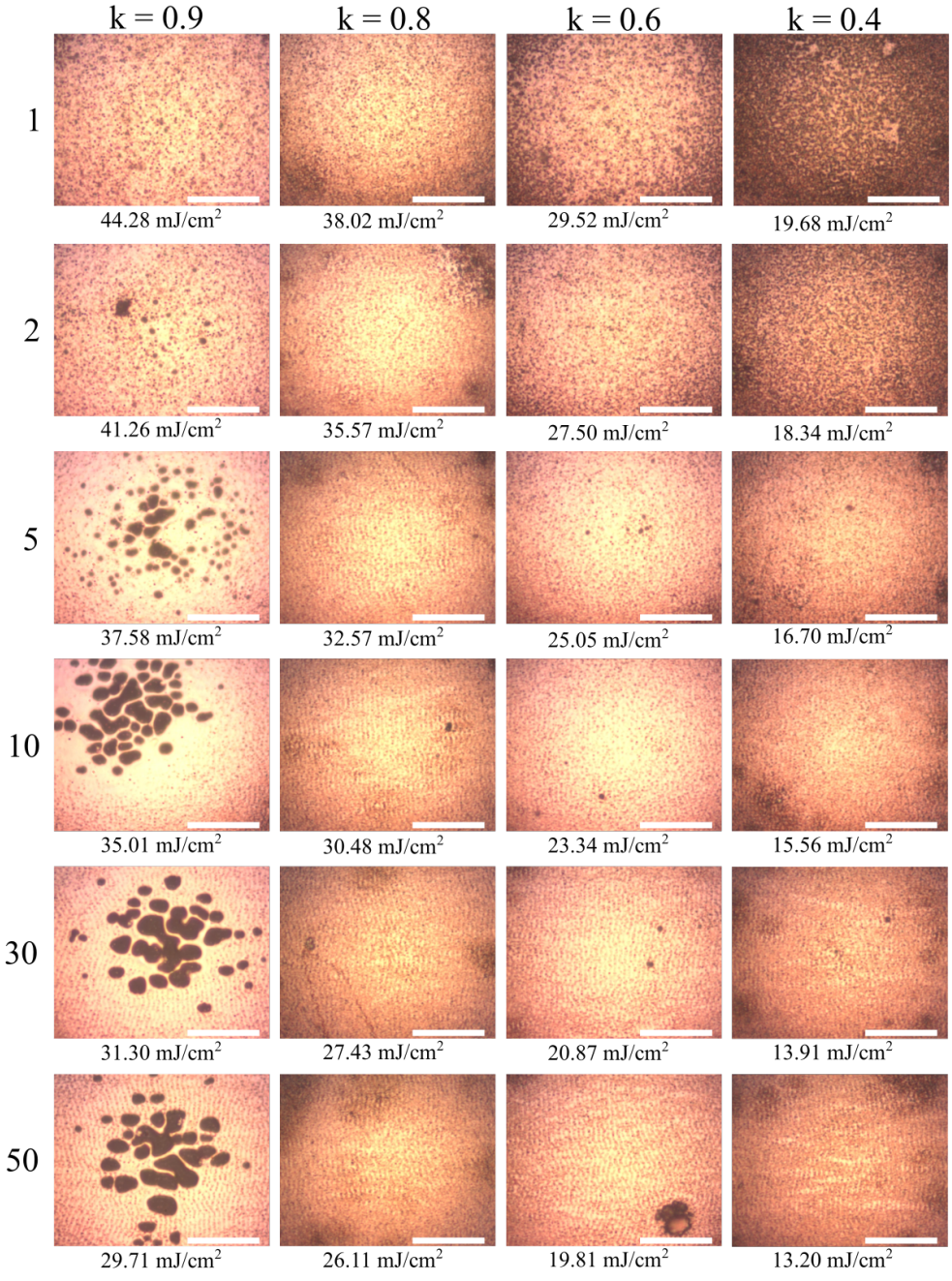

(a)

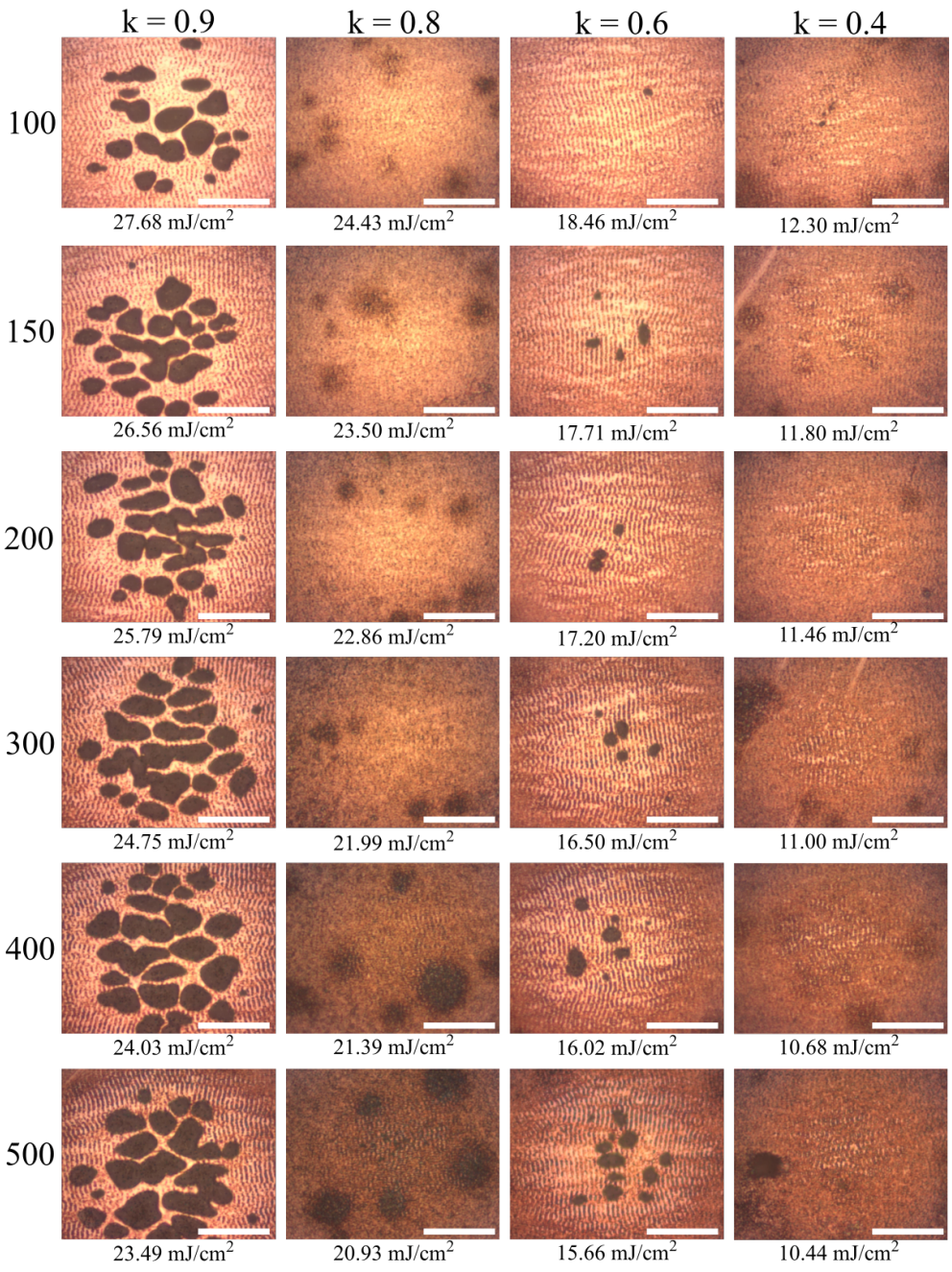

(b)

Figure 51. OM micrographs of irradiation spots on bismuth, the respective number of pulses and fluence are indicated on each picture, the laser polarization lies on the horizontal direction. White scale bar indicates 15 μm.

Titanium

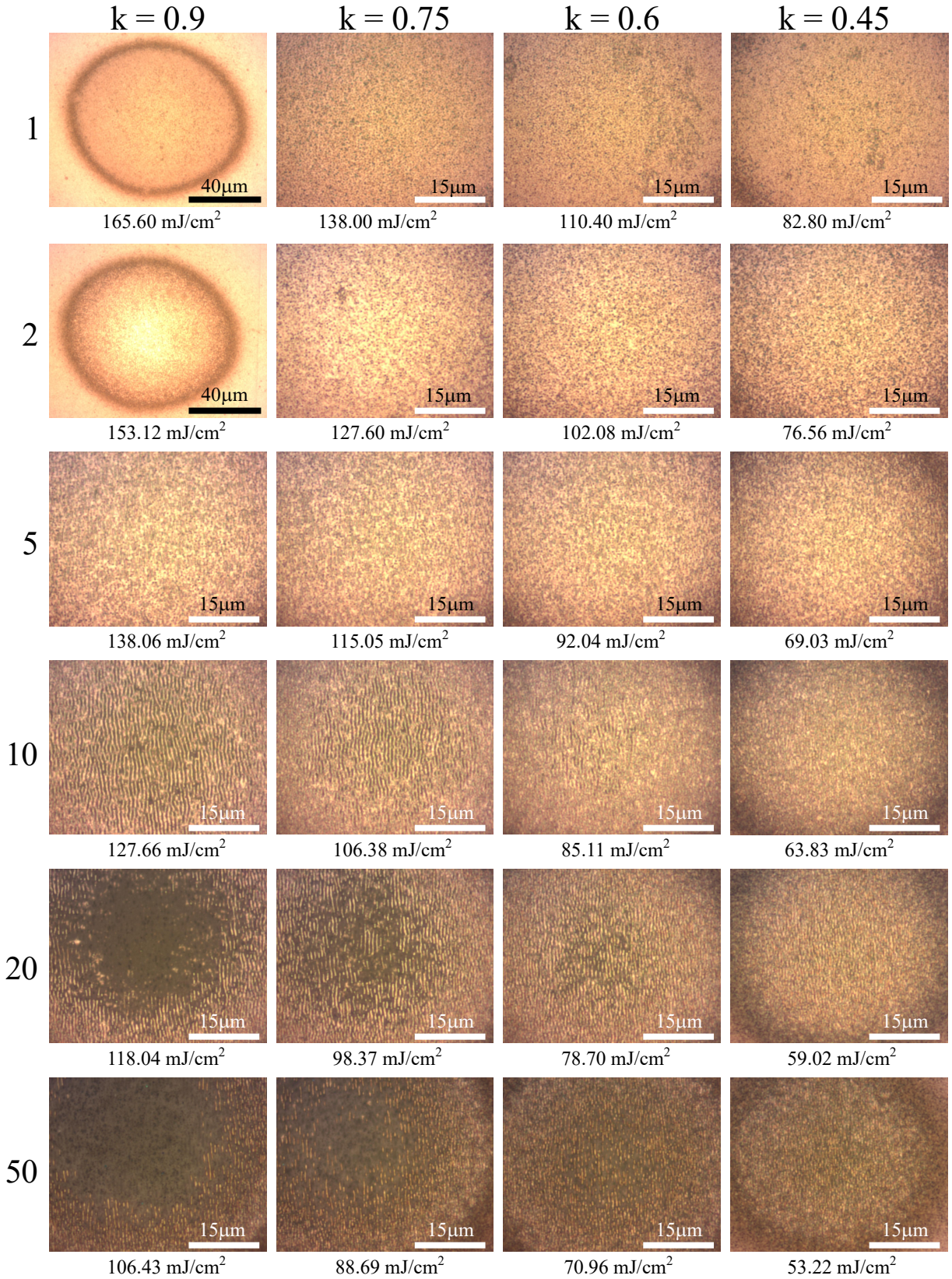
k = 0.9
k = 0.75
k = 0.6
k = 0.45
1
2
5
10
20
50
40µm
15µm
165.60 mJ/cm2
138.00 mJ/cm2
110.40 mJ/cm2
82.80 mJ/cm2
153.12 mJ/cm2
127.60 mJ/cm2
102.08 mJ/cm2
76.56 mJ/cm2
138.06 mJ/cm2
115.05 mJ/cm2
92.04 mJ/cm2
69.03 mJ/cm2
127.66 mJ/cm2
106.38 mJ/cm2
85.11 mJ/cm2
63.83 mJ/cm2
118.04 mJ/cm2
98.37 mJ/cm2
78.70 mJ/cm2
59.02 mJ/cm2
106.43 mJ/cm2
88.69 mJ/cm2
70.96 mJ/cm2
53.22 mJ/cm2

(a)

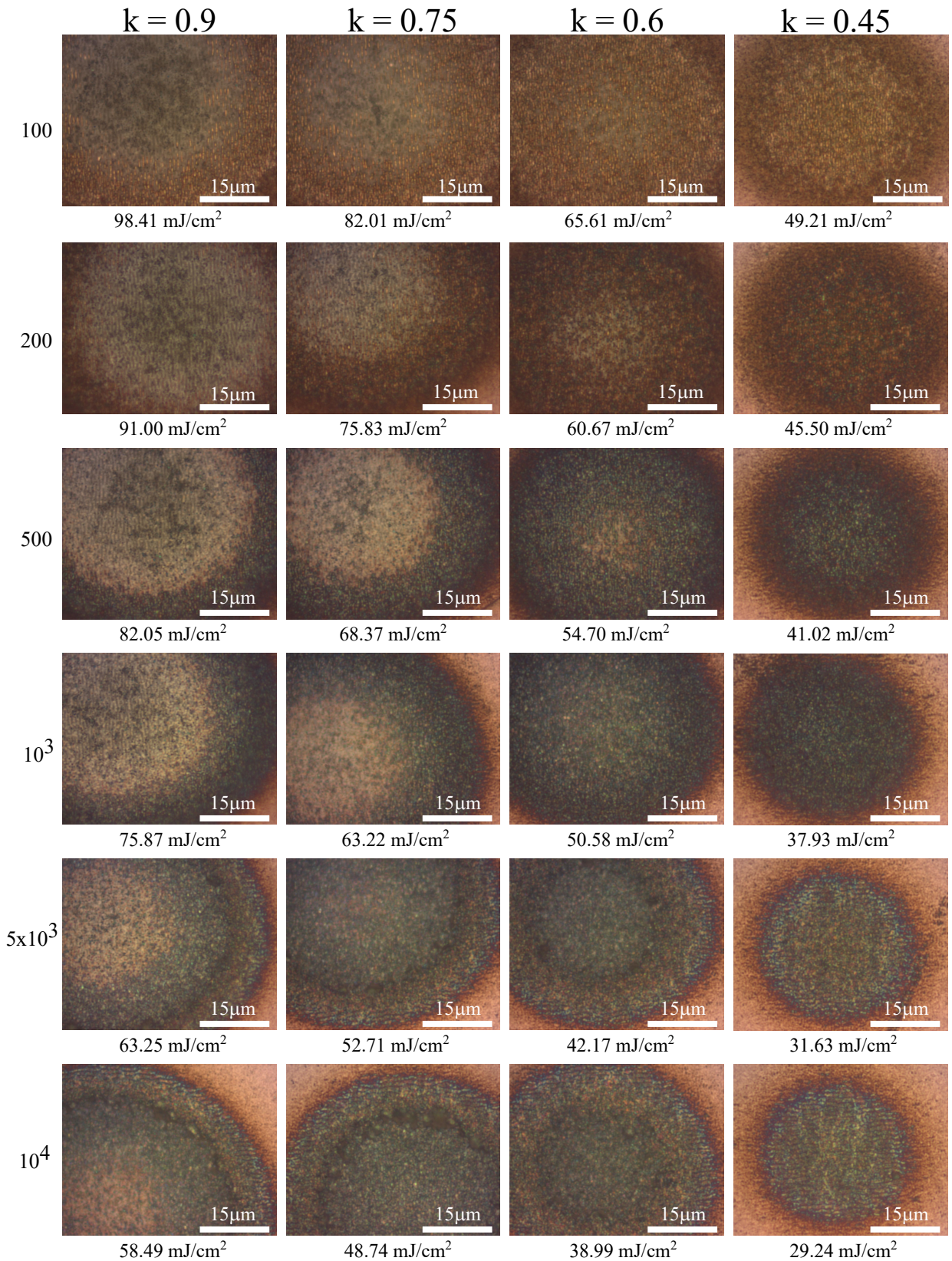

(b)

Figure 52. OM micrographs of irradiation spots on titanium, the respective number of pulses and fluence are indicated on each picture, the laser polarization lies on the horizontal direction. White scale bar indicates 15 μm.

Appendix B. SEM micrographs

Bismuth

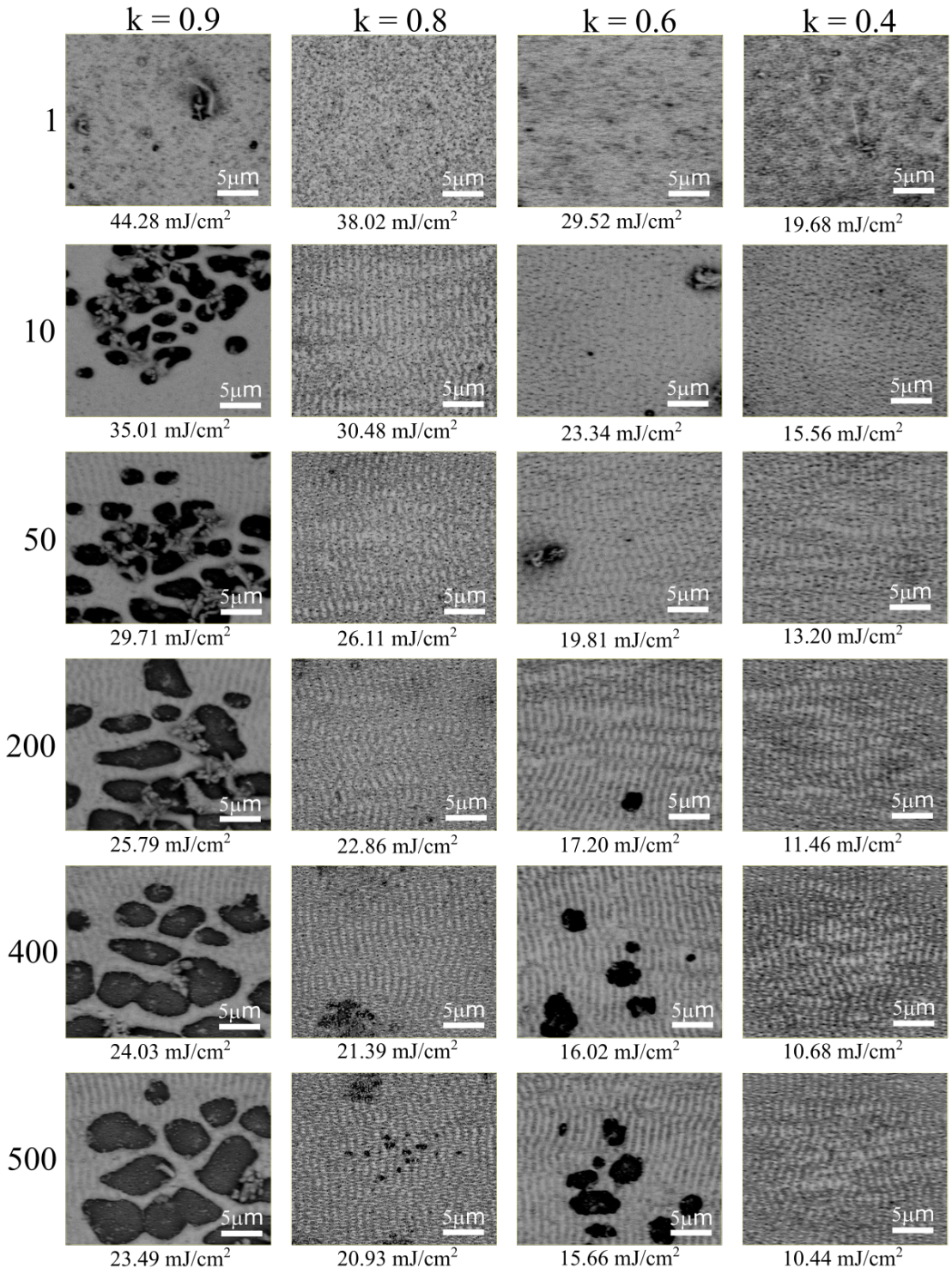

Figure 53. SEM micrographs of irradiation spots on bismuth, the respective number of pulses and fluence are indicated on each picture, the laser polarization lies on the horizontal direction.

Titanium

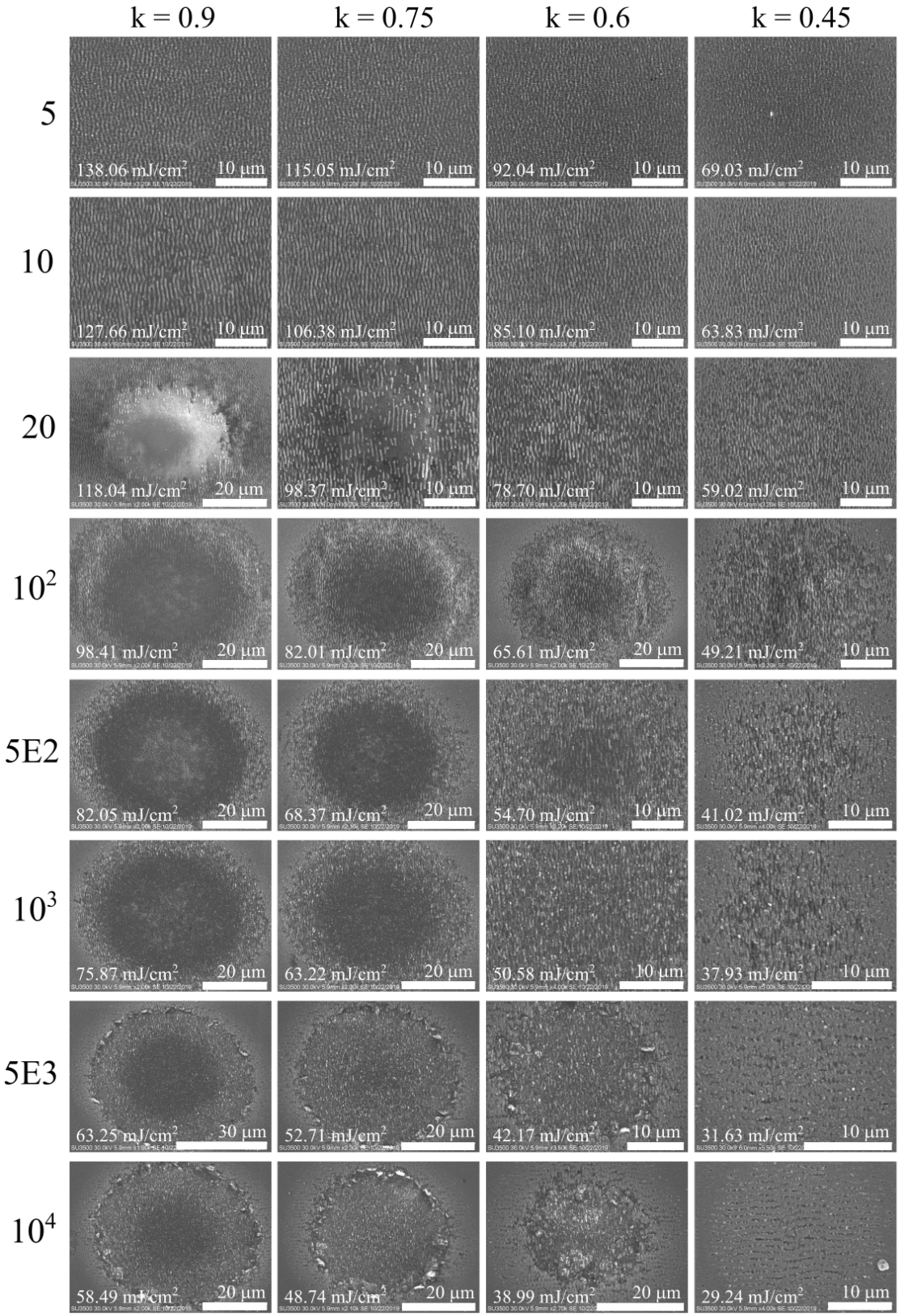

Figure 54. SEM micrographs of irradiation spots on titanium, the respective number of pulses and fluence are indicated on each picture, the laser polarization lies on the horizontal direction.

.